ISTITUTO ITALIANO DI TECNOLOGIA

UNIVERSITA' DEGLI STUDI DI NAPOLI "FEDERICO II"

SCUOLA POLITECNICA E DELLE SCIENZE DI BASE

PhD thesis in "Industrial product and process Engineering"

XXXII cycle

"MICROFLUIDIC SYNTHESIS AND ENGINEERING OF HYDROGEL-BASED BIOSENSOR FOR IN-GEL IMMUNOASSAYS"

Supervisors:

Prof. Dr. Filippo Causa

Prof. Dr. Paolo Antonio Netti

Co-tutors:

Dr. Pasqualina Liana Scognamiglio

Dr. Edmondo Battista

Candidate

Alessandra De Masi

2017/2020

Table of contents

List of Abbreviations

10R4	PEGDA 15% (v/w) + PEGDA/DHEBA 4:1
10R40	PEGDA 10% (v/w) + PEGDA/DHEBA 40:1
15R4	PEGDA 15% (v/w) + PEGDA/DHEBA 4:1
15R40	PEGDA 15% (v/w) + PEGDA/DHEBA 40:1
anti hIgG-FC	monoclonal antihuman IgG FC specific
antih-IgG FAB	monoclonal anti-human IgG FAB specific
antih-IgGFAB647	anti-human IgG FAB labelled with atto647N
BSA	Bovine serum albumin
C	Cleaved microparticles
Ca	Capillary number
CAD	Computer Aided Design
CALUX	Chemical-activated luciferase expression
CAM	Computer-aided manufacturing
CLSM	Confocal laser scanning microscope
Cryo-SEM	cryo scattering electron microscope
CV	Coefficient of variability
DHEBA	N,N′(1,2Dihydroxyethylene)bisacrylamide
DLCs	Dioxin-like compounds
DMSO	Dimethylsulfoxide
DNA	Deoxyribonucleic Acid
DSC	Differential scanning calorimetry
ELISA	Enzyme linked immunosorbent assay
FBS	Fetal bovine serum
FCS	Fluorescence correlation spectroscopy
FITC	Fluorescein isothiocyanate

GC	Gas chromatography
hIgG	Human Immunoglobulin G
hIgG-atto647N	Immunoglobulin G labelled with atto647N
HR-GC/MS	High-resolution gas chromatography/mass spectroscopy
HSA	Human serum albumin
IgG	Immunoglobulin G
IgG-FITC	Immunoglobulin G labelled with FITC
LMO	Light mineral oil
LOD	Limit of detection
MetS	Metabolic syndrome
miRNA	micro-RNA
NC	Non-cleaved microparticles
NMR	Nuclear magnetic resonance
OVA-dioxin ATTO647N	Ovalbumin conjugated with dioxin labelled with atto674N
OVA-dioxin	Ovalbumin conjugated with dioxin
PBS	Phosphate buffered saline
PDMS	Polydimethylsiloxane
PEG	Poly (ethylene glycol)
PEGDA	Poly (ethylene glycol)dyacrylate
PMMA	Poly(methyl methacrylate)
POPs	Persistent organic pollutants
PPF	poly(propylene fumarate)
PVA	poly(vinyl alcohol)
RIA	Radioimmunoassay
RNA	Ribonucleic Acid
SEM	Standard error of the mean

TCDD	2,3,7,8-tetrachlorodibenzo-para-dioxin
TEQ	Toxic equivalents
UV	Ultra violet light
UV/Vis	UV and visible light
v/v	volume/volume ratio
v/w	volume/weight ratio
W/O emulsion	Water in oil emulsion

Abstract

Recently hydrogel microparticles have been widely used as a versatile tool to perform beads-based assays due to their hydrophilic, biocompatible and highly flexible chemical and physical properties. Since the chemical properties of the polymeric network can be tuned, the gel can be easily functionalized with any type of biomolecule. Late studies show an ever-increasing interest in performing microparticles-based sandwich immunoassays, using primary antibodies to capture a specific biomarker and a fluorescent secondary antibody to show the binding event. In order to adapt this scheme to hydrogels, where diffusion represents the limiting factor, it is necessary to increase the porosity of the network and avoid non-specific interactions between gel and biomolecules.

The following PhD project aims to design, synthesize and characterize PEG-based hydrogels microparticles able to detect specific biomarkers with high sensitivity in complex fluids such as serum, blood and urine. Hydrogel microparticles thus realized show a high sensitivity due to their capability to concentrate the target in a small volume, amplifying the signal.

This PhD project can be divided into several steps:

- Design and microfluidic synthesis of the hydrogels microparticles
- Characterization of the hydrogel microparticles
- Assay optimization and specificity tests
- Realization of a microfluidic device to perform assays on chip

Microfluidics offers a high-throughput platform for synthesizing uniform and monodisperse polymeric microspheres in one step. In particular, a T-junction glass chip was used to produce 70-75 µm diameter microparticles, polymerized on flow by a UV lamp. PEG microparticles were obtained using light mineral oil mixed with nonionic surfactant Span 80 as continuous phase and PEGDA, Darocur 1173 and N,N′(1,2Dihydroxyethylene)bisacrylamide (DHEBA) as disperse phase.

DHEBA is a cleavable crosslinker which can be cut via oxidation, increasing the pore size in order to allow the passage of antibodies and, simultaneously, producing aldehydes that can be used for further conjugation. In order to characterize the hydrogel microparticles, cleavage

kinetics and conditions, porosity, aldehydes titration, diffusion and equilibrium partitioning of fluorescent probes (antibodies and 50 nm nanoparticles) have been analyzed. Optimized conjugated hydrogel microparticles were then used to perform a sandwich immunoassay on hIgG. Experimental data show a limit of detection in the picomolar range, a high specificity and selectivity of the assay (in presence of unrelated proteins) and good results even in complex fluids such as serum and urine. To detect low-molecular-weight biomolecules, which are not suitable for a sandwich system, a bead-based competitive assay has been developed and optimized. The experimental data confirm a limit of detection in the picomolar range.

In order to speed up all the incubation and washing steps, the assay has been implemented inside a microfluidic chip, which can host up to five particles in parallel. Preliminary studies on the capture of fluorescent probes and washing volumes and time have been performed.

1. Introduction

1.1. Hydrogels: Principal concepts

Hydrogels are defined as three dimensional cross-linked polymeric networks that can absorb a large amount of aqueous solvents and biological fluids without dissolving[1–3]. Nowadays, hydrogels have attracted great interest in different research fields such as drug delivery[4,5], tissue engineering[6,7], optics, diagnostics[8,9] and imaging, since they can react (swell or de-swell) to different external stimuli (Figure 1.1)[10].

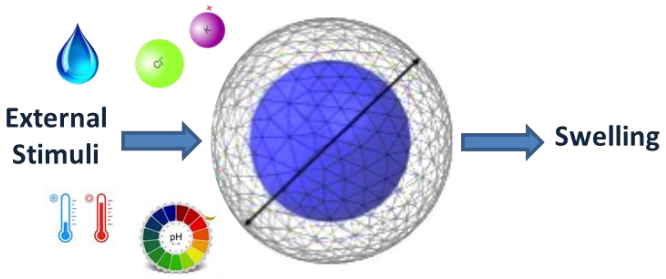

Figure 1.1: Schematic illustration of hydrogel swelling (and deswelling) in response to different external stumuli.

Hydrogels can be classified on the base of different parameters[11] such as physical structure, ionic charge, synthesis mechanism, size, bonds and structural and mechanical characteristics (Figure 1.2).

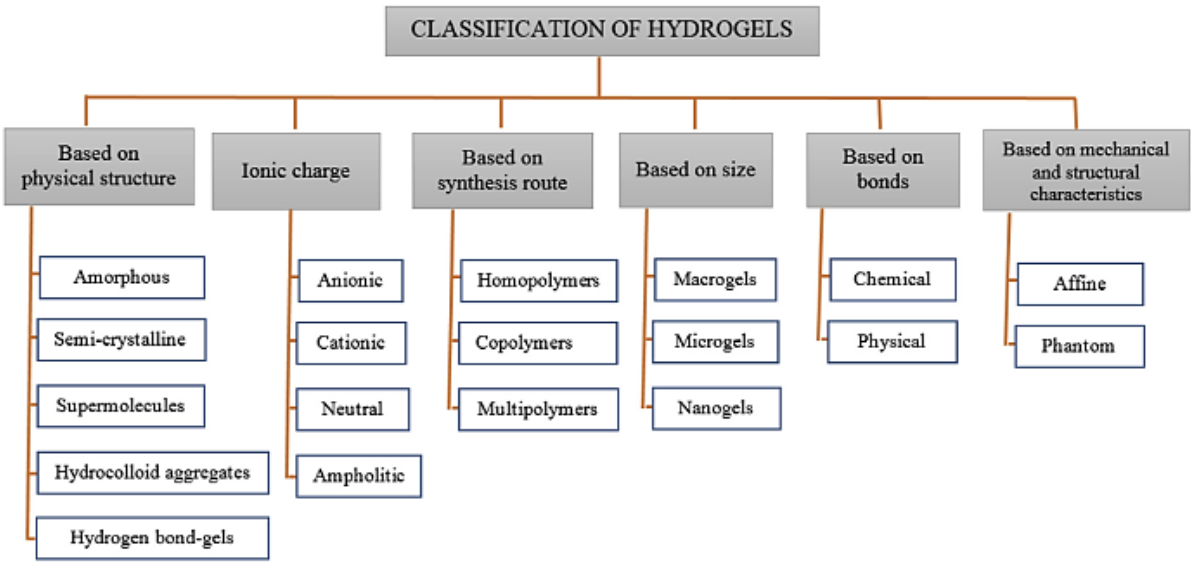

Figure 1.2: Classification of hydrogel based on different parameters: physical structure, ionic charge, synthesis mechanism, size, bonds and structural and mechanical characteristics[12].

Typically, hydrogels can be categorized basing on their size as nanogels, microgels and macrogels. The first ones are defined as a colloidal stable system, with a water swellable polymeric networks whose diameter typically ranges from 100 nm to 1 μm. Microgels, instead, show a range from tens to hundreds of microns and can present an inhomogeneous distribution of polymer chains throughout the network[13,14]. Macrogels are bulk networks with a size typically ranging from hundreds of microns to millimetres or more. Hydrogels can be also classified into chemical and physical, based on their crosslinking chemistry[15]. Physical gels are defined as polymeric networks bound together via polymer chain entanglement and/or non-covalent interactions, typically hydrogen bonding, electrostatic or hydrophobic interactions[16–18]. The chemical crosslinked gels, instead, present a higher stability due to the covalent bonds between different polymer chains (crosslinks)[19,20]. These gels are usually formed through monomer polymerization in the presence of a crosslinking agent, which typically presents two reactive moieties. Based on physical structures of networks, hydrogels can be amorphous[21], semi-crystalline[22], hydrogels with hydrogen-bond structure[23], supermolecules, and hydro-colloid aggregates[24]. In terms of ionic charges present in a polymer network, hydrogels are classified into anionic[25,26], cationic[27], neutral[28], and ampholitic hydrogels[29]. Finally, basing on their composition, hydrogels are classified into homopolymers (one monomer type), copolymers (two monomer types), and multipolymers (three or more monomer types).

Many polymer are available to synthetize hydrogels as collagen, gelatin, chitosan, hyaluronic acid, alginate, poly(vinyl alcohol) (PVA), poly(propylene fumarate) (PPF), PNIPAAm20[30] and many others. In particular, from the literature, emerges the poly(ethylene)glycol (PEG) as the perfect candidate to synthesise hydrogels for biomedical applications thanks to its anti-fouling properties that prevents non-specific interactions between the gel and biomolecules different from the target[31]. PEGs are relatively inexpensive and available in a large range of molecular weights and chemical modifications: PEG molecular weights ranging from a few hundred to several thousand grams per mole have been used to fabricate hydrogel particles[32]. Moreover, PEGs show good solubility in aqueous buffers required for biomolecule manipulation[33,34]. Typically, PEG hydrogels are obtained through free-radical polymerization between (meth)acrylate or diacrylates PEG derivatives in presence of a UV-sensitive photoinitiator[35].

1.2 Hydrogel microparticles synthesis

One of the major advantages of use hydrogels microparticles is the great variety of chemical strategies available for their synthesis, including one-step procedures like parallel crosslinking of multifunctional monomers, as well as multiple step procedures, concerning synthesis of polymer molecules with reactive groups and their subsequent crosslinking. These synthesis procedures are typically performed in batch[36] and can be thermal, radical or photo-activated depending on the nature of the initiator used. It is possible to identify three different preparation strategies, based on the particle formation mechanism: homogeneous nucleation, emulsification[37] and complexation[38]. In the first one hydrogel microparticles are produced starting from a homogeneous solution while the emulsification process involves the formation of pre-polymer solution droplets in an oil phase. Emulsification represents the best technique to obtain core-shell microparticles[39].

Finally, microparticles can be synthesized by complexation, mixing two dilute water-soluble polymers that can form complexes in water. Recent applications for hydrogel microparticles, especially in the biomedical field, high control on their size and structure (crosslinking density) and tailored physico-chemical properties such as swelling behaviour and response to stimuli [1,40]. For this reason, microfluidic methods are gaining a great interest in literature in order to achieve major control on size and shape of microparticles, to use milder chemistry and reduce time and cost of the synthesis.

Among microfluidic-based methods, techniques based on droplet generation and flow lithography are the most used. The first method allows the production of sphere-like particles, while the second is an ideal alternative for designing non-spherical particles, such as rods, flakes and shape-coded particles, which are more desirable in some particular applications (Figure 1.3). Microfluidic-based hydrogel microparticles synthesis relays on the formation of a stable water in oil emulsion between an oil phase (continuous phase) and a pre-polymeric aqueous phase with an initiator (dispersed phase). The most used continuous phases are light mineral oil, silicone oil, corn oil, hexadecane and fluorinated oil, combined with a surfactant to stabilize the emulsion[42].

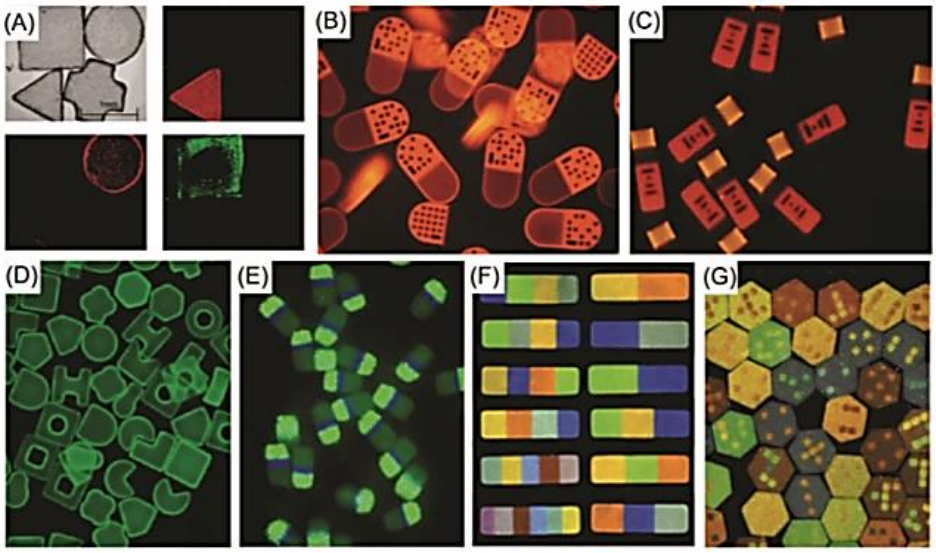

Figure 1.3: Overview of encoded hydrogel microparticles synthesized by photolithographic methods. (A) PEG hydrogel microparticles of various shapes fabricated by contact lithography. (B) 2-D barcoded hydrogel microparticles synthesized by flow lithography. (C) 1-D barcoded hydrogel microparticles. (D) Different shapes of PEG hydrogel microparticles fabricated by replica molding. (E) QD-encoded hydrogel microparticles synthesized by flow lithography. (F) PEG hydrogel microparticles incorporating upconversion nanoparticles synthesized by flow lithography (G) PEG hydrogel microparticles with M-Ink color-encoding patterns.[41]

Droplet formation in microchannels has been mainly achieved using flow focusing, co-flow, T-junction and step emulsification combined with cross flow/co-flow techniques. The synthesis occurs in a miniaturized device typically made of glass or polydimethylsiloxane (PDMS). The crosslinking of polymeric monomers can be achieved either into the device (on-chip) or in separated vials (off-chip) and is induced by UV/Vis light[43], via thiol-Michael addition click reaction[44] or changing the temperature and ionic crosslinking[45]. Regarding the droplet generation methods, the formation of the droplet depends by several parameters such as flow rates and their ratio, viscosity of the fluid, characteristic channels dimensions, device geometry, capillary number (Ca) and surface tension[46]. To obtain a stable emulsion and monodisperse droplets, synthesis conditions must be optimized. This technique has been extensively used in literature to produce monodisperse hydrogel microparticles for biomedical applications[47–52].

Doyle et al. introduced flow-lithography[53] in 2006. Particles are synthetized in high-throughput PDMS microfluidic device. Shape and size of the particles are controlled using a patterned lithographic mask, through which UV light photo-cures the particles with the desired shape directly on flow into the microfluidic channels. As results, they were able to obtain a high

number of codes combining graphical and spectral encoding, as well as different chemistries such as Janus particles[54]. Further improvements have been made developing the stop-flow lithography[55], where the pumping system is actuated so that the flow is stopped for few milliseconds allowing the polymerization through a mask.

1.3 Physical and chemical hydrogels characterizations

1.3.1 Target Diffusion in Hydrogel

Particular attention must be attained in the evaluation of biomolecules diffusion in hydrogel matrices since it provides important information about analyte accessibility and allow to properly set-up a bioassay. Information about diffusion of fluorescently labelled probes can be obtained with several techniques but the most used are Fluorescence correlation spectroscopy (FCS)[56] and the fluorescence intensity analysis over diffusion time[57]. In both cases it is important to make several assumptions in order to choose the right diffusion model for the data analysis. In free solution and in absence of any interactions with other target biomolecules, the diffusion process is governed by Stokes-Einstein relation:

$$D_0 = \frac{k_B T}{6\pi\eta R_h} \approx {N_0}^{-\frac{1}{2}} \qquad (1)$$

where k_B is the Boltzmann constant, T is the temperature in kelvin, η is the solvent viscosity, R_h is the hydrodynamic radius of the diffusing molecule and N_0 is the crosslinks number.

In hydrogels, the diffusion is explained by different models, related to the nature of the diffusing biomolecule. Oligonucleotides, for example, are considered as Gaussian chain when $R_g < a/2$ (where Rg is the gyration radius and a is mean gel pore size), the diffusion coefficient is described by Zimm model[58], where the macromolecule migrates in ellipsoidal conformation[59], described as follows:

$$D_0 = 0.196\ \frac{k_B T}{\eta R_h} \approx {N_0}^{-\frac{1}{2}} \qquad (2)$$

If $Rg > a/2$, the reptation theory describes the movement of an unattached chain by Brownian motion in a multi-chain system forming the gel. The lateral movement of the chain is limited

by gel fibers with a resulting loss of entropy that forces the chain to migrate inside a tube with length $L = Na$, where N is the number of pore occupied by the chain. In such scenario:

$$D_0 = \frac{k_B T a^2}{3{N_k}^2 \zeta_k b^2} \approx {N_0}^{-\frac{1}{2}} \qquad (3)$$

where a represents the mean pore size, N_k is the the number of Kuhn segments, ζ_k is the friction coefficient of a Kuhn segments, and b is the Kuhn length. For proteins considered as rigid beads, the stochastic model proposed by Ongston et al.[60] address the diffusion of spherical particles in a fibres array with:

$$\frac{D}{D_0} = \exp\left(\frac{-\phi^{\frac{1}{2}} R_h}{r_f}\right) \qquad (4)$$

where D_0 is the diffusion coefficient in solution, r_f the fibre radius and ϕ is the volume fraction of fibres.

In order to experimentally evaluate the diffusion coefficient of various solutes in polymeric systems, Fluorescence Correlation Spectroscopy (FCS) has been demonstrated to be one of the most reliable technique. FCS can measure the diffusion of nanomolar solute concentrations allowing to determine the diffusivity of fluorescent probes and the number concentration of fluorescent solutes in a sample, a very challenging analysis with other techniques. The length of FCS measurements is typically on the order of minutes as opposed to standard bulk diffusion techniques which require hours to days. Most importantly, FCS allows for direct estimation of solute–hydrogel and solute–solute interactions, hydrogel matrix heterogeneity, and hydrogel dynamics such as swelling behaviour. FCS measures fluctuations in the fluorescence intensity of a small illuminated sample volume to target solutes moving through this volume. The recorded fluctuations are then correlated in time by a time-delayed correlation function which indicates the concentration and translational diffusion coefficient of the fluorescent solute[61,62]. Most FCS applications include the dynamics of single solutes or interactions between solutes in solution[63,64], in sol–hydrogel films[65], on surfaces[66] or to probe cell membrane organization and dynamics[67,68]. Only recent advances of FCS have allowed researchers to expand this technique for probing diffusion in living tissue and hydrogels[69]. It has been used to determine anomalous diffusion in polymer solutions[70], normal diffusion in agarose hydrogels[71,72], controlled release from peptide hydrogel scaffolds[73], as well as to probe structural changes in

polymer hydrogels. These studies have established the utility of FCS as a tool to measure solute diffusivity on the microscopic level in complex environments.

1.3.2 Hydrogels porosity and mesh size

The control of the hydrogel structure at a molecular level influences how a molecule moves inside the matrix and its accessibility to capture probes immobilized within the network. The access of target molecules to the immobilized ligands has to be assured while maintaining a structural integrity of the hydrogel matrix. This prerequisite defines the need to optimize the monomer composition and the porosity and swelling behaviour of the final hydrogel. In general, swelling behaviour and porosity can be easily tuned according to the starting material properties (i.e., monomer, porogens and crosslinkers concentrations) or, in case of external stimuli responsive hydrogels, it is also possible to implement the dynamic change of the porosity varying pH, ionic strength or temperature. For example, thermo-responsive hydrogels are used as an injectable depot system for the delivery of drugs or cells[74,75]. Other stimuli-responsive hydrogels are also reported as novel detection systems for biosensing applications[76,77]. In particular, the physical changes of the hydrogel such as a volume change and a sol-gel transition can be an excellent indication for the detection of target analytes without the use of analytical equipment[78,79]. Usually, for diagnostic applications, hydrogels are designed to accommodate a capture molecule inside a non-fouling network with a predetermined mesh size or porosity with a cut-off for certain molecules known as interferents.

In the case of crosslinked hydrogel with known chain lengths, the mesh size can be evaluated theoretically through a network characterization basing on their swelling behaviour, while in case of hydrogel networks deformed or modified by the presence of inert porogens or cleavable crosslinkers, it is necessary to evaluate experimentally the porosity. For this purpose, from the literature emerge many promising techniques to evaluate hydrogel porosity such as NMR cryo-porometry[80], DSC thermo-porometry[81] or cryo-SEM image analysis[82,83]. The characterization of the network structure of a hydrogel passes through the determination of the polymer fraction ($v_{2,s}$), the molecular weight of the polymer chain between two neighbouring cross-linking points (M_c) and the correlation distance between them, also known as mesh size (ξ)[84,85] (Figure 1.4).

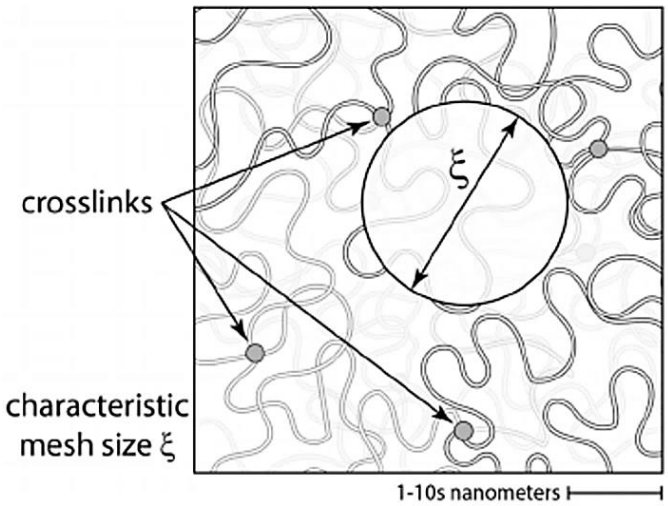

Figure 1.4: Schematic illustration of hydrogel characteristic mesh size[86]

The nature and the amount of polymer fraction defines how a hydrogel is capable to imbibe and retain water, while the M_c and ξ are averaged parameters that defines the accessibility and the transport of molecular species in the network. However, all these parameters are described theoretically by the equilibrium swelling theory and the rubber elasticity, while a variety of techniques are available to experimentally measure and verify them[87,88]. For bulk hydrogels, the structural characterization is usually carried out measuring the degree of hydration by weighting the amount of water absorbed by the polymer and converting it in the volumetric fraction according to the so-called equilibrium swelling theory developed by Flory and Rehner and then modified by Peppas and Merrill[89]. However, this approach is not simple for microparticles, due to difficulties in the canonical measurements of swelling[90]. Recently, Battista et al. demonstrated the direct determination of swelling on core/shell microgels through atomic force microscopy (AFM): M_c and ξ were determined from the topographic imaging measuring the actual volume by "Laplacian volume" occupied by the single microparticles[91]. Once volumes were determined, swelling ratio (Q) was obtained for both swollen (Q_s) and relaxed state (Q_r):

$$Q_s = \frac{V_s}{V_d} \qquad (5)$$

$$Q_r = \frac{V_r}{V_d} \qquad (6)$$

Where V_d is the dry volume, V_s is the volume in the swollen state and V_r in the relaxed state. These data can be considered as the starting input for the equation to calculate the molecular weight between cross-links in presence of water ($\overline{M_c}$) according to the following equation[92]:

$$\frac{1}{\overline{M_c}} = \frac{1}{\overline{M_n}} - \frac{\left(\frac{\bar{v}}{v_1}\right)\left[ln\left(1-v_{2,s}\right)+v_{2,s}+\chi_1 {v_{2,s}}^2\right]}{v_{2,r}\left[\left(\frac{v_{2,s}}{v_{2,r}}\right)^{\frac{1}{3}}-\left(\frac{v_{2,s}}{2v_{2,r}}\right)\right]} \qquad (7)$$

where $\overline{M_n}$ is the average molecular weight of the un-crosslinked polymer, χ is the Flory parameter, v is the specific volume of the polymer. In particular, v_1 is the molar volume of water[93], $v_{2,s}$ and $v_{2,r}$ represent respectively the polymer volume fraction in the swollen and relaxed state. The relaxed state is defined as the state of the polymer immediately after cross-linking, but before swelling and is mathematically the inverse of swelling ratio (Q), calculated as follows:

$$v_{2,r} = \frac{V_d}{V_r} \qquad (8)$$

$$v_{2,s} = \frac{V_d}{V_s} \qquad (9)$$

Once $\overline{M_c}$ was calculated by Peppas and Merril equation, the mesh size can be derived as follows:

$$\xi = {v_{2,s}}^{-\frac{1}{3}} \left(\bar{r}_0^2\right)^{\frac{1}{2}} \qquad (10)$$

where $\bar{r}_0^2$ is the value of the end-to-end distance of polymer chains in the unperturbed state and it is calculated through the Flory characteristic ratio, or rigidity factor, C_n[94]:

$$C_n = \frac{\bar{r}_0^2}{Nl^2} \qquad (11)$$

Where l is the C-C bond length (l = 0.146 Å)[95,96] and N is the number of links of the chains, given by the following equation:

$$N = \frac{2\overline{M_c}}{M_r} \qquad (12)$$

where Mr is the molecular weight of the repeating unit of the polymer.

1.3 Hydrogel microparticles in diagnostics

In recent years, there has been an ever-increasing interest in technologies based on hydrogel microparticles for a wide variety of biotechnology applications, especially in the detection field, as shown in figure 1.5. The most attractive characteristic of hydrogels relies on the flexible synthetic approaches to design multifunctional particles provided with suitable encoding and sensing capabilities toward specific targets such as pollutants[97] or clinically relevant biomarkers[98,99]. The use of microparticles in diagnostics revolutionized the existing methodologies in term of time and cost, sample amount and sensitivity. Microarrays and ELISAs mainly benefited from the microparticles bringing to the market well assessed technologies increasingly easier to perform[85].

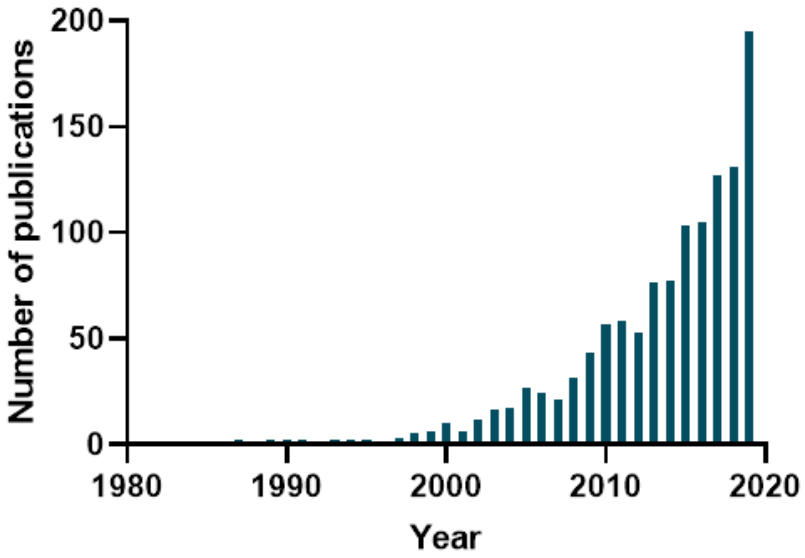

Figure 1.5: Histogram showing the increase in publications related to the keywords "hydrogel detection" during the past 40 years. PubMed data.

The three-dimensional, and eventually responsive, nature of the polymer networks plays a key role in bead-based assays, although the design of hydrogel materials in biosensing applications highlights serval difficulties. Particularly relevant are the issues related to the mass transport

inside the network, closely connected to swelling behaviour, probe density and diffusion of solutes (Figure 1.6).

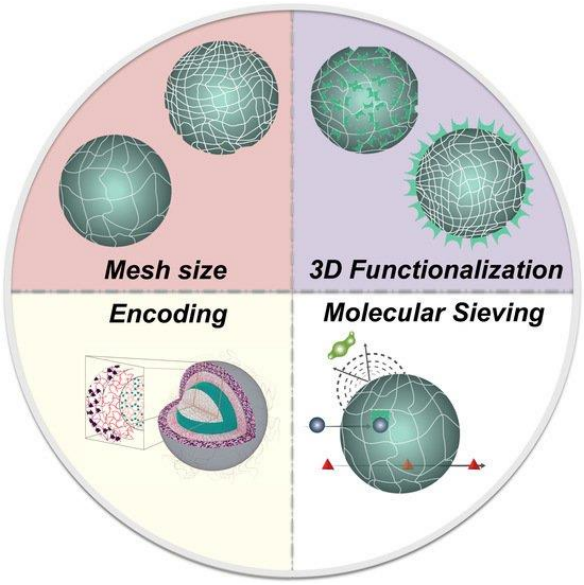

Figure 1.6: Schematic illustration of hydrogel microparticles for diagnostic and its principal characteristics[100].

Due to their three-dimensional nature and increased effective surface area, hydrogel substrates offer higher capacity for probe immobilization in comparison to surface-based systems such as planar microarrays or polystyrene beads. In fact, in a series of studies where probe-functionalized polyacrylamide hydrogel pads were immobilized on a surface for DNA detection, hydrogels were found to be superior for biosensing relative to rigid two-dimensional planar surfaces[101–104]. In order to selectively capture a specific target, a proper functionalization of hydrogels results vital. Several methods to functionalize the gels have been explored, ranging from in situ functionalization at the time of synthesis to post-synthesis functionalization utilizing functional groups in the gel[101].

Another important characteristic for hydrogels in diagnostics is their porosity. The gel network can be tuned to act as a molecular sieving, representing a physical barrier to the entrance of larger interfering molecules and thus enhancing the signal/noise ratio. Moreover, target diffusion and probe/target interaction kinetics in hydrogel substrates were first extensively studied and modelled for hydrogel pads[98,99] and hydrogel posts[106].

Finally, one of the major concerns in multiplex analysis is the encoding. In case of 2D arrays, the identity of each probe is determined by positional encoding, where the location on the grid univocally identifies the target[107]. The great advantage of using microspheres relies on the flexibility of manipulation in three dimensions, but this precludes the positional encoding. Therefore, each microparticle is endowed by a unique code that defines the capture molecules conjugate on the surfaces. The encoding must address a number of requirements: it must be optically read, inert, capable to produce a large number of unique combinations, implementable on micron-scale materials and suitable for low-cost mass production. Most of the bead-based assays commercially available are comprised of polymer microspheres with one or more fluorescent dyes physically entrapped. For the sake of multiplex assays, a reporter dye is required to emit in a region of the spectrum free from the emission of encoding. in addition to fluorescent codes, other widely used techniques are shape[108–110] and graphical[111,112] encoding.

1.4 Aim and outline of dissertation

In biosensor field there is an ever-increasing interest in novel microparticles production and engineering to improve the detection in complex fluids. Although different types of microparticles are already on the market (e.g., fluorescently labelled and magnetic), there is a need for new materials with high chemical flexibility to introduce the right functionalities and with a large porosity to improve accessibility of the biomolecules into the three-dimensional bulk. In order to achieve this goal, we focused on the synthesis and optimization of new hydrogel-based materials which combine biocompatibility, stability and low non-specific interactions with biomolecule, essential features for diagnostic applications. The hydrogel microparticles realized have been tested performing an in-gel sandwich immuno-assay on human IgG in complex fluids and a competitive assay on a small toxic molecule (TCDD dioxin). Finally, this novel hydrogel microparticles have been trapped inside a microfluidic device for on-chip detection applications, taking a first step towards the development of a fast and easy point-of-care testing platform.

In **chapter 2** we focused on the characterization of the microfluidic droplet generation in a T-junction device in order to synthesize monodisperse cleavable hydrogel microparticles with fine controlled physical and chemical properties, such as size, shape and composition to perform in-gel immuno-assays.

In **chapter 3** we concentrated on development of a simple technique for one-step generation of porous and reactive PEG hydrogels. To this purpose, we have developed a new class of porous hydrogel particles through the use of a specific cleavable cross-linker (N,N′(1,2Dihydroxyethylene)bisacrylamide, DHEBA). Equilibrium volumetric swelling, monitoring of swollen radius and amount of aldehydes formed over time allow to optimize cleavage reaction conditions. Moreover, NMR cryoporometry and equilibrium partitioning of fluorescent probes give information about the accessibility of the biomolecules inside the polymeric network.

In **chapter 4** the cleavable hydrogel microparticles synthesized and characterized are used to develop and optimize an innovative in-gel sandwich assay for the detection of human immunoglobulin G (IgG) in biological fluids such as human serum and urine.

In **chapter 5**, we focused the development of an in-gel competitive assay for the detection of the tetrachlorodibenzo-para-dioxin (TCDD), a dangerous and toxic compound commonly referred to as dioxin.

Finally, in **chapter 6,** we present the design, fabrication and testing of an innovative microfluidic device for on-chip detection. This device is based on the hydrodynamic trapping of the hydrogel microparticles and is realized via conventional replica micro-molding with inexpensive techniques and materials. Conclusions and future perspectives are briefly presented and discussed in **chapter 7**.

1.5 References

1. Ahmed, E. M. Hydrogel: Preparation, characterization, and applications: A review. *Journal of Advanced Research* vol. 6 105–121 (2015).

2. Ranjha, N. M., Umbreen, A. & Qureshi, F. Preparation and characterization of crosslinked acrylic acid/hydroxypropyl methyl cellulose hydrogels for drug delivery.

3. De, S. K. *et al.* Equilibrium Swelling and Kinetics of pH-Responsive Hydrogels: Models, Experiments, and Simulations. *J. MICROELECTROMECHANICAL Syst.* **11**, (2002).

4. Peppas, N. A., Keys, K. B., Torres-Lugo, M. & Lowman, A. M. Poly(ethylene glycol)-containing hydrogels in drug delivery. *J. Control. Release* **62**, 81–87 (1999).

5. Peppas, N. A., Hilt, J. Z., Khademhosseini, A. & Langer, R. Hydrogels in Biology and Medicine: From Molecular Principles to Bionanotechnology. *Adv. Mater.* **18**, 1345–

1360 (2006).

6. Lee, K. Y. & Mooney, D. J. Hydrogels for Tissue Engineering. *Chem. Rev.* **101**, 1869–1880 (2001).

7. Sannino, A. *et al.* Synthesis and characterization of macroporous poly(ethylene glycol)-based hydrogels for tissue engineering application. *J. Biomed. Mater. Res. - Part A* **79**, 229–236 (2006).

8. Helgeson, M. E., Chapin, S. C. & Doyle, P. S. Hydrogel microparticles from lithographic processes: Novel materials for fundamental and applied colloid science. *Current Opinion in Colloid and Interface Science* vol. 16 106–117 (2011).

9. Rubina, A. Y., Kolchinsky, A., Makarov, A. A. & Zasedatelev, A. S. Why 3-D? Gel-based microarrays in proteomics. *Proteomics* **8**, 817–831 (2008).

10. Amin, S., Rajabnezhad, S. & Kohli, K. Hydrogels as potential drug delivery systems Oral Bioavailability enhancement of Exemestane View project Development and Validation of a Stability-Indicating LC Method for Simultaneous Analysis of Aceclofenac and Paracetamol in Conventional Tablets and in Microsphere Formulations View project Hydrogels as potential drug delivery systems. *Sci. Res. Essay* **3**, 1175–1183 (2009).

11. Qiu, Y. & Park, K. Environment-sensitive hydrogels for drug delivery ☆. (2012) doi:10.1016/j.addr.2012.09.024.

12. Mahinroosta, M., Farsangi, Z., … A. A.-M. today & 2018, undefined. Hydrogels as intelligent materials: A brief review of synthesis, properties and applications. *Elsevier*.

13. Smith, M. H., Herman, E. S. & Lyon, L. A. Network deconstruction reveals network structure in responsive microgels. *J. Phys. Chem. B* **115**, 3761–3764 (2011).

14. Hoare, T. & Pelton, R. Dimensionless plot analysis: A new way to analyze functionalized microgels. *J. Colloid Interface Sci.* **303**, 109–116 (2006).

15. Langer, R. & Tirrell, D. A. Designing materials for biology and medicine. *Nature* vol. 428 487–492 (2004).

16. Collier, J. H. *et al.* Thermally and photochemically triggered self-assembly of peptide

hydrogels [11]. *Journal of the American Chemical Society* vol. 123 9463–9464 (2001).

17. Akiyoshi, K. *et al.* Controlled association of amphiphilic polymers in water: Thermosensitive nanoparticles formed by self-assembly of hydrophobically modified pullulans and poly(N-isopropylacrylamides). *Macromolecules* **33**, 3244–3249 (2000).

18. Li, Y. & Tanaka, T. Phase transitions of gels. *Annu. Rev. Mater. Sci.* **22**, 243–277 (1992).

19. Hennink, W., reviews, C. van N.-A. drug delivery & 2012, undefined. Novel crosslinking methods to design hydrogels. *Elsevier*.

20. Eddington, D., reviews, D. B.-A. drug delivery & 2004, undefined. Flow control with hydrogels. *Elsevier*.

21. Bale, S., Banks, V., Haglestein, S. & Harding, K. G. A comparison of two amorphous hydrogels in the debridement of pressure sores. *J. Wound Care* **7**, 65–68 (1998).

22. Kurt, B., Gulyuz, U., Demir, D. D. & Okay, O. High-strength semi-crystalline hydrogels with self-healing and shape memory functions. *Eur. Polym. J.* **81**, 12–23 (2016).

23. Li, X., Wu, W., Polymers, W. L.-C. & 2008, undefined. Synthesis and properties of thermo-responsive guar gum/poly (N-isopropylacrylamide) interpenetrating polymer network hydrogels. *Elsevier*.

24. Zhang, X.-Z., Lewis, P. J. & Chu, C.-C. Fabrication and characterization of a smart drug delivery system: microsphere in hydrogel. *Biomaterials* **26**, 3299–3309 (2005).

25. Mocanu, G. *et al.* New anionic crosslinked multi-responsive pullulan hydrogels. *Elsevier*.

26. Saunders, J. R. *et al.* Modeling Theories of Intelligent Hydrogel Polymers Modeling of limited Oxygen Nitrification Processes View project EMB of micro annular plate View project Modeling Theories of Intelligent Hydrogel Polymers. *Artic. J. Comput. Theor. Nanosci.* **5**, 1–19 (2008).

27. Jeong, B., Bae, Y., Lee, D., Nature, S. K.- & 1997, undefined. Biodegradable block copolymers as injectable drug-delivery systems. *nature.com*.

28. Percec, V., Bera, T. K. & Butera, R. J. A new strategy for the preparation of supramolecular neutral hydrogels. *Biomacromolecules* **3**, 272–279 (2002).

29. Baker, J., Blanch, H. W., Prausnitz, J. M. & Org, E. *Lawrence Berkeley National Laboratory Recent Work Title Swelling Properties of Acrylamide-based Ampholytic Hydrgels: Comparison of Experiment with Theory Permalink https://escholarship.org/uc/item/1gx881n4 Publication Date*. https://escholarship.org/uc/item/1gx881n4 (1994).

30. Hsu, M. N., Wei, S.-C., Phan, D.-T., Zhang, Y. & Chen, C.-H. Nano-in-Micro Smart Hydrogel Composite for a Rapid Sensitive Immunoassay. *Adv. Healthc. Mater.* 1801277 (2019) doi:10.1002/adhm.201801277.

31. Padmavathi, N. C. & Chatterji, P. R. Structural characteristics and swelling behavior of poly(ethylene glycol) diacrylate hydrogels. *Macromolecules* **29**, 1976–1979 (1996).

32. Hutanu, D. Recent Applications of Polyethylene Glycols (PEGs) and PEG Derivatives. *Mod. Chem. Appl.* **02**, 2–7 (2014).

33. Zalipsky, S. & Harris, J. M. Introduction to Chemistry and Biological Applications of Poly(ethylene glycol). *ACS Symp. Ser.* **680**, 1–13 (1997).

34. Harris, J. M., Sedaghat-Herati, M. R., Sather, P. J., Brooks, D. E. & Fyles, T. M. Synthesis of New Poly(Ethylene Glycol) Derivatives. in *Poly(Ethylene Glycol) Chemistry* 371–381 (Springer US, 1992). doi:10.1007/978-1-4899-0703-5_22.

35. Nguyen, K. T. & West, J. L. Photopolymerizable hydrogels for tissue engineering applications. *Biomaterials* **23**, 4307–4314 (2002).

36. Zhang, H. *et al.* Uniform polysaccharide composite microspheres with controllable network by microporous membrane emulsification technique. *Anal. Bioanal. Chem.* **410**, 4331–4341 (2018).

37. Ding, S., Serra, C. A., Vandamme, T. F., Yu, W. & Anton, N. Double emulsions prepared by two-step emulsification: History, state-of-the-art and perspective. (2018) doi:10.1016/j.jconrel.2018.12.037.

38. Feng, X., Pelton, R., Leduc, M. & Champ, S. Colloidal complexes from poly(vinyl amine) and carboxymethyl cellulose mixtures. *Langmuir* **23**, 2970–2976 (2007).

39. Jones, C. D. & Lyon, L. A. Synthesis and characterization of multiresponsive core-shell microgels. *Macromolecules* **33**, 8301–8306 (2000).

40. Burkert, S., Schmidt, T., Gohs, U., Chemistry, H. D.-… P. and & 2007, undefined. Cross-linking of poly (N-vinyl pyrrolidone) films by electron beam irradiation. *Elsevier*.

41. Roh, Y. H., Lee, H. J. & Bong, K. W. Microfluidic Fabrication of Encoded Hydrogel Microparticles for Application in Multiplex Immunoassay. *Biochip Journal* vol. 13 64–81 (2019).

42. Luo, R.-C. & Chen, C.-H. Structured Microgels through Microfluidic Assembly and Their Biomedical Applications. *Soft* **01**, 1–23 (2012).

43. Choi, C. H., Jung, J. H., Hwang, T. S. & Leezz, C. S. In situ microfluidic synthesis of monodisperse PEG microspheres. *Macromol. Res.* **17**, 163–167 (2009).

44. Rossow, T. *et al.* Controlled synthesis of cell-laden microgels by radical-free gelation in droplet microfluidics. *J. Am. Chem. Soc.* **134**, 4983–4989 (2012).

45. Walther, B., Cramer, C., Tiemeyer, A., … L. H.-J. of colloid and & 2005, undefined. Drop deformation dynamics and gel kinetics in a co-flowing water-in-oil system. *Elsevier*.

46. Wang, J. T., Wang, J. & Han, J. J. Fabrication of advanced particles and particle-based materials assisted by droplet-based microfluidics. *Small* **7**, 1728–1754 (2011).

47. Celetti, G., Di Natale, C., Causa, F., Battista, E. & Netti, P. A. Functionalized poly(ethylene glycol) diacrylate microgels by microfluidics: In situ peptide encapsulation for in serum selective protein detection. *Colloids Surfaces B Biointerfaces* **145**, 21–29 (2016).

48. Keller, S., Teora, S. P., Hu, G. X., Nijemeisland, M. & Wilson, D. A. High-Throughput Design of Biocompatible Enzyme-Based Hydrogel Microparticles with Autonomous Movement. *Angew. Chemie* **130**, 9962–9965 (2018).

49. Liu, E. Y., Jung, S., Weitz, D. A., Yi, H. & Choi, C. H. High-throughput double emulsion-based microfluidic production of hydrogel microspheres with tunable chemical functionalities toward biomolecular conjugation. *Lab Chip* **18**, 323–334 (2018).

50. Lewis, C. L. *et al.* Microfluidic Fabrication of Hydrogel Microparticles Containing Functionalized Viral Nanotemplates. *Langmuir* **26**, 13436–13441 (2010).

51. Haghgooie, R., Toner, M. & Doyle, P. S. Squishy non-spherical hydrogel microparticles. *Macromol. Rapid Commun.* **31**, 128–134 (2010).

52. Amalvy, J. I. *et al.* Synthesis and characterization of novel pH-responsive microgels based on tertiary amine methacrylates. *Langmuir* **20**, 8992–8999 (2004).

53. Dendukuri, D., Pregibon, D. C., Collins, J., Hatton, T. A. & Doyle, P. S. Continuous-flow lithography for high-throughput microparticle synthesis. *Nat. Mater.* **5**, 365–369 (2006).

54. Yánez-Sedeño, P., Campuzano, S. & Pingarrón, J. M. *Janus particles for (bio)sensing*.

55. Dendukuri, D., Gu, S. S., Pregibon, D. C., Hatton, T. A. & Doyle, P. S. Stop-flow lithography in a microfluidic device. *Lab Chip* **7**, 818–828 (2007).

56. Zustiak, S. P., Boukari, H. & Leach, J. B. Solute diffusion and interactions in cross-linked poly(ethylene glycol) hydrogels studied by Fluorescence Correlation Spectroscopy. *Soft Matter* **6**, 3609–3618 (2010).

57. Zhao, Z., Al-Ameen, M. A., Duan, K., Ghosh, G. & Fujiou Lo, J. On-chip porous microgel generation for microfluidic enhanced VEGF detection. *Biosens. Bioelectron.* **74**, 305–312 (2015).

58. Zwanzig, R. Theoretical basis for the Rouse-Zimm model in polymer solution dynamics. *J. Chem. Phys.* **60**, 2717–2720 (1974).

59. Pregibon, D. C. & Doyle, P. S. Optimization of Encoded Hydrogel Particles for Nucleic Acid Quantification. *Anal. Chem.* **81**, 4873–4881 (2009).

60. Ogston, A., … B. P.-… S. of L. A. & 1973, undefined. On the transport of compact particles through solutions of chain-polymers. *royalsocietypublishing.org*.

61. Michelman-Ribeiro, A., Boukari, H., Nossal, R. & Horkay, F. Structural changes in polymer gels probed by fluorescence correlation spectroscopy. *Macromolecules* **37**, 10212–10214 (2004).

62. Krichevsky, O. & Bonnet, G. Fluorescence correlation spectroscopy: The technique and its applications. *Reports Prog. Phys.* **65**, 251–297 (2002).

63. Van Rompaey, E., Engelborghs, Y., Sanders, N., De Smedt, S. C. & Demeester, J.

Interactions between oligonucleotides and cationic polymers investigated by fluorescence correlation spectroscopy. *Pharm. Res.* **18**, 928–936 (2001).

64. Bosco, S. J., Zettl, H., Crassous, J. J., Ballauff, M. & Krausch, G. Interactions between methyl cellulose and sodium dodecyl sulfate in aqueous solution studied by single molecule fluorescence correlation spectroscopy. *Macromolecules* **39**, 8793–8798 (2006).

65. Martin-Brown, S. A., Fu, Y., Saroja, G., Collinson, M. M. & Higgins, D. A. Single-molecule studies of diffusion by oligomer-bound dyes in organically modified sol-gel-derived silicate films. *Anal. Chem.* **77**, 486–494 (2005).

66. Zhao, J. & Granick, S. How Polymer Surface Diffusion Depends on Surface Coverage. (2007) doi:10.1021/ma062104l.

67. Wawrezinieck, L., Rigneault, H., Marguet, D., journal, P. L.-B. & 2005, undefined. Fluorescence correlation spectroscopy diffusion laws to probe the submicron cell membrane organization. *Elsevier*.

68. Takahashi, Y., Bark, N., Kinjo, M. & Rigler, R. Fluorescence Correlation Spectroscopy (FCS) Analysis of Human Red Blood Cell System. in *Optical Review* vol. 10 596–599 (Optical Society of Japan, 2003).

69. Tatarkova, S. A., Kamra Verma, A., Berk, D. A. & Lloyd, C. J. Quantitative fluorescence microscopy of macromolecules in gel and biological tissue. *Phys. Med. Biol.* **50**, 5759–5768 (2005).

70. Masuda, A., Ushida, K., and, T. O.-J. of P. & 2006, undefined. New fluorescence correlation spectroscopy (FCS) suitable for the observation of anomalous diffusion in polymer solution: Time and space dependences of diffusion. *Elsevier*.

71. Fatin-Rouge, N., Starchev, K., journal, J. B.-B. & 2004, undefined. Size effects on diffusion processes within agarose gels. *Elsevier*.

72. Fatin-Rouge, N., Wilkinson, K. J. & Buffle, J. Combining Small Angle Neutron Scattering (SANS) and Fluorescence Correlation Spectroscopy (FCS) measurements to relate diffusion in agarose gels to structure. *J. Phys. Chem. B* **110**, 20133–20142 (2006).

73. Designed Research; S, S. Z. K., Performed Research; S, Y. N. K. & Pnas, S. Z.

Controlled release of functional proteins through designer self-assembling peptide nanofiber hydrogel scaffold. vol. 106 www.pnas.orgcgidoi10.1073pnas.0807506106 (2009).

74. Li, W., Yan, Z., Ren, J., Reviews, X. Q.-C. S. & 2018, undefined. Manipulating cell fate: dynamic control of cell behaviors on functional platforms. *pubs.rsc.org*.

75. Lee, Y. *et al.* Thermo-sensitive, injectable, and tissue adhesive sol-gel transition hyaluronic acid/pluronic composite hydrogels prepared from bio-inspired catechol-thiol reaction. doi:10.1039/b919944f.

76. Shigemitsu, H. *et al.* Preparation of supramolecular hydrogel–enzyme hybrids exhibiting biomolecule-responsive gel degradation. *Nat. Protoc.* **11**, (2016).

77. Lee, S.-H., Kim, T. H., Lima, M. D., Baughman, R. H. & Kim, S. J. Biothermal sensing of a torsional artificial muscle †. *Nanoscale Commun. Cite this Nanoscale* **8**, 3248 (2016).

78. Wilson, A. N. & Guiseppi-Elie, A. Bioresponsive hydrogels. *Adv. Healthc. Mater.* **2**, 520–532 (2013).

79. Lee, S. J. & Park, K. Synthesis and Characterization of Sol-Gel Phase-reversible Hydrogels Sensitive to Glucose. *J. Mol. Recognit.* **9**, 549–557 (1996).

80. Park, J. *et al.* Microfluidic fabrication and permeation behaviors of uniform zwitterionic hydrogel microparticles and shells. *J. Colloid Interface Sci.* **426**, 162–169 (2014).

81. Iza, M., Woerly, S., Danumah, C., Kaliaguine, S. & Bousmina, M. Determination of pore size distribution for mesoporous materials and polymeric gels by means of DSC measurements: Thermoporometry. *Polymer (Guildf).* **41**, 5885–5893 (2000).

82. Aston, R., Sewell, K., Klein, T., Lawrie, G. & Grøndahl, L. Evaluation of the impact of freezing preparation techniques on the characterisation of alginate hydrogels by cryo-SEM. *European Polymer Journal* vol. 82 1–15 (2016).

83. Yoshinobu, M., Morita, M., Higuchi, M. & Sakata, I. Morphological study of hydrogels of cellulosic super water absorbents by CRYO-SEM observation. *J. Appl. Polym. Sci.* **53**, 1203–1209 (1994).

84. Fernández-Barbero, A. *et al.* Gels and microgels for nanotechnological applications. *Advances in Colloid and Interface Science* vols 147–148 88–108 (2009).

85. Kryscio, D. R. & Peppas, N. A. Critical review and perspective of macromolecularly imprinted polymers. *Acta Biomaterialia* vol. 8 461–473 (2012).

86. Dunn, A. C. *et al.* Kinetics of aqueous lubrication in the hydrophilic hydrogel Gemini interface. *Proc. Inst. Mech. Eng. Part H J. Eng. Med.* **229**, 889–894 (2015).

87. Anseth, K. S., Bowman, C. N. & Brannon-Peppas, L. Mechanical properties of hydrogels and their experimental determination. *Biomaterials* **17**, 1647–1657 (1996).

88. Brannon-Peppas, L. & Peppas, N. A. Equilibrium swelling behavior of pH-sensitive hydrogels. *Chem. Eng. Sci.* **46**, 715–722 (1991).

89. Kofinas, P., Athanassiou, V., Biomaterials, E. M.- & 1996, undefined. Hydrogels prepared by electron irradiation of poly (ethylene oxide) in water solution: unexpected dependence of cross-link density and protein diffusion coefficients on. *Elsevier*.

90. Marek, S., Conn, C., Polymer, N. P.- & 2010, undefined. Cationic nanogels based on diethylaminoethyl methacrylate. *Elsevier*.

91. Battista, E., Mazzarotta, A., Causa, F., Cusano, A. M. & Netti, P. A. Core-shell microgels with controlled structural properties. *Polym. Int.* **65**, 747–755 (2016).

92. Echeverria, C., Peppas, N., Matter, C. M.-S. & 2012, undefined. Novel strategy for the determination of UCST-like microgels network structure: effect on swelling behavior and rheology. *pubs.rsc.org*.

93. Thakur, A., Wanchoo, R. K. & Singh, P. *Structural Parameters and Swelling Behavior of pH Sensitive Poly(acrylamide-co-acrylic acid) Hydrogels*.

94. Leach, S. P. Z. and J. B. Hydrolytically degradable poly(ethylene glycol) hydrogel Biomacromolecules. *Biomacromolecules* **11**, 1348–1357 (2011).

95. Malana, M. A., Firdous, G., Javed, A., Zafar, Z. I. & Khan, M. S. Swelling kinetics and rheological characterization of methyl acrylate-vinyl acetate-acrylic acid hydrogels. *Asian J. Chem.* **26**, 1898–1904 (2014).

96. Zubtsov, D., Savvateeva, E., … A. R.-A. & 2007, undefined. Comparison of surface and

hydrogel-based protein microchips. *Elsevier*.

97. Manikas, A. C., Aliberti, A., Causa, F., Battista, E. & Netti, P. A. Thermoresponsive PNIPAAm hydrogel scaffolds with encapsulated AuNPs show high analyte-trapping ability and tailored plasmonic properties for high sensing efficiency. *J. Mater. Chem. B* **3**, 53–58 (2015).

98. Appleyard, D. C., Chapin, S. C. & Doyle, P. S. Multiplexed Protein Quantification with Barcoded Hydrogel Microparticles. *Anal. Chem.* **83**, 193–199 (2011).

99. Cusano, A. M. *et al.* Integration of binding peptide selection and multifunctional particles as tool-box for capture of soluble proteins in serum. *J. R. Soc. Interface* **11**, (2014).

100. Battista, E., Causa, F. & Netti, P. Bioengineering Microgels and Hydrogel Microparticles for Sensing Biomolecular Targets. *Gels* **3**, 20 (2017).

101. Proudnikov, D., Timofeev, E. & Mirzabekov, A. *Immobilization of DNA in Polyacrylamide Gel for the Manufacture of DNA and DNA±Oligonucleotide Microchips*. (1998).

102. Fotin, A. V., Drobyshev, A. L., Proudnikov, D. Y., Perov, A. N. & Mirzabekov, A. D. Parallel thermodynamic analysis of duplexes on oligodeoxyribonucleotide microchips. *Nucleic Acids Res.* **26**, 1515–1521 (1998).

103. Kolchinsky, A. M. *et al.* Gel-based microchips: History and prospects. *Molecular Biology* vol. 38 4–13 (2004).

104. Sorokin, N. V *et al.* Kinetics of Hybridization on Surface Oligonucleotide Microchips: Theory, Experiment, and Comparison with Hybridization on Gel-Based Microchips. *J. Biomol. Struct. Dyn.* **24**, 57–66 (2006).

105. khimiia, V. O.-B. & 2011, undefined. Semiconductor fluorescent nanocrystals (quantum dots) in biological biochips. *europepmc.org*.

106. Lee, A. G., Arena, C. P., Beebe, D. J. & Palecek, S. P. Development of Macroporous Poly(ethylene glycol) Hydrogel Arrays within Microfluidic Channels. *Biomacromolecules* **11**, 3316–3324 (2010).

107. Birtwell, S. & Morgan, H. Microparticle encoding technologies for high-throughput multiplexed suspension assays. *Integrative Biology* vol. 1 345–362 (2009).

108. Jang, E. & Koh, W. G. Multiplexed enzyme-based bioassay within microfluidic devices using shape-coded hydrogel microparticles. *Sensors Actuators, B Chem.* **143**, 681–688 (2010).

109. Park, S., Lee, H. J. & Koh, W.-G. Multiplex Immunoassay Platforms Based on Shape-Coded Poly(ethylene glycol) Hydrogel Microparticles Incorporating Acrylic Acid. *Sensors* **12**, 8426–8436 (2012).

110. Lee, W., Choi, D., Kim, J. H. & Koh, W. G. Suspension arrays of hydrogel microparticles prepared by photopatterning for multiplexed protein-based bioassays. *Biomed. Microdevices* **10**, 813–822 (2008).

111. Appleyard, D. C., Chapin, S. C., Srinivas, R. L. & Doyle, P. S. Bar-coded hydrogel microparticles for protein detection: Synthesis, assay and scanning. *Nat. Protoc.* **6**, 1761–1774 (2011).

112. Wilson, R., Cossins, A. R. & Spiller, D. G. Encoded microcarriers for high-throughput multiplexed detection. *Angewandte Chemie - International Edition* vol. 45 6104–6117 (2006).

2. On-Flow Hydrogel Microparticles Synthesis Via Microfluidic Droplet Generation

2.1 Introduction

The main issue in microparticles synthesis is to obtain a both narrow size distribution and a high production rate. From the literature, as the most promising technique to achieve this goal, emerges the microfluidic droplet generation. This technique has been extensively used to produce monodisperse microparticles[1–10] due to its numerous advantages such as: ease of control parameters that influence the final characteristics of the particles, high productivity, reproducibility and stability of the emulsion.

Droplet-based microfluidic devices present different geometries and characteristics (Figure 2.1). Droplet formation in microchannels has been mainly achieved using flow focusing, co-flow, T-junction and step emulsification combined with cross flow/co-flow techniques. The most easy-to-set geometry due to its simplicity still remains the T-junction. In fact, this geometry has been widely used in literature for droplet break up studies[14], uniform and monodisperse droplets production[26], nanoparticles encapsulation[27], single cells analysis[28,29], biomolecules detection[30] and drug discovery[31] to cite a few.

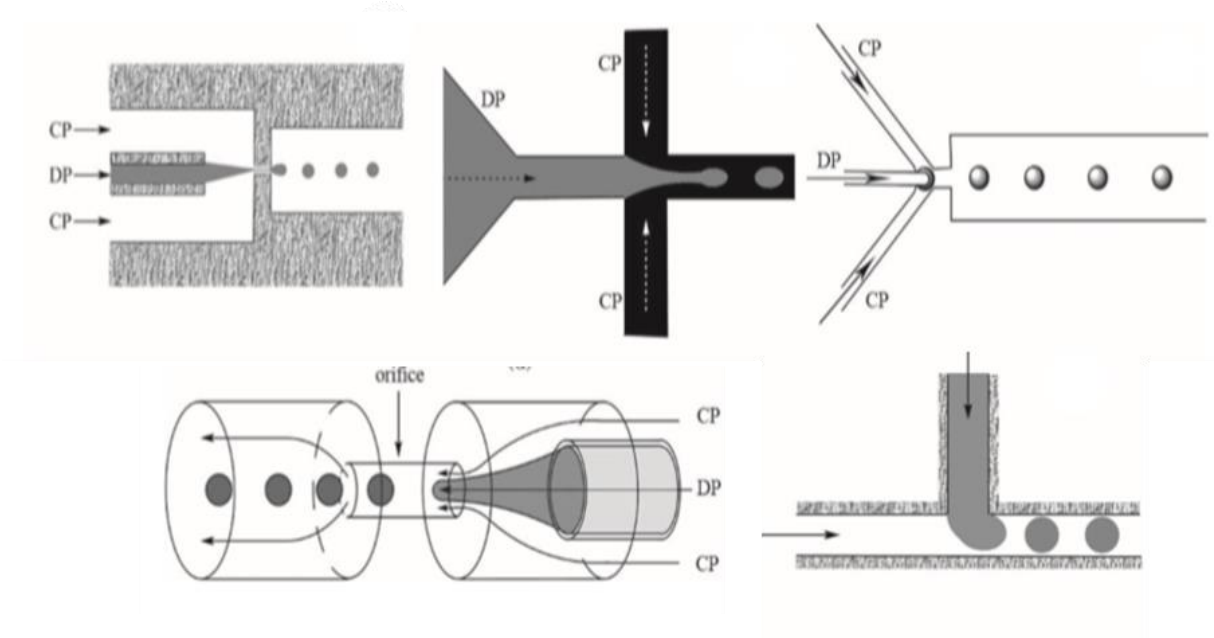

Figure 2.1: Most used geometries for droplet generation chips including T-Junction, X-junction and co-flow systems[21]

One of the most widely studied microfluidic geometries to generate droplets or bubbles is the T-junction, which presents a side arm that introduces a fluid to a main channel, where an immiscible phase flows. Thorsen et al.[11], described the formation of droplets in a T-junction device as a result of the competition between the shear forces acting to pinch a droplet off the emerging dispersed phase thread, and the interfacial tension acting on stabilising it. In this device, the size of the droplets is determined by numerous parameters including the relative flow rates of the two immiscible fluids, properties of the fluids (viscosities and interface tension), and the characteristic dimensions of the microchannels[12]. Higher flow rate ratios, greater viscosity of the continuous phase, lower interface tension, and smaller characteristic dimensions will result in the decrease of droplet size. Extensive studies have been carried out in literature to describe and characterise the break-up mechanism in a microfluidic T-junction, both in Newtonian and non-Newtonian systems[13–20].

There are different forces which play a role in the break-up process, such as:

- The interfacial tension which acts against the break-up;
- The drag force arising from the shear stress exerted by the flow of the continuous phase; This force promotes break-up, transferring kinetic energy to the tip of the discontinuous phase;
- The pressure's drop along the growing droplet;
- The inertial force exerted by the continuous fluid on the dispersed phase.

The relative effect of the viscous forces with respect to the interfacial tension between dispersed and continuous phases is represented by a dimensionless number called Capillary number (*Ca*, Eq. 1).

$$Ca = \frac{\mu U}{\gamma} \qquad (1)$$

where μ is the fluid viscosity, U represents the fluid velocity and γ is the interfacial tension between the two immiscible fluids.

In the microns length-scale both viscous stress and capillary pressure are enhanced, and the gravitational effect is negligible. Therefore, viscous and capillary forces become dominant over the others, if the characteristic length L is sufficiently small. According to this, *Ca* of the continuous phase (Ca_c) results to be the most frequently used dimensionless number in

characterizing microfluidic droplet generation. In microflows, Ca_c is usually in the range of 10^{-3} to 1. The capillary number can be varied by acting on the flow rate of the continuous phase or on the interfacial tension between the two immiscible fluids, modifying, for example, the surfactant concentration or the type of oil used.

As the flow rate of the fluids through the device, and so Ca_c, is increased[21,22], the microfluidic droplet generation passes through three regimes: squeezing, dripping and jetting, which appear sequentially.

Squeezing mode (Figure 2.2) occurs at low capillary number, such as $Ca_c < 10^{-2}$, where the interfacial forces dominate the shear stress, so the breaking mechanism is governed by a pressure gradient that comes along the growing droplet. In this flow regime, the droplets are bigger than the channel dimensions and their size is determined by the volumetric flow rate ratio of the two immiscible fluids, according to the following eq. 2 for rectangular cross-sections,

$$\frac{D}{l} = 1 + \alpha \frac{Qd}{Qc} \qquad (2)$$

where D is the length of the fluid segment, l is the width of the channel, Qd and Qc the flow rates of the discontinuous and continuous phase respectively.

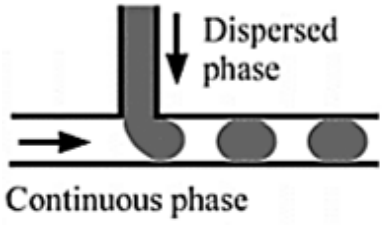

Figure 2.2: A schematic illustration of the squeezing regime in a T-junction chip

As capillary number increases ($Ca_c > 10^{-2}$), the regime transforms from squeezing to dripping (Figure 2.3), where viscous forces dominate over interfacial tension effects and, because of large viscous shear force, the dispersed phase breaks up before the droplet obstructs the

microchannels. In this regime, the droplet retains a spherical shape, smaller than the channel dimension[23].

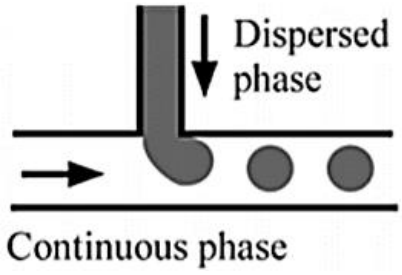

Figure 2.3: A schematic illustration of the dripping regime in a T-junction chip

In dripping regime, breakup occurs right at the dispersed phase nozzle, according to this mechanism: the discontinuous phase enters the main channel and propagates downstream occupying a fraction of the cross-section of the channel, broken then at the junction by the pressure drop along the growing droplet. The droplet so released flows downstream, while the tip of the discontinuous phase recoils to the junction and the process repeats. De Menech et. al[24] detailed the transition between squeezing and dripping. They corrected the classical scaling law, which considers exclusively the flow rates ratio, with a term depending from Ca_c (Eq. 3). Moreover, they found that the dependence of the droplets volume on Ca_c in the dripping regime is weak, typically with an exponent ranging from -0.1 to -0.4.

$$\frac{D}{l} = \alpha\left(\frac{Q_d}{Q_c}\right)^x (Ca_c)^y \qquad (3)$$

where Ca_c is the capillary number of the continuous phase, D is the length of the fluid segment, l is the width of the channel, Qd and Qc the flow rates of the discontinuous and continuous phase respectively and α, x and y are three fitting parameters depending on the specific droplet generation system ($0 < x < 1$, $-1 < y < 0$).

Qualitatively, microfluidic systems in dripping regime typically produce monodisperse droplets and their volume could be effectively controlled with the flow rates of the two immiscible phases. By increasing either the continuous-fluid flow rate Qc or dispersed-fluid flow rate Qd, dripping to jetting transition (Figure 2.4) can occur. An extended liquid jet emits from the dispersed channel and ultimately breaks up into droplets at the end of the jet due to Rayleigh–

Plateau instability. More specifically, the transition occurs when the sum of viscous forces and dispersed phase inertial forces overcome interfacial tension[25], summarized by equation 4:

$$Ca_c + \mathrm{We}_d > 1 \quad (4)$$

Where We_d is the Weber number of the dispersed phase, defined as follow (Eq. 5):

$$We = \frac{\rho v L}{\gamma} \quad (5)$$

where ρ is the fluid density, v is the fluid velocity, L is the characteristic dimension of the channel e γ represents the interfacial tension between the two immiscible fluids.

Jetting regime can be divided in:

- narrowing jetting regime ($Ca_c > 1$), where the viscous-drag force overwhelms the capillary force, thus the jet stretches downstream with a thinner diameter.
- widening jetting regime ($We_d > 1$): the dispersed phase is faster than the continuous phase and consequently, the jet is decelerated as moving downstream, which widens the jets.

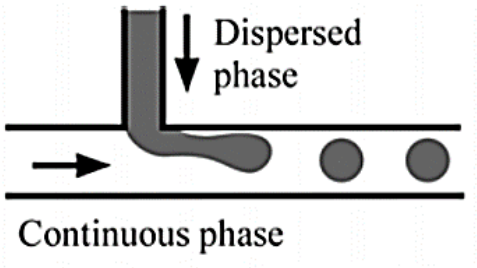

Figure 2.4: A schematic illustration of the jetting regime in a T-junction chip

However, the exact Ca_c values giving the transition between the three regimes, depends on the experimental conditions such as the dimension and geometry of the device and the physical properties of the fluids (viscosity, surface tension, etc.). In water-in-oil (W/O) droplet emulsions, the internal channel surfaces of droplet generation chip present a hydrophobic coating and the continuous phase typically consists of oils or organic solvents immiscible with water.

In this work a T-junction device was used to produce monodisperse Poly (ethylene glycol) microparticles using a PEG diacrylate (PEGDA) with a M_n=700 at different percentages and in presence of a photo-initiator. Moreover, the cleavable cross-linker N, N′(1,2Dihydroxyethylene) bis-acrylamide (DHEBA) is added to the pre-polymer solution at different concentrations to obtain porous networks. Firstly, the chip was characterized in terms of flow regimes and the influence of flow rates and capillary number on droplet size and rate has been analysed. According to the data fitting, scaling laws for the droplet diameter and frequency were calculated in the dripping regime and then applied to optimize the microfluidic parameters for the hydrogel microparticles synthesis.

2.2 Materials and methods

2.2.1 Pre-polymer solution and continuous phase preparation

Polyethylene glycol diacrylate (PEGDA700 by Sigma-Aldrich) solutions were prepared by adding 10% or 15% w/v pre-polymer to deionized water, via micro-pipette. After 5 min of agitation at room temperature, 0.5% v/v photo-initiator (Darocur 1173 by Sigma-Aldrich) and 4 different amounts of N, N′(1,2Dihydroxyethylene) bis-acrylamide (DHEBA) was added to the solution, as shown in Table 1. All steps were performed minimizing sample exposure to light, to avoid any pre-polymerization. The continuous phase, for all the pre-polymer solutions, is represented by Light Mineral Oil (LMO, Sigma Aldrich) with 5% (v/v) SPAN80 (Sigma Aldrich) as surfactant.

Table 2.1: Pre-polymer solutions composition, in terms of PEGDA700 and DHEBA, and samples name

PEGDA700 (w/v) %	DHEBA (w/v) %	R (mol PEG/mol Dheba)	X PEG	X DHEBA	NAME
15	0.1	42.9	0.98	0.02	15R40
15	1	4.29	0.81	0.19	15R4
10	0.07	40.8	0.98	0.02	10R40
10	0.7	4.08	0.81	0.19	10R4

2.2.2 Droplet generation

A T-junction glass chip (Dolomite, figure 2.5), connected with Polyethylene tubes (d=0.25 mm), was used to obtain droplets. PEGDA 700 g/mol 15% (w/v) and LMO with 5% (v/v) SPAN80 were the standard solutions chosen to characterize the emulsification process in the T-Junction device.

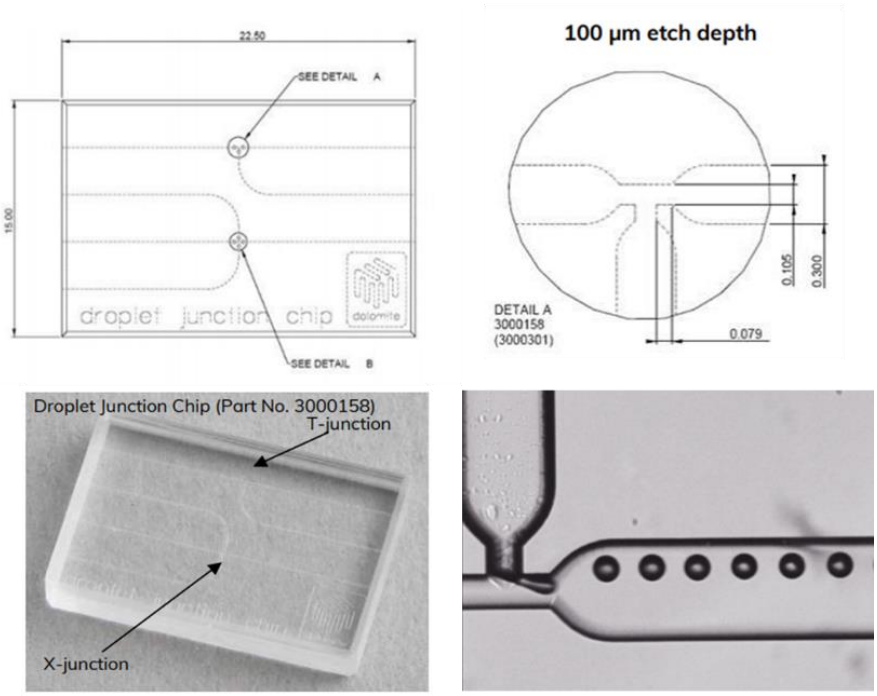

Figure 2.5: Images and technical specification of the quartz hydrophobic droplet chip used for the W/O emulsion. Bottom right, an image of monodisperse droplets of 75 µm produced with the T-Junction chip.

The production of droplets was performed starting from the microfluidic emulsification of pre-polymer solution in a continuous oil phase. The microfluidic setup is shown in figure 2.6. The continuous and disperse phases were injected using high precision syringe pumps (Nemesys-low pressure) to ensure a reproducible, stable flow. The continuous phase was introduced in the main channel and the dispersed phase in the lateral channel; they met at the T-junction where the droplet breakup occurred. The drops thus formed were conveyed into an outlet tube and light-cured by focusing a UV light (ʎ= 365 nm) on a tube's portion. The distance between the UV source and the outlet tube was set at 5cm.

After photo-polymerization, microparticles were collected in an Eppendorf and then washed. In particular, the synthesized particles collected in an LMO bath, were centrifuged at 7000 rpm for 1 minute, then LMO was extracted with a syringe, and acetone was added to the particles. The samples were kept in slow agitation for 20 minutes and then centrifuged again at 7000 rpm for 1 minute. Washing cycles, as described before, were also performed with diethyl ether, ethanol and H_2O with 0.05% Tween20 (v/v). The samples were finally suspended in H_2O with 0.05% Tween20 and stored at 4°C for a further characterization.

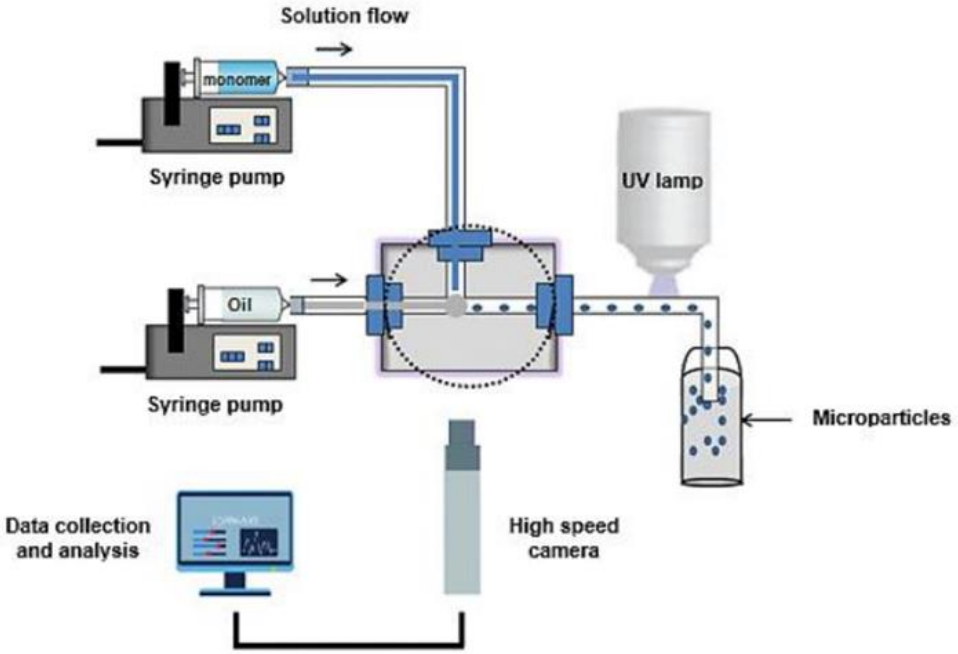

Figure 2.6: Schematic illustration of the experimental microfluidic setup. Two syringe pumps push the solutions into the microfluidic channels, up to the T-junction where the droplet breakup occurs. Then the droplets are polymerized on flow in the outlet tube by means of an UV lamp and collected in a reservoir. A high-speed camera collects videos of the droplet formation and send the data to the software for the size and rate analysis.

2.2.3 Data collection and analysis

Droplets formation process, visualized and recorded with a CCD camera Imperx IGV-B0620M, was then analysed with Dolomite Droplet Analysis software. Droplet size, frequency, spacing and velocity were measured at varying flow rates imposed. Flow data fitting was performed in MATLAB; droplet size and frequency scaling laws, with flow rate ratio of both phases and capillary number of the continuous phase, were found in dripping regime.

2.3 Results and discussion

2.3.1 Characterization of the droplet generation process

In order to find, for the system in question, the exact laws correlating size and frequencies of the droplets with capillary number and flow rate ratios, the experimental data extracted from the collected videos were analysed and fitted in MATLAB with the least squares method. Thus, droplet diameter *D* and frequency scaling laws (Eq. 6-7) were found and illustrated together with the experimental data (Figure 2.7).

$$\frac{D}{l} = 0.64(R)^{0.17}\ (Ca_c)^{-0.2} \qquad (6)$$

$$f = \frac{Q_d}{V} = Q_d\left(\frac{3}{4\pi}\right)\left(\frac{0.64(Q)^{0.17}\ (Ca_c)^{-0.2}}{2}L\right)^{-3} \qquad (7)$$

Where D is the droplet diameter, L is the thickness of the orifice (square section), R is the flow rates ratio, Ca_c is the capillary number of the continuous phase, and f is the droplet rate.

The obtained scaling low is consistent with the break-up hypothesis discussed in the introduction (Eq. 3) and with the literature[17,24]. Furthermore, the droplet rate scaling law indicates that, at fixed Ca_c and Q_c, when Q_d is reduced, despite particles volume decreases, also their frequency decreases. According to the obtained results, as expected, the diameter of the particles decreases as the capillary number of the continuous phase or the ratio between the flow rates increase and the productivity is enhanced with the increment in capillary number.

The physical explanation of these trends lies in the dripping break-up model: the tip of the discontinuous phase enters the main channel and then propagates, occupying a fraction of the cross section. Consequently, the thread of the dispersed phase is forced to collapse (squeezing pressure effect) under the pressure exerted by the syringe pump. Also, the inertial effect of the oil tends to thin the neck of the dispersed phase (inertial effect) and the droplet is formed.

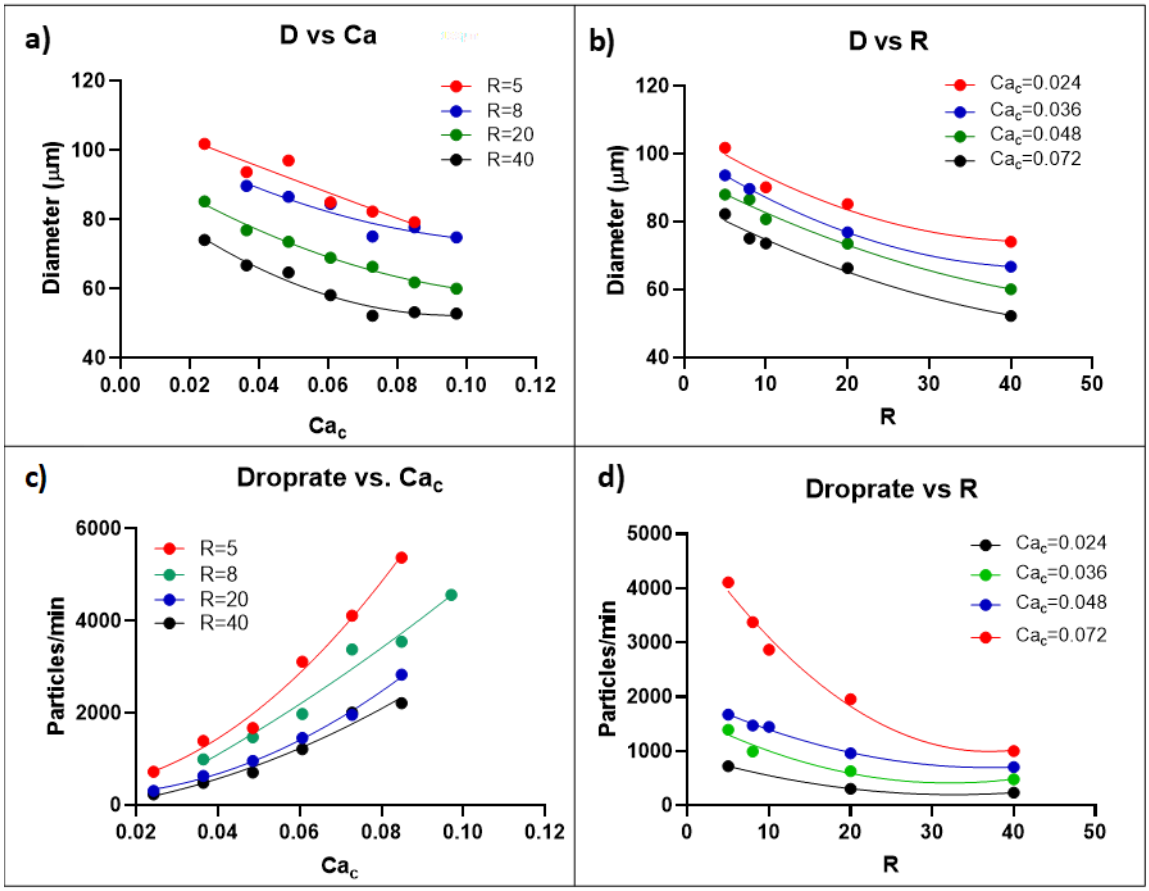

Figure 2.7: Effect of capillary number Ca_c and flow rates ratio R on droplet size and rate. (a) Data showing the variation of droplet diameter in function of Ca_c, at fixed R. (b) Data showing the variation of droplet diameter in function of R at fixed Ca_c. (c) Data showing the variation of drop rate in function of Ca_c at fixed R (d) Data showing the variation of drop rate in function of R at fixed Ca_c.

In this scenario, the forces that favour the droplet formation are the shear stress exerted by the continuous phase at the interface, the squeezing pressure and the inertial effect of the continuous phase. The forces that oppose the droplet formation are the internal cohesion of the discontinuous phase, function of its viscosity, and the surface tension. Note that if the shear stress is too high, the dispersed phase thread is stretched, and jetting or co-flow can occur.
According to this break-up model, and the obtained scaling laws, it is possible to discuss the influence of each parameter on droplet size and rate:

- If Ca_c and the R increase, droplet size decreases. Moreover, while the drop rate increases with Ca_c, the increase of the ratio R could either reduce or increase the droplet rate depending on the variation of the single-phase flow rate.

- If the viscosities ratio μ_c/μ_d is lowered, the resulting droplets will be bigger while droplet rate will decrease. Tice, Lyon and Ismagilov[32] also demonstrated that for higher viscosities of the discontinuous phase, the system crosses over to jetting regime at lower flow rates, or alternatively, at smaller Ca. If the viscosities ratio μ_c/μ_d increases, droplet size reduces while the productivity is enhanced. Furthermore, it is reasonable to assume that the dripping-jetting transition limit moves towards higher capillary number.

However, the combined effect of γ, μ_c and Q_c, is contained in Ca_c, and can be discussed in these terms: increasing μ_c, at other parameters fixed, generates an increment in capillary number and productivity, while droplet diameter becomes smaller. Both effects can be obtained and amplified by improving Q_c or lowering γ. A productivity enhancement can be selectively obtained by increasing Q_d, without affecting the oil capillary number.

2.3.2 Optimization of microfluidic parameters for the hydrogel microparticles synthesis

According to the T-junction characterization, to obtain 75µm monodisperse droplets three different flow rates (Table 2.2) have been compared in terms of droplet size, stability, droplet rate and spacing to avoid coalescence phenomena. Since the dispersed phases for all the synthesized hydrogel microparticles are very similar in terms of viscosity, density and interfacial tension with the continuous phase, the optimal flow rates will be the same for all the productions (Table 2.1). The continuous phase used for all experiments is LMO with 5% SPAN80 as surfactant and an interfacial tension with the dispersed phases ranging from 1.8 to 3 mN/m. Analysing the data showed in the table 2.2, it is evident that the middle flow rates are the most productive ones but, when the Q_c is elevated, the regime results in a not so stable dripping, causing an increased standard deviation and a not monodisperse production of final particles. The last flow rates, instead, produce monodisperse solution of particles but it is needed a longer time to synthesize a significant quantity of particles. The optimal flow rates are 0.25 µL/min for the dispersed phase and 2.5 µL/min for the oil. This setting can produce about 20 particles per second, with a size ranging from 72.6 to 77.4µm.

Table 2.2: Flow rates and their ratio are imposed parameters; Ca is calculated knowing the continuous phase properties and flow rate; mean droplet size and its standard deviation, frequency and spacing between two consequent droplets are obtained from the droplet generation videos analysis (Droplet Monitor software).

R	Q_d(µL/min)	Q_c(µL/min)	Size(µm)	S.Dev.(µm)	f (drops/s)	Spacing(µm)	Ca
10	0.25	2.5	75	2.4	19.9	110.2	3.03E-02
10	0.5	5	70.3	6.5	38.6	101.2	6.07E-02
20	0.1	2.0	73.2	1.17	9.7	157.8	2.43E-02

To demonstrate the droplet uniformity, a video of the production of about 1000 droplets was acquired and analysed with Droplet monitor software to evaluate the droplets diameter. The histogram in figure 2.8 shows the frequency distribution of the droplets diameter. It can be noticed how about 90% of the droplets falls into the range between 75 and 77µm.

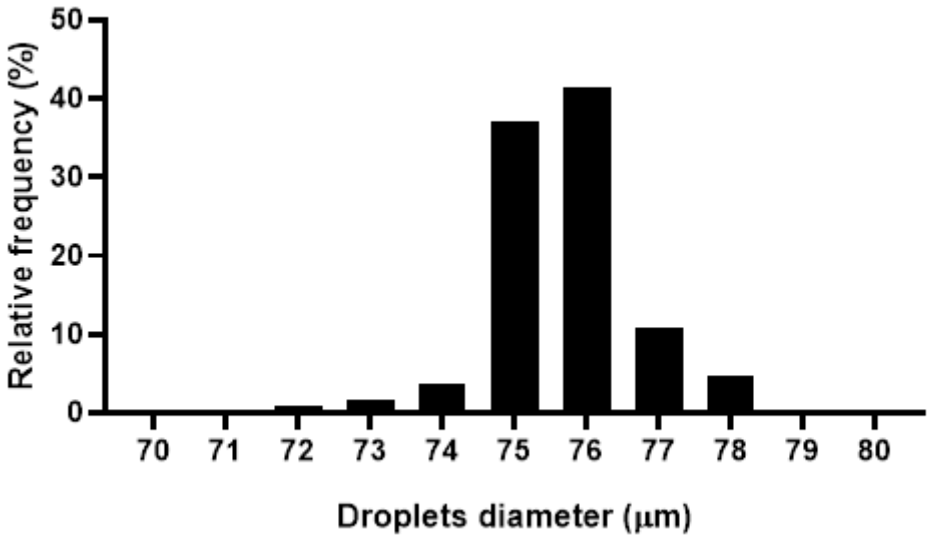

Figure 2.8: Frequency distribution of droplets diameter evaluated from the video analysis of about 1000 droplets production (10R40).

Knowing the flow rates, it is possible to estimate the permanence time of a particle in the portion of the outlet tube illuminated by the UV lamp. The internal radius of the outlet tube *r* measure 0.38 mm, the average length of the illuminated portion *L* is 3.8 cm and the total flow rate Q (PEGDA + oil) is 3µL/min, so according to equation 8 the permanence time is about 6 min.

$$t = \frac{V}{Q} = \frac{\pi r^2 L}{Q} \qquad (8)$$

In consequence, the pre-polymer solution droplets are polymerized in 6 minutes with a lamp power density of 1.8 W/cm^2 and a resulting energy flux of about 250 J/cm^2, which is enough to fully crosslink the polymer. It is important to notice that the use of a photo initiator for the polymerization process could hinder PEGDA biocompatibility but, for immuno-sensing applications where there is no contact with living cells, this does not represent a limitation. For this reason, studies about the biocompatibility of PEGDA and photo initiator mixture have not been performed in this work. After the polymerization, microparticles have been washed to eliminate the excess of oil and imaged with an optical microscope (figure 2.9), to demonstrate their monodispersity.

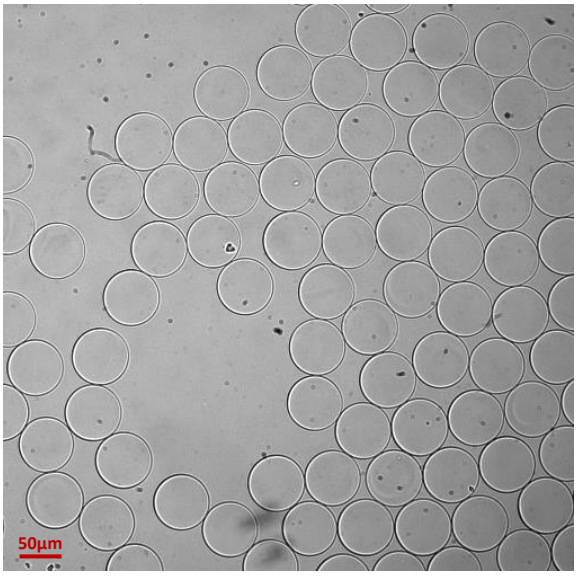

Figure 2.9: Optical image of monodisperse microparticles of PEGDA/DHEBA copolymer (10R40)

2.4 Conclusions

In this work, microfluidic droplets generation in a T-junction device has been investigated and used in order to synthesize cleavable hydrogel microparticles with fine controlled physical and chemical properties, such as size, shape and composition to perform in-gel immuno-assays.

First, the dynamics of droplet formation was analysed, studying the effect of different parameters (Capillary number, flow rates ratio, viscosities of both phases etc.) on the hydrogel microparticles synthesis in terms of size and productivity. These studies led to scaling laws which allow to predict, the droplets size and productivity at fixed flow rates and phases composition. These scaling laws were used to produce monodisperse droplets of PEGDA/DHEBA copolymers with a diameter of 75µm, which were then polymerized on flow to realize hydrogels microparticles. To sum up, this work allowed us to set a microfluidic platform and optimize microfluidic parameters in order to perform a high throughput synthesis of monodisperse hydrogel microparticles for diagnostics.

2.5 References

1. Kim, J. H. *et al.* Droplet Microfluidics for Producing Functional Microparticles. *Langmuir* **30**, 1473–1488 (2014).
2. Kan Liu, †, Hui-Jiang Ding, †, Jing Liu, †, Yong Chen, ‡ and & Xing-Zhong Zhao*, †,§. Shape-Controlled Production of Biodegradable Calcium Alginate Gel Microparticles Using a Novel Microfluidic Device. (2006) doi:10.1021/LA061729+.
3. Dendukuri, D., Tsoi, K., Hatton, T. A. & Doyle, P. S. Controlled synthesis of nonspherical microparticles using microfluidics. *Langmuir* **21**, 2113–2116 (2005).
4. Xu, Q. *et al.* Preparation of Monodisperse Biodegradable Polymer Microparticles Using a Microfluidic Flow-Focusing Device for Controlled Drug Delivery. *Small* **5**, 1575–1581 (2009).
5. Wan, J., Bick, A., Sullivan, M. & Stone, H. A. Controllable Microfluidic Production of Microbubbles in Water-in-Oil Emulsions and the Formation of Porous Microparticles. *Adv. Mater.* **20**, 3314–3318 (2008).
6. Duncanson, W. J. *et al.* Microfluidic synthesis of advanced microparticles for encapsulation and controlled release. *Lab on a Chip* vol. 12 2135–2145 (2012).
7. Rondeau, E. & Cooper-White, J. J. Biopolymer Microparticle and Nanoparticle Formation within a Microfluidic Device. *Langmuir* **24**, 6937–6945 (2008).
8. Wang, W., Zhang, M.-J. & Chu, L.-Y. Functional Polymeric Microparticles Engineered from Controllable Microfluidic Emulsions. *Acc. Chem. Res.* **47**, 373–384 (2014).
9. Han, S. I., Soo Kim, H. & Han, A. In-droplet cell concentration using dielectrophoresis. *Biosens. Bioelectron.* **97**, 41–45 (2017).

10. Kim, H. S., Guzman, A. R., Thapa, H. R., Devarenne, T. P. & Han, A. A droplet microfluidics platform for rapid microalgal growth and oil production analysis. *Biotechnol. Bioeng.* **113**, 1691–1701 (2016).
11. Thorsen, T., Roberts, R. W., Arnold, F. H. & Quake, S. R. Dynamic pattern formation in a vesicle-generating microfluidic device. *Phys. Rev. Lett.* **86**, 4163–4166 (2001).
12. Kumacheva, E. & Garstecki, P. Microfluidic reactors for polymer particles. (2011).
13. Garstecki, P., Gañán-Calvo, A. M. & Whitesides, G. M. *Formation of bubbles and droplets in microfluidic systems*.
14. Garstecki, P., Fuerstman, M. J., Stone, H. A. & Whitesides, G. M. Formation of droplets and bubbles in a microfluidic T-junction - Scaling and mechanism of break-up. *Lab Chip* **6**, 437–446 (2006).
15. Zhao, C. X. & Middelberg, A. P. J. Two-phase microfluidic flows. *Chem. Eng. Sci.* **66**, 1394–1411 (2011).
16. Nisisako, T., Torii, T. & Higuchi, T. Novel microreactors for functional polymer beads. *Chem. Eng. J.* **101**, 23–29 (2004).
17. De menech, M., Garstecki, P., Jousse, F. & Stone, H. A. Transition from squeezing to dripping in a microfluidic T-shaped junction. *J. Fluid Mech.* **595**, 141–161 (2008).
18. Bai, L., Fu, Y., Zhao, S. & Cheng, Y. Droplet formation in a microfluidic T-junction involving highly viscous fluid systems. *Chem. Eng. Sci.* **145**, 141–148 (2016).
19. Chiarello, E., Gupta, A., Mistura, G., Sbragaglia, M. & Pierno, M. Droplet breakup driven by shear thinning solutions in a microfluidic T-junction. *Phys. Rev. Fluids* **2**, (2017).
20. Roumpea, E., Chinaud, M. & Angeli, P. Experimental investigations of non-Newtonian/Newtonian liquid-liquid flows in microchannels. *AIChE J.* **63**, 3599–3609 (2017).
21. Wang, J. T., Wang, J. & Han, J. J. Fabrication of advanced particles and particle-based materials assisted by droplet-based microfluidics. *Small* **7**, 1728–1754 (2011).
22. Liu, H. & Zhang, Y. Droplet formation in a T-shaped microfluidic junction. *J. Appl. Phys.* **106**, (2009).
23. Zhu, P. & Wang, L. Passive and active droplet generation with microfluidics: a review. *Lab Chip* **17**, 34–75 (2017).
24. De Menech, M. Modeling of droplet breakup in a microfluidic T-shaped junction with a phase-field model. *Phys. Rev. E - Stat. Nonlinear, Soft Matter Phys.* **73**, 1–19 (2006).

25. Nunes, J. K., Tsai, S. S. H., Wan, J. & Stone, H. A. Dripping and jetting in microfluidic multiphase flows applied to particle and fibre synthesis. *J. Phys. D. Appl. Phys.* **46**, (2013).
26. Xu, J. H., Li, S. W., Tan, J., Wang, Y. J. & Luo, G. S. Preparation of highly monodisperse droplet in a T-junction microfluidic device. *AIChE J.* **52**, 3005–3010 (2006).
27. Yeh, C. H., Zhao, Q., Lee, S. J. & Lin, Y. C. Using a T-junction microfluidic chip for monodisperse calcium alginate microparticles and encapsulation of nanoparticles. *Sensors Actuators, A Phys.* **151**, 231–236 (2009).
28. Akbari, S. & Pirbodaghi, T. Microfluidic encapsulation of cells in alginate particles via an improved internal gelation approach. *Microfluid. Nanofluidics* **16**, 773–777 (2014).
29. Tan, W.-H. & Takeuchi, S. Monodisperse Alginate Hydrogel Microbeads for Cell Encapsulation. *Adv. Mater.* **19**, 2696–2701 (2007).
30. Celetti, G., Di Natale, C., Causa, F., Battista, E. & Netti, P. A. Functionalized poly(ethylene glycol) diacrylate microgels by microfluidics: In situ peptide encapsulation for in serum selective protein detection. *Colloids Surfaces B Biointerfaces* **145**, 21–29 (2016).
31. Shembekar, N., Chaipan, C., Utharala, R. & Merten, C. A. Droplet-based microfluidics in drug discovery, transcriptomics and high-throughput molecular genetics. *Lab on a Chip* vol. 16 1314–1331 (2016).
32. Tice, J. D., Lyon, A. D. & Ismagilov, R. F. Effects of viscosity on droplet formation and mixing in microfluidic channels. *Anal. Chim. Acta* **507**, 73–77 (2004).

3. Physico-Chemical Characterization of Peg-Based Hydrogel Microparticles

3.1 Introduction

PEG-based Hydrogel microparticles have been widely used as a versatile platform for biological assays due to their biocompatibility, hydrophilic and highly tuneable properties[1–4]. Their solution-like environment and non-fouling features in complex biological fluids render hydrogels as ideal immobilization substrates for immunoassays in biosensing applications [5–8]. When compared to flat surfaces, 3D particles offer significantly higher surface areas for immobilization of capture probes[9], with an increase in protein loading capacity, and sensitivities, and lowering limits of detection[10]. Some of the drawbacks and limitations of these hydrogels are related to laborious functionalization of antibodies to the gel, and to the hindered mass transport and analytes diffusion within this cross-linked polymer network, thus requiring longer incubation time and reducing sensitivity.

Introduction of pores creates more space for high protein complexes, increases surface area–to–volume ratios for antibody immobilization, and facilitates biomolecules diffusion[11]. A number of approaches have been used to generate porous scaffolds. One of the simplest methods for generation of porous hydrogels is through freeze drying and a consequent re-swelling. The drawback of this method is that pore formation affects the mechanical properties of the hydrogels, with limited applications[12,13]. Another simple strategy is to modulate the composition of poly (ethylene glycol)diacrylate (PEGDA) in the pre-polymer solution. Increasing the molecular weight of the PEGDA chains and lowering its concentration are effective ways to increase the gel porosity. Indeed, longer PEGDA chains or lower concentrations of active species result in a reduced crosslinking density. Gas-forming techniques have been also used to generate PEG hydrogels with high pore sizes, but with this technique it is difficult to control their sizes and guarantee pore interconnectivity[14]. One major system is solvent casting, where various particle classes are homogeneously distributed into a solution prior to polymerization. A wide variety of inactive porogens have been employed depending on the hydrogel and application, typically inert PEG[15,16]. Once polymerization is completed, the porogens are subsequently leached or dissolved away with a selective solvent, resulting in a porous network[17]. Although porous hydrogels can be generated with these

methods, the use of a porogen requires many washing steps and many hours (up to 48 hours) to eliminate the excess[18].

In this work we focus on development of a simple technique for one-step generation of porous and reactive PEG hydrogels. To this purpose, we have developed a new class of porous hydrogel particles through the use of a specific cleavable cross-linker, such as N,N′(1,2Dihydroxyethylene)bisacrylamide (DHEBA). DHEBA has been largely used in literature to produce hollow particles[19], membranes for separation, synthesis and catalysis[20] or selectively permeable particles[21], but it has never been used to produce pores without completely destroying the network.

Hydrogel microparticles realized in this project are designed to optimize the porosity of PEG-based materials, basing on previous studies (not published yet) conducted by our research group about PEGDA700 microgels. For this purpose, the microparticles are a result of photo-polymerization of UV-crosslinked PEGDA (Mn = 700) with DHEBA at different ratios and in the presence of Darocur1173 as photoinitiator. These cleavable microparticles are synthesized by droplet microfluidic chip. After photo-polymerization, the vicinal diols in the cross-linker can be cleaved by stoichiometric amounts of sodium periodate [22]. Upon chemical cleavage, the crosslinking density reduces, the pore size increases, and, simultaneously, two aldehyde groups are formed useful for further functionalization (Figure 3.1). Schiff base formation between aldehydes and amine-containing molecule (i.e. antibody) occurs readily in aqueous solutions, especially at elevated pH, and this bond is stabilized by adding a reductant compound (i.e. sodium cyanoborohydride).

Equilibrium volumetric swelling, increment in swollen radius and the amount of aldehydes formed have been analysed to optimize cleavage reaction conditions. Moreover, to gain information about the accessibility of the biomolecules inside the polymeric network, studies about relative porosity for all the microparticles composition have been carried out using NMR cryoporometry and equilibrium partitioning of fluorescent probes. Finally, fluorescence correlation spectroscopy has been used to study the influence of the polymeric network on the diffusion of fluorescently labelled biomolecules with a high molecular weight, like antibodies (Human IgG).

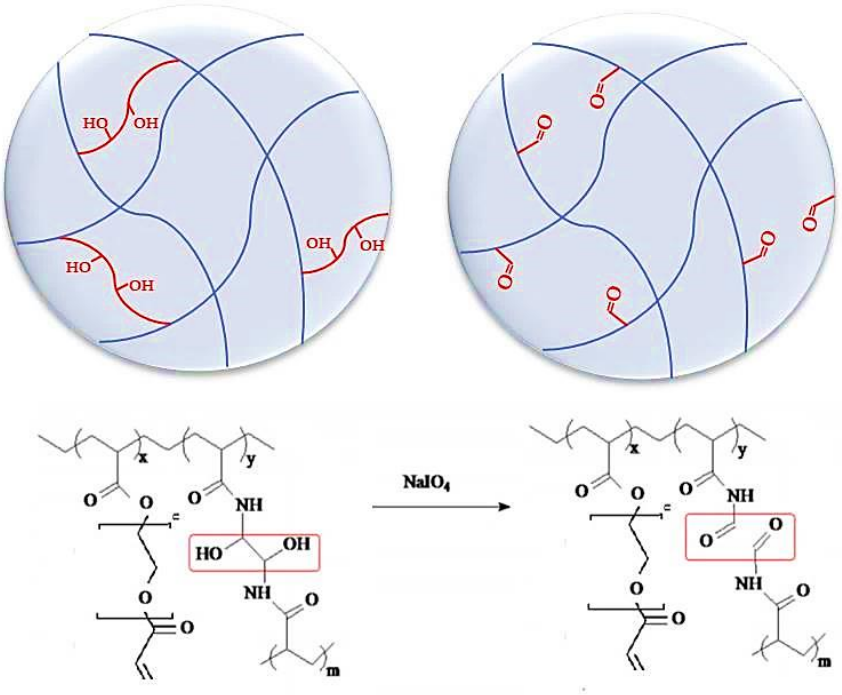

Figure 3.1: Scheme of the hydrogel microparticles chemical composition and cleavage reaction

3.2 Materials and Methods

3.2.1 Hydrogel microparticles synthesis

Polyethylene glycol diacrylate (PEGDA700 by Sigma-Aldrich) solutions were prepared, as shown in Table 2.1, with 4 different amounts of DHEBA. The prepolymer solution was vortexed for 1 min at room temperature, adding 0.5% v/v of Darocur1173 (Sigma-Aldrich) as photo initiator. All preliminary steps were performed minimizing sample exposure to light, to avoid any undesired polymerization. The droplets generation was performed starting from the microfluidic emulsification of pre-polymer solution in a continuous phase (oil).

A T-junction glass chip (Dolomite) was used to obtain 70µm diameter droplets, using Light Mineral Oil (LMO) with 5% (v/v) SPAN 20 as continuous phase. Polyethylene tubes (d=0.25 mm) were used to deliver fluids to the microdevice. The continuous and disperse phases were injected using high precision syringe pumps (Nemesys-low pressure) to ensure a reproducible, stable flow. The continuous phase was introduced in the main channel and the dispersed phase in the lateral channel; they met at the T-junction where the droplet breakup occurred.

Table 3.1: Prepolymer solutions composition, in terms of PEGDA700 and DHEBA, and samples identification code.

PEGDA700 (w/v) %	DHEBA (w/v) %	R (mol PEG/mol Dheba)	X PEG	X DHEBA	NAME
15	0.1	42.9	0.98	0.02	15R40
15	1	4.29	0.81	0.19	15R4
10	0.07	40.8	0.98	0.02	10R40
10	0.7	4.08	0.81	0.19	10R4

The drops were polymerized on flow by means of a UV lamp. After photo-polymerization, hydrogels microparticles were collected and washed. All the experiments were carried out at room temperature and atmospheric pressure.

3.2.2 Morphological characterization

Morphological characterization was carried out collecting images of the hydrogel microparticles in the dried state by SEM (scanning electron microscope) and swollen state by optical microscope (IX 71 Olympus, DRY 10× objective). SEM analysis were performed on a FE-SEM Ultra Plus (Zeiss) microscope at 5 kV. For sample preparation, 50µL of microparticles suspension was spotted on a thin glass slide, air-dried for 16 hours at room temperature and then sputtered with a 10 nm thin gold layer. After these steps, images of the dried microparticles were acquired.

3.2.3 Equilibrium volumetric swelling measurements

Equilibrium swelling experiments were performed to investigate the influence of Sodium periodate concentration on the cleavage reaction. Equilibrium swelling ratio Q is defined as Equation 1.

$$Q = \frac{(Vs - Vd)}{Vd} \qquad (1)$$

Where V_s is the volume of the water-swollen microparticles at room temperature and V_d is the volume of the dried microparticles, assuming the particles remain spherical during the drying

process. PEGDA700 15% with 1% (w/v) of DHEBA was used as model and three sodium periodate concentrations (0.1mM, 1mM, 10mM) were investigated. The microparticles were cleaved overnight at room temperature and then washed to stop the reaction. The experiments were performed recording hydrogel microparticles images in the swollen state and in the dry state with an inverted microscope (IX 71 Olympus) equipped with a 10× objective. Cleaved hydrogel microparticles were soaked at room temperature in H_2O with 0.05% tween (v/v) for 24h and then the images recorded. The average radius of the swollen particles was estimated using ImageJ software. The same samples were then dried in an oven at 40 °C under vacuum for 24h, and their average radius, in the dry state, was measured.

3.2.4 Oxidative cleavage kinetics

In order to optimize cleavage conditions, several studies about kinetics and temperature were carried out, following the variation of particles size and number of aldehydes over time. Regarding the particle radius, images of swollen particles were acquired and analysed using an inverted microscope (IX 71 Olympus) equipped with a 10x objective and the ImageJ software. The reaction was carried out at two different temperatures (25°C and 50°C) and followed over time up to 24 hours for the higher temperature reaction and up to 48 hours for the room temperature reaction. For every time step, a small amount of particles was collected, washed with a solution of Sodium Bicarbonate 0.1M and then visualized at the microscope.

3.2.5 Aldehydes titration

In order to follow the generation of aldehydes inside the particles during the reaction, a commercial colorimetric aldehyde assay kit (Sigma Aldrich) was used. Hydrogel microparticles were cleaved with a 10mM Sodium Periodate solution at 50°C and kept in agitation at 500 rpm, avoiding any exposition to light that could slow the reaction. For every time step, about 1000 particles were collected, washed with a solution of Sodium Bicarbonate 0.1M to stop the reaction and then analysed with the colorimetric kit, including also a sample containing non-cleaved particles (time zero) and a standard curve prepared with known concentrations of aldehydes (0, 1, 3.3, 10, 33, 100, 333, and 1000 mM). The assay was performed in a 96 wells plate, following the manufacturer instructions. The 550nm absorbance of all samples was registered, using a plate reader (2300 EnSpire multilabel reader, Perkin-Elmer) and the number of aldehydes was calculated through the calibration curve. All experiments were carried out in triplicate and the error was represented by the standard deviation.

3.2.6 Equilibrium partitioning measurements

Using a Nikon Eclipse C1/80i confocal microscope, equilibrium partitioning of both FITC-labelled IgG antibodies and Silica nanoparticles (size 50 nm) was measured. Fluorescence signal inside and outside the particles was read and the IN/OUT average fluorescence signal ratio was calculated.

The experiments were performed by dropping 27 μL of the particles suspension (corresponding to about 100 particles) in a "IBIDI μ-Slide 18 Well – Flat" and then adding 3 μL of 20 μM IgG-FITC solution or Silica nanoparticles suspension in another well (thus obtaining a final concentration of 2 μM for each well). The IBIDI slide was treated with Bovine serum albumin (BSA, Sigma Aldrich) 1% to avoid aspecific adsorption of antibodies on the glass slide. After 60 minutes all images were acquired at the confocal microscope (CLSM Leica TCS SP5, using argon laser line 488 nm, objective 25x water, scan speed 400 Hz, λ em range 500-550 nm). Regarding the experiments on cleaved particles, all aldehydes have been previously blocked via reductive amination to avoid any interaction between antibodies and hydrogel microparticles during the diffusion. In particular, the cleaved particles were capped with Tris buffer 0.1M(under stirring for 30 min at room temperature) and then washed.

3.2.7 NMR cryoporometry measurements

NMR cryo-porometry is a technique for the determination of the pore size distribution via the observation of the solid-liquid phase transition temperature of a medium (water) confined in the pores. Water trapped in small pores melts at lower temperature and the bigger the pore the most water trapped behaves as free water, liquefying near the 0°C.

Jackson and McKenna [23] expressed the shift of the pore melting point T_m as:

$$\Delta T_m = T_m - T_0 = -\frac{k}{r} \qquad (2)$$

where k is a material constant that depends on the molar volume v, on the solid–liquid surface energy Υ_{sl}, on the enthalpy ΔH and on the bulk melting point T_0, as equation 3 indicates.

$$k_c = 2v\gamma_{sl}\frac{T_0}{\Delta H_f} \qquad (3)$$

The resulting NMR signal I(T) varies smoothly with temperature T and its shape reflects the pore size distribution. By assuming I(T) ~ V(T) where V(T) is the pore volume that contains molten liquid at a given temperature T, it can be simply obtained a pore-size distribution p(r) as follows:

$$\mathrm{p(r)} = \frac{k}{r^2}\frac{dI(T)}{dT} \qquad (4)$$

Basing on this concept, the higher the NMR signal and its derivative the more porous results the material.

NMR spectra were recorded using an Agilent 600MHz (14 Tesla) spectrometer equipped with a DD2 console and an OneNMR HX probe. The NMR cryoporometry measurements were performed to study the influence of PEGDA/DHEBA ratio on the pore size distribution of pre- and post-cleavage copolymers. The following hydrogel bulk samples with 10% (v/v) D_2O were prepared:

- PEGDA 10% with 0.5% (v/v) Darocur and 1:4 mol DHEBA
- PEGDA 10% with 0.5% (v/v) Darocur and 1:40 mol DHEBA
- PEGDA 15% with 0.5% (v/v) Darocur and 1:4 mol DHEBA
- PEGDA 15% with 0.5% (v/v) Darocur and 1:40 mol DHEBA

The obtained solutions were degassed with nitrogen, and then transferred into NMR glass tubes (5 mm of diameter) reaching a height of 5 cm. The NMR tubes were fixed to a support and the pre-polymer solutions were then polymerized using a UV lamp for 30 minutes with a 365nm light. Regarding the post-cleavage samples, the hydrogels were dried in oven (overnight, 60°C) and then a 10mM solution of Sodium Periodate was added in order to completely cover the samples. The cleavage reaction took place overnight at 50°C. After that, NMR cryo-porometry measurements were performed on fast frozen samples, using a temperature ramp going from -45°C to 5°C with a velocity of 0.1°C per minute. Signal was acquired every 50 minutes (every 5°C).

3.2.8 Fluorescence correlation spectroscopy measurements

In order to estimate the diffusion coefficient of antibodies inside the hydrogel microparticles, fluorescence correlation spectroscopy (FCS) experiments were carried out. Microparticles were cleaved (overnight, 50°C, 500 rpm) and washed with a 0.1M Sodium bicarbonate solution to stop the reaction. The cleaved microparticles were incubated (20 min, RT) with 10nM atto647N and 10nM atto647N-labelled human IgG and, then, analysed with a confocal microscope (Zeiss, using a 633 laser (2%) in total reflection mode, objective 40x water). The experiments were performed in an "IBIDI μ-Slide 8 Wells", pre-treated with a BSA solution to avoid any interaction between the glass slide and the fluorescent probes during the acquisitions. For fluorescence excitation a low-noise laser was used (633 nm wavelength). Determination of the confocal volume was established via calibration against a 10nM phosphate buffered saline (PBS) solution of atto647N, assuming D_0 = 160 $\mu m^2/s$ [24]. All FCS measurements were performed at room temperature and, for each sample, 10 FCS correlation functions were acquired for 10s in three different particles.

3.3 Results and discussion

3.3.1 Hydrogel microparticles synthesis and morphological characterization

According to the T-junction characterization (present in the chapter 2), microgel droplet size and generation rate were regulated by different parameters. In chapter 2, we applied different outer to inner flow rate ratio to test sizes and generation rates during droplet generation process. The aqueous phases used are shown in Table 3.1. The continuous phase used for all experiments is LMO with 5% SPAN80 as surfactant and an interfacial tension with the dispersed phases ranging from 1.8 to 3mN/m. A 75μm diameter monodisperse droplets would be generated using a flow rate of 0.25μL/min for the dispersed phase and 2.5μL/min for the oil, with an outer to inner flow rate of 10, resulting in a production of ~20 droplets per second. Since the dispersed phases for all the synthesized hydrogel microparticles are very similar in terms of viscosity, density and interfacial tension with the continuous phase, the optimal flow rates will be the same for all the productions. The pre-polymer solution droplets are polymerized in 6 minutes with a lamp power density of 1.8 W/cm^2 and a resulting exergy flux of about 250 J/cm^2, which is enough to fully crosslink the polymer.

To demonstrate the droplet uniformity, a video of the production of about 1000 droplets was acquired and analysed with Droplet monitor software to evaluate the droplets diameter. The histogram in figure 3.2 shows the frequency distribution of the droplets diameter. It can be noticed how about 90% of the droplets falls into the range between 75 and 77µm. The polymerized hydrogel microparticles are shown, in the swollen and dried state in figure 3.3. Optical images confirm that the microparticles, after the photopolymerization, are monodisperse with a diameter of about 75µm, without any contraction. SEM images demonstrate that the microparticles retain their spherical shape even in the dried state, with a diameter of about 30µm.

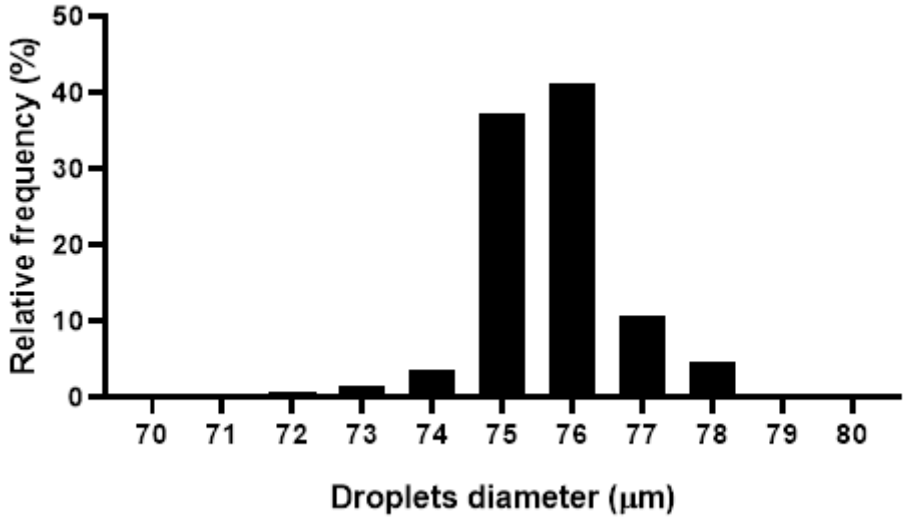

Figure 3.2: Frequency distribution of droplets diameter evaluated from the video analysis of about 1000 droplets production (10R40).

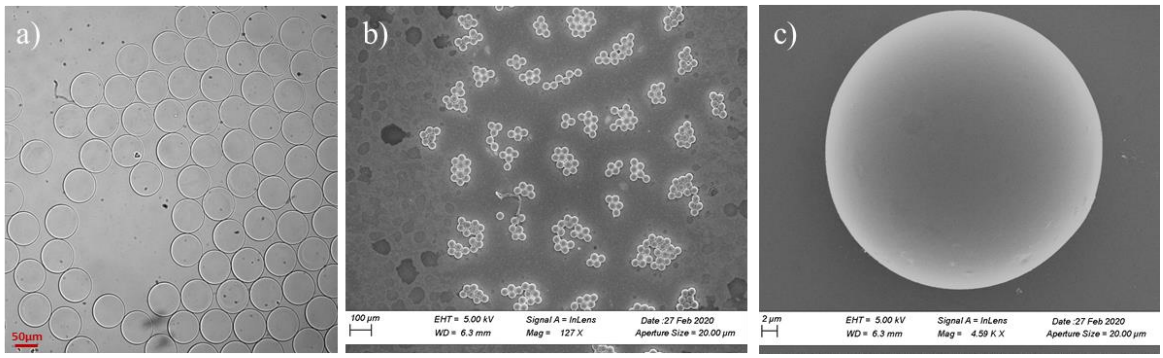

Figure 3.3: a) Optical image of monodisperse swollen microparticles of PEGDA/DHEBA copolymer (10R40) b) SEM image of dried 10R40 microparticles (127 X) c) SEM image of dried 10R40 microparticle's surface (4.59 K X)

3.3.2 Equilibrium volumetric swelling measurements

Equilibrium swelling studies were performed as an examination of volume differences between microparticles, after the cleavage reaction of the cross-linker DHEBA. Equilibrium volumetric swelling of the hydrogel microparticles is directly proportional to their porosity.

The higher the swelling the greater the amount of water absorbed by the hydrogel, suggesting a greater effectiveness of the cleavage reaction. Different concentrations of the cutting agent, the sodium periodate, have been evaluated. As shown in figure 3.4, the sodium periodate at 10mM leads to a greater volumetric difference between the particle in its wet/dry state. Consequently, this concentration was used for further characterizations and analysis.

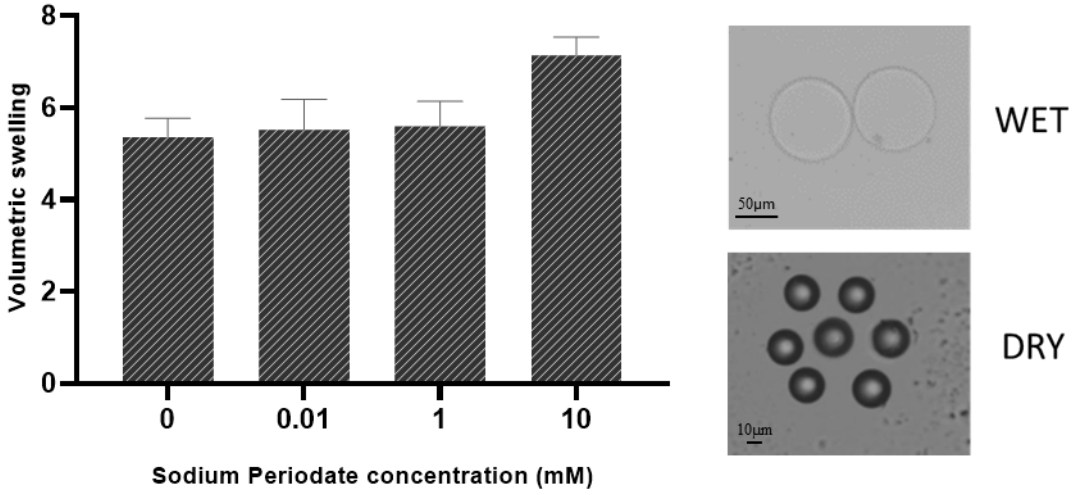

Figure 3.4: Volumetric swelling of hydrogel microparticles 15R4 at different cleavage conditions in terms of sodium periodate concentrations (left) and example of optical microscope images of swollen and dry hydrogel microparticles (right).

3.3.3 Cleavage kinetics analysis

In order to optimize cleavage temperature and time with sodium periodate (10mM), studies about the influence of these two parameters on the swollen particles size were conducted for all the hydrogel microparticles compositions. The figure 3.5 shows the variation of particles size over cleavage time at room temperature. In these conditions, the reaction is particularly slow, in fact there is no significant increment in the particles radius up to 48 hours. As shown in figure 3.6, the cleavage reaction conducted at 50°C is faster and the experimental data show a significant increment in the particles radius in 24 hours. After 1 day, the microparticles start to

lose their spherical shape due to the network degradation. The optimal cleavage conditions emerging from this analysis result to be 50°C overnight. Moreover, it can be noticed how the cleaved sample presenting the highest increment in radius (from 34 to 42 μm) is the 10R40 microparticle (figure 3.6d), resulting the most promising material for the in-gel immunoassay application.

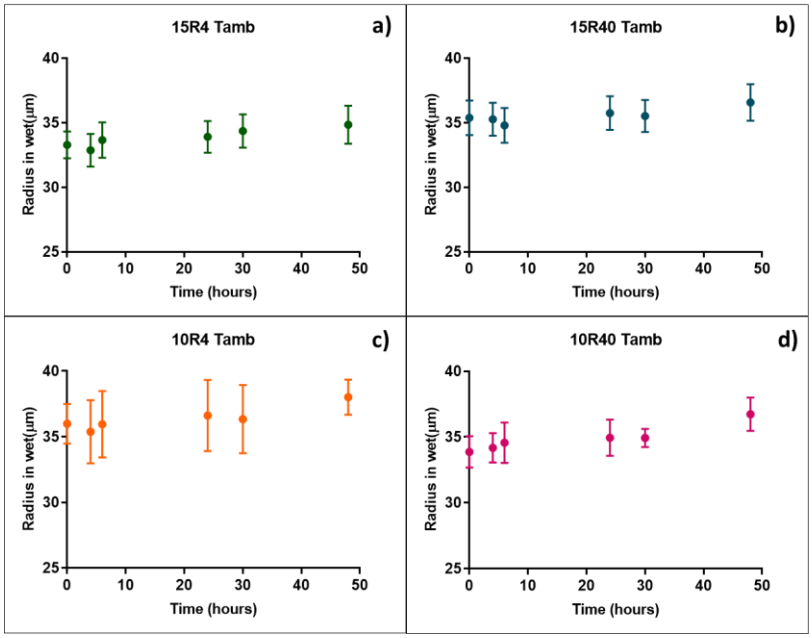

Figure 3.5: Increment in swollen particles radius over cleavage time at room temperature for the samples a)15R4, b)15R40, c)10R4 and d)10R40

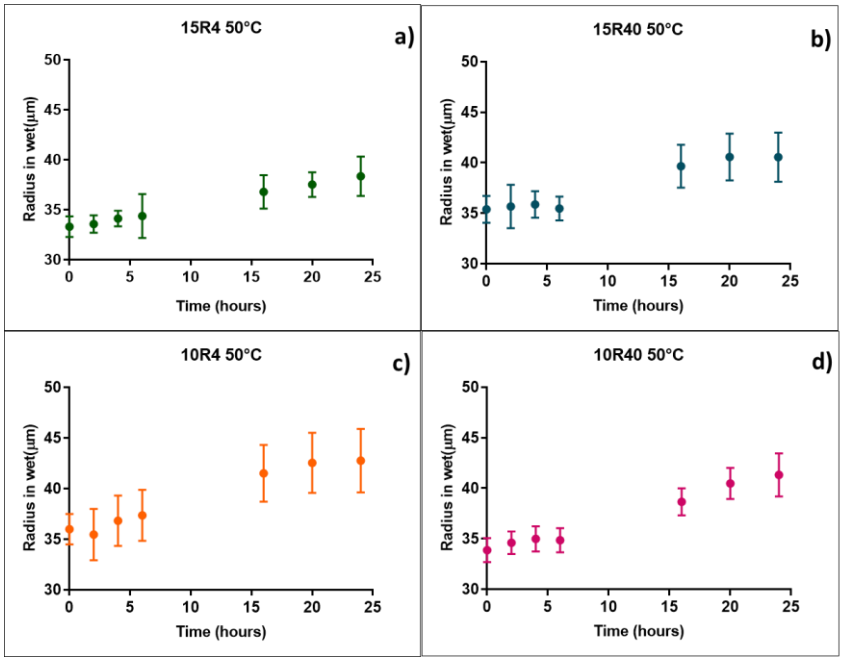

Figure 3.6: Increment in swollen particles radius over cleavage time at 50°C for the samples a)15R4, b)15R40, c)10R4 and d)10R40

3.3.4 NMR cryo-porometry measurements

NMR cryo-porometry is based on the suppression of melting/freezing point in confined liquids as described by equations in the methods section. Figure 3.11 follows the melting of water in all not-cleaved (NC) and cleaved (C) samples, with varying PEGDA concentration and PEGDA/cross-linker ratio (IT curve) . In all samples, the NMR signal intensity increases with temperature, as the water confined within the cross-linking networks melts. No further rise is observed past the bulk melting temperature suggesting that no water was present on the exterior of the gels. An increase in signal intensity is visible in the melting curve data of all cleaved samples compared to their not-cleaved particles, suggesting high water content confined within the cleaved networks. Moreover, as the PEGDA concentration is decreased (10%), the density of higher effective pores also increases. This behaviour is revealed in Figure 3.7, where there is a proportion of water, present within bigger pores, that melts at a higher temperature. These data indicate that 10R40 sample results the most porous, with a higher water content than other samples and this result is more evident differentiating the curve.

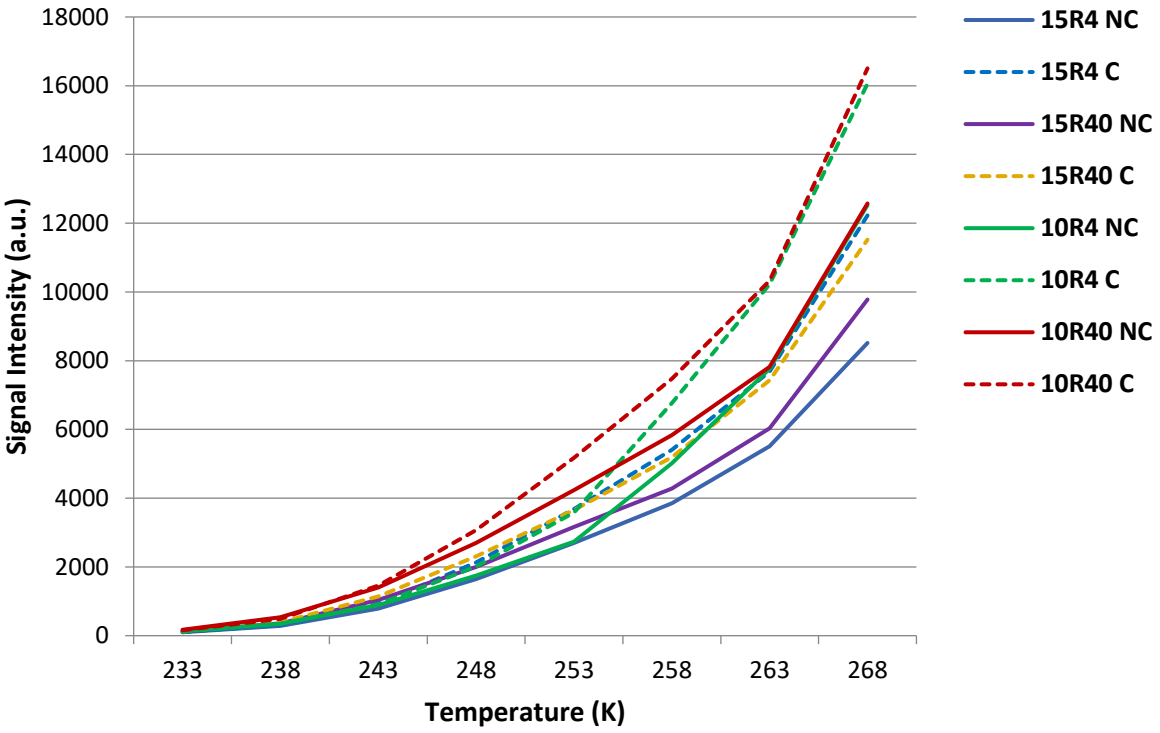

Figure 3.7: Variation of the NMR signal of water with the temperature for all the hydrogel compositions pre and post cleavage (IT curve).

Using equations 2 and 4, the IT curve in the figure 3.7 has been analysed in order to obtain a pore size distribution for all the hydrogel compositions. Since water as probe fluid for NMR cryoporometry has been largely studied in literature, its constant k is known and, in particular, is equal to 30 nm K^{23}. The figure 3.8 shows the derivative of the NMR signal with the inverse of the temperature (X=1000/T) and the data are fitted with a Gaussian equation. The intensity of this derivative is strictly connected with the quantity of pores at each X value and the parameter X is inversely proportional to the pore radius. Thus, lower values of X reflect the presence of larger pores[25], while the 3.66 K^{-1} value, where the origin of the axes is set, corresponds to the melting of bulk water. Through the equation 2, the fitting parameters for each curve in the graph can be used to evaluate the mean pore size. For all the compositions, the mean value lies in the range 3.85-3.87 K^{-1} which reflects a mean pore size of about 2.2 nm. This result is in accordance with the mean mesh size of the PEGDA700 10-15%, as already demonstrated by our group in previous works[26]. It is interesting to notice that, when X values are lower than 3.7 K^{-1} (pore diameter larger than 10 nm) the derivative dI/dX results to be more intense for the 10R40 and 10R4 samples, reflecting the presence of a bigger quantity of large pores compared with the non-cleaved microparticles and with pure PEGDA700 10-15%.

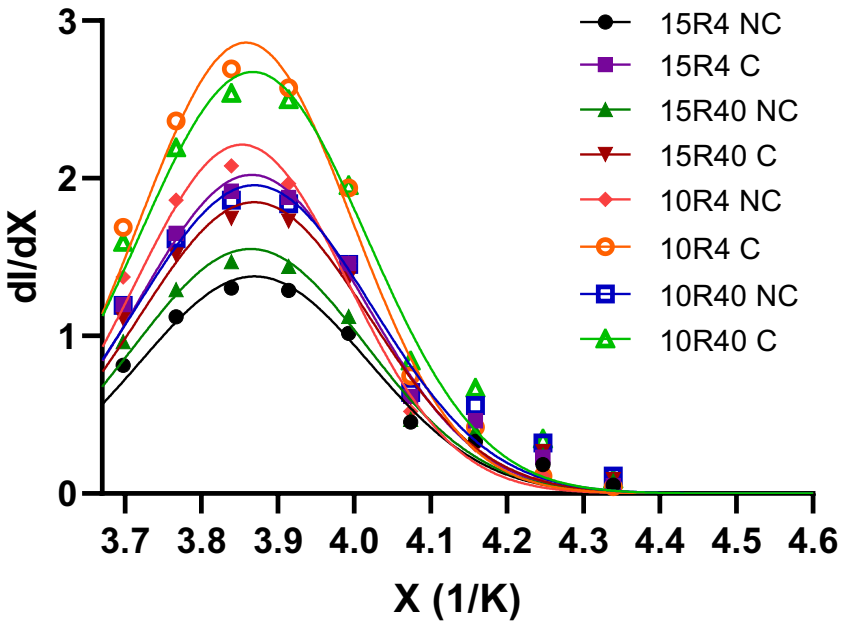

Figure 3.8: Derivative of the NMR signal with the inverse of temperature (1/K = X, proportional to pore radius r) for all the hydrogel compositions. Smaller X values represents larger pore and higher derivative intensities represent a bigger amount of pores.

3.3.5 Equilibrium partitioning measurements

To examine microstructural characteristics of these porous materials, the microparticles were equilibrated with fluorescently labelled antibodies, which were then imaged using confocal microscopy. Fluorescence was not observed in not-cleaved samples, which is expected as an antibody is larger than the mesh size of the PEG network at 10 and 15% PEGDA. Confocal images of the hydrogel microparticles suspended in 2µM IgG-FITC solution (Figure 3.9, left) revealed the equilibrium partitioning of antibodies within the microparticles. The figure 3.9 shows the equilibrium fluorescence profile inside a 10R40 microparticle, before and after the cleavage. It can be noticed how, with equal external fluorescence intensity (about 1500 a.u.) the cleaved microparticles exhibits a higher inner fluorescence respect to the non-cleaved one (about 5-fold). This data is reflected by the IN/OUT percentage ratio shown in figure 3.10.

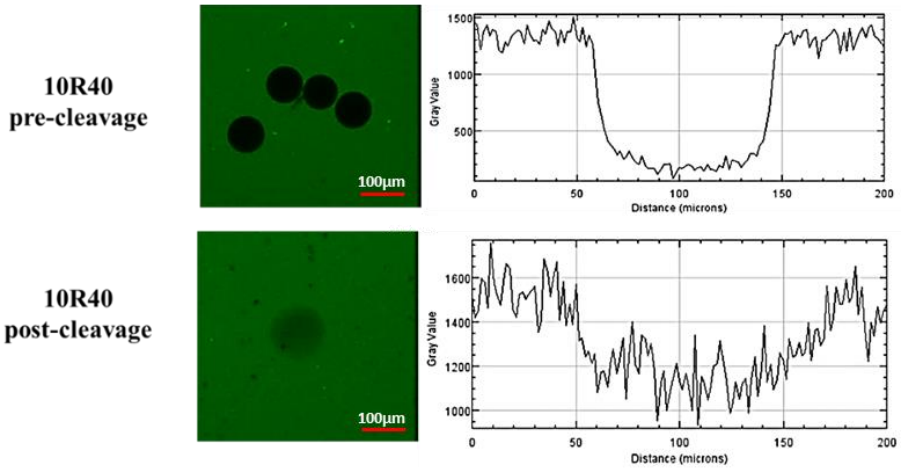

Figure 3.9: CLSM images (left) and equilibrium fluorescence signal profile (right) for the diffusion of a labelled IgG inside the hydrogel microparticles 10R40, before and after the cleavage.

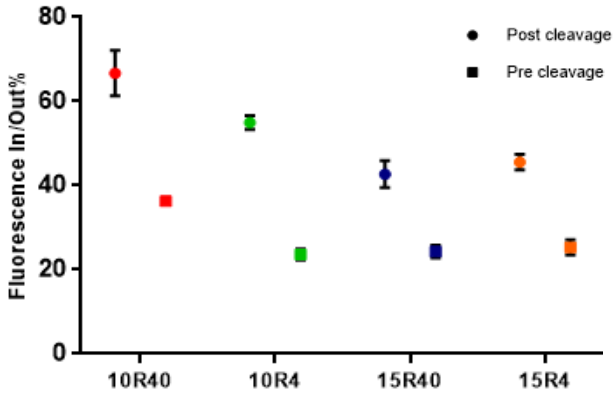

Figure 3.10: Fluorescence partition coefficient for the diffusion of a labelled IgG inside the hydrogel microparticles, before and after the cleavage.

As shown in figure 3.10, the partition coefficient of the labelled IgG is enhanced by the cleavage reaction for all kind of samples. In particular, in accordance with the previous experiments, the hydrogel microparticles 10R40 present the greater porosity, showing the higher ratio (IN/OUT) in fluorescence signal than other samples. Moreover, the ability of the protein to access the central region of the microparticle provides proof of the overall pore interconnectivity. Since our final aim is to perform a sandwich assay within the microparticles, it is necessary to verify if the size of the pores created is such as to allow the presence of a ternary complex. Since the size of the antibody is ~15 nm in its longest direction, the complex of three antibodies could extend to a maximum of 45 nm within the pores, therefore the diffusion of silica nanoparticles with the diameter of 50nm has been studied.

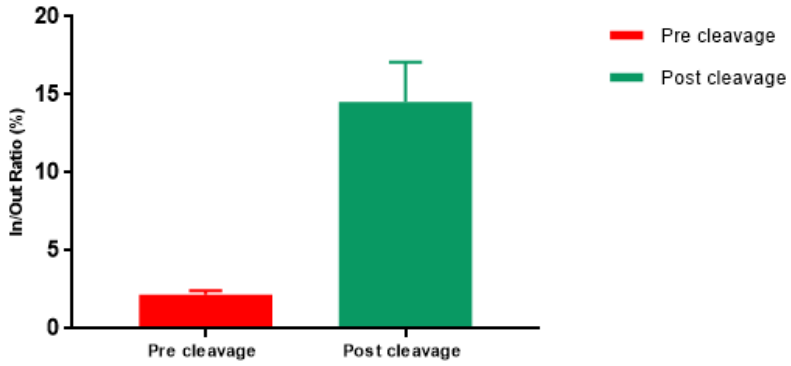

Figure 3.11: Fluorescence partition coefficient for the diffusion of labelled silica nanoparticles (diameter 50nm) inside the hydrogel microparticles 10R40, before and after the cleavage.

As shown in figure 3.11, the 10R40 cleaved microparticles allow the diffusion of the nanoparticles within the network, confirming the creation of pores with size of ~50 nm, suitable for the sandwich immunoassay.

3.3.6 Aldehydes titration

To calculate the number of aldehydes formed after the cleavage reaction, a titration of the aldehydes formed over time was performed using a colorimetric aldehyde quantitation kit. As shown in figure 3.12, the samples absorbance, and so the amount of aldehydes formed after the cleavage of 1000 microparticles, increases overtime until it reaches a plateau between 16 and 24 hours, confirming the cleavage time set by other previous experiment (overnight). From the standard curve (Figure 3.13) and the equation associated, a quantification of aldehydes can be obtained. In particular, the quantity of aldehydes formed in 16 hours is about 4 nmol in 1000

particles and, scaling for a single particle it is about 4pmol, in accordance with the amount of the cross-linker DHEBA present during the microparticle synthesis. (Figure 3.14).

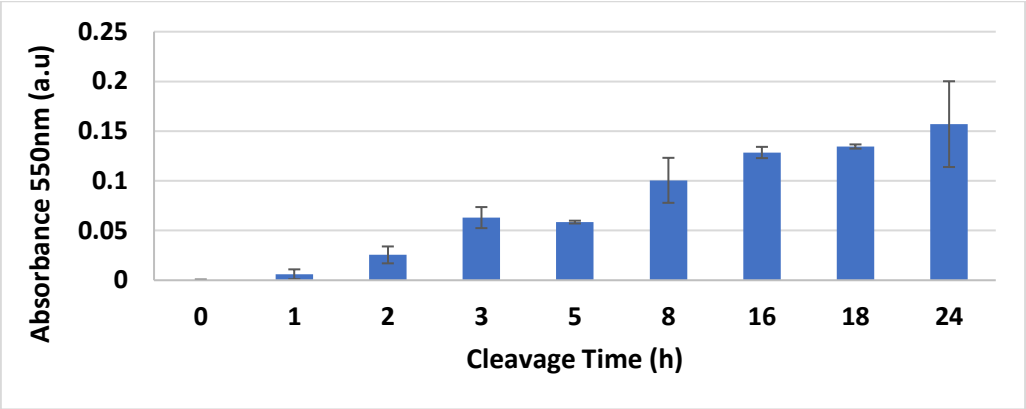

Figure 3.12: Aldehydes absorbance at 550nm over time evaluated on 1000 particles 10R40 per sample

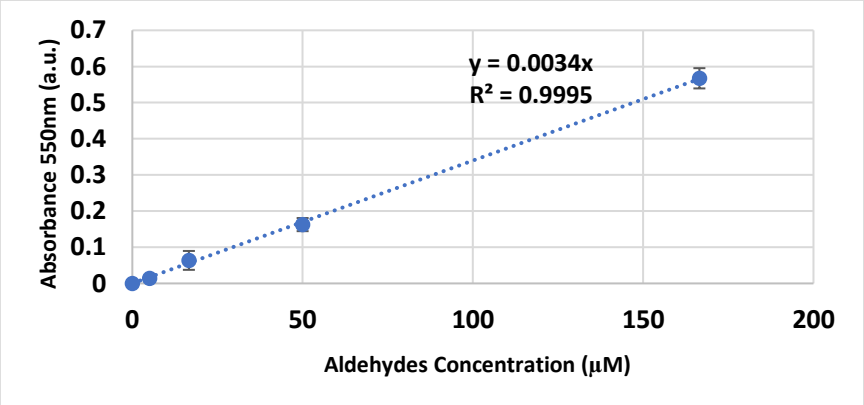

Figure 3.13: Aldehydes colorimetric kit standard curve

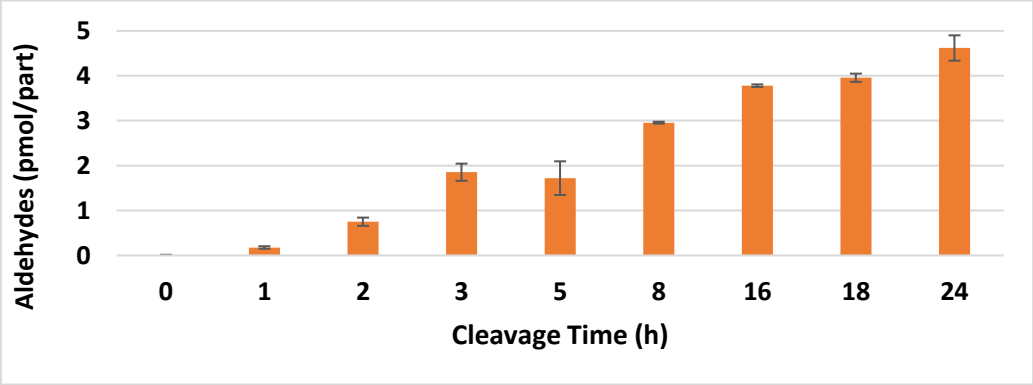

Figure 3.14: Quantity of aldehydes per particle over cleavage time, evaluated through the standard curve

The number of aldehydes calculated will be important for the functionalization steps of the microparticles with the primary antibody.

3.3.7 Fluorescence correlation spectroscopy measurements

In order to optimize the incubation time for the microparticles conjugation with the primary antibody, fluorescence correlation spectroscopy analysis was conducted for calculating the diffusion coefficient of the human IgG inside the hydrogel microparticles. The average autocorrelation functions of hIgG and atto647N, as molecules free in the solution and diffused within the hydrogel microparticles, are presented in Figure 3.15. The autocorrelation functions reveal the time required for a molecule to diffuse through a defined confocal volume. Diffusion is the macroscopic reflection of random thermal motions at molecular level and of the collisions between solvent and solute molecules.

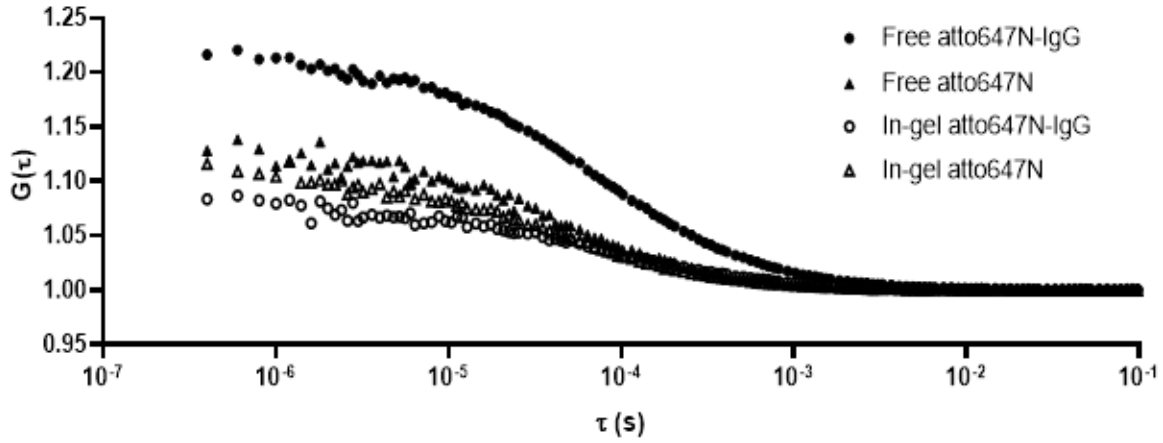

Figure 3.15: FCS average correlation functions G(τ) for atto647N and hIgG-atto647N in buffer and inside the hydrogel microparticles

To interpret the data obtained from FCS, several assumptions were made in order to obtain this correlation functions. First, since the porosity of the hydrogel was larger than the hydrodynamic radius of the diffusing solutes, the case of freely diffusing monodisperse fluorescent solutes was applied. Second, because low laser intensity was used, the excitation of molecular triplet states was not taken into consideration. For the labelled IgG, we have also assumed that only one fluorophore was attached to each protein molecule. For our labelling technique, we have calculated that there were 1.1 fluorophore molecules per each protein molecule, which validated this initial assumption. Furthermore, as the fraction of the non-attached Atto647 remaining from the IgG labelling process is very low (5%) we assume that it is negligible for the fitting.

In particular, from the mathematical point of view, the time sequence of the detected fluorescence intensity, I(t), emitted by the molecules in the confocal volume (V) at time t, is time-correlated to generate the autocorrelation function defined as:

$$G(\tau) = 1 + \frac{\langle \delta I(t) \delta I(t+\tau) \rangle}{\langle I(t) \rangle^2} \qquad (5)$$

where $\delta I(t) = I(t) - \langle I(t) \rangle$ denotes the deviation of the measured intensity from the average intensity $\langle I(t) \rangle$. Analysis of $G(\tau)$ provides information about the underlying mechanisms for the intensity fluctuations. For an ideal case of freely diffusing monodisperse and uniformly bright fluorescent particles an expression for the correlation function can be derived as:

$$G(\tau) = 1 + \frac{1}{N} \frac{1}{(1+(\tau/\tau_D))} \frac{1}{(1+p(\tau/\tau_D))^{0.5}} \qquad (6)$$

where N denotes the average number of particles in the excitation volume, τ the delay time, τ_D the characteristic diffusion time, and p an instrumental constant. Assuming that the fluorescent diffusing molecules are excited by a 3D Gaussian beam, the characteristic time for fluorescent particles diffusing along the lateral width (r_o) of the focused incident laser beam is defined as:

$$\tau_D = \frac{(r_0)^2}{4D} \qquad (7)$$

where D denotes the translational diffusion coefficient of the particles in the host medium.

According to these models, we measured the number of molecules crossing the confocal volume per unit of time and the diffusional time required for the molecules to cross the confocal volume. The diffusion coefficients of the molecules were determined both in solution and inside the hydrogel matrix through the fitting (Eq. 6) of the autocorrelation functions shown in figure 3.15. The results, summarized in Table 3.2, demonstrate that atto647N does not interact with the hydrogel network and that the IgG diffuses inside the matrix almost as in buffer, with a decrement in diffusion coefficient of about 8%. Considering the big size of the IgG molecules, the decrement in its diffusion is very low[27]. This demonstrates that the hydrogel microparticles are porous enough to perform a fast immunoassay. In fact, assuming a unidirectional diffusion of the antibodies inside the microparticles with a 55µm average radius, the time needed to fill the particle is less than 1 minute.

Table 3.2: Mean diffusion coefficients in buffer (D_0) and in gel (D_{gel}) and their ratios D_{gel}/D_0 for atto647N and for hIgG-atto647N.

	D_0 ($\mu m^2/s$)	D_{gel}	D_{gel}/D_0
Atto647N	160	133.7±17.0	0.89±0.13
HIgG-atto647N	68.5±2.1	63.6±15.8	0.92±0.07

3.4 Conclusions

In conclusion, here we report the microfluidic synthesis and Physico-chemical characterization of porous hydrogel microparticles. We successfully synthesized monodisperse cleavable PEG-based microparticles through the use of a cleavable cross-linker DHEBA. This technique presents several advantages such as: the simultaneous creation of pores and reactive groups, the possibility to functionalize post-synthesis the particles with any biomolecule without changing the pre-polymer solution, which avoid an optimization of the fluid dynamic parameters for every type of biomarker. In fact, since changing the pre-polymer solution means to vary its viscosity and interfacial tension with oil, it is necessary to change the fluid dynamic parameters in order to obtain particles with same size and productivity.

The volumetric swelling, the kinetics analysis, the NMR cryoporometry and the aldehydes titration allowed to optimize the cleavage reaction conditions and gave important information about the relative porosity of all the hydrogel composition tested. Moreover, the equilibrium partitioning and FCS analysis demonstrated that the cleaved hydrogel microparticles allow the passage of single antibodies and complexes without any significant interaction with the gel network. This can be addressed to the high porosity of the microparticles and to the PEG's anti-fouling properties.

3.5 References

1. Peppas, N. A., Hilt, J. Z., Khademhosseini, A. & Langer, R. Hydrogels in Biology and Medicine: From Molecular Principles to Bionanotechnology. *Adv. Mater.* **18**, 1345–

1360 (2006).

2. Peppas, N. A., Keys, K. B., Torres-Lugo, M. & Lowman, A. M. Poly(ethylene glycol)-containing hydrogels in drug delivery. *J. Control. Release* **62**, 81–87 (1999).

3. Nguyen, K. T. & West, J. L. Photopolymerizable hydrogels for tissue engineering applications. *Biomaterials* **23**, 4307–4314 (2002).

4. Lee, K. Y. & Mooney, D. J. Hydrogels for Tissue Engineering. *Chem. Rev.* **101**, 1869–1880 (2001).

5. Ma, Y. *et al.* Portable visual quantitative detection of aflatoxin B 1 using a target-responsive hydrogel and a distance-readout microfluidic chip. *Lab Chip* **16**, 3097–3104 (2016).

6. Chapin, S. C. & Doyle, P. S. Ultrasensitive multiplexed microRNA quantification on encoded gel microparticles using rolling circle amplification. *Anal. Chem.* **83**, 7179–7185 (2011).

7. Srinivas, R. L., Chapin, S. C. & Doyle, P. S. Aptamer-functionalized microgel particles for protein detection. *Anal. Chem.* **83**, 9138–9145 (2011).

8. Chapin, S. C., Appleyard, D. C., Pregibon, D. C. & Doyle, P. S. Rapid microRNA profiling on encoded gel microparticles. *Angew. Chemie - Int. Ed.* **50**, 2289–2293 (2011).

9. Kawaguchi, H. Functional polymer microspheres. *Progress in Polymer Science (Oxford)* vol. 25 1171–1210 (2000).

10. Kim, J., Heo, J. & Crooks, R. M. Hybridization of DNA to Bead-Immobilized Probes Confined within a Microfluidic Channel. *Langmuir* **22**, 10130–10134 (2006).

11. Rubina, A. Y., Kolchinsky, A., Makarov, A. A. & Zasedatelev, A. S. Why 3-D? Gel-based microarrays in proteomics. *Proteomics* **8**, 817–831 (2008).

12. Ferrer, G. G. *et al.* Influence of the nature of the porous confining network on the sorption, diffusion and mechanical properties of hydrogel IPNs. *Eur. Polym. J.* **46**, 774–782 (2010).

13. Bajpai, S. K., Bajpai, M. & Sharma, L. Investigation of Water Uptake Behavior and Mechanical Properties of Superporous Hydrogels. *J. Macromol. Sci. Part A* **43**, 507–524 (2006).

14. Chen, J., Blevins, W. E., Park, H. & Park, K. Gastric retention properties of superporous hydrogel composites. in *Journal of Controlled Release* vol. 64 39–51 (2000).

15. Choi, D., Jang, E., Park, J. & Koh, W. G. Development of microfluidic devices incorporating non-spherical hydrogel microparticles for protein-based bioassay. *Microfluid. Nanofluidics* **5**, 703–710 (2008).

16. Choi, N. W. *et al.* Multiplexed Detection of mRNA Using Porosity-Tuned Hydrogel Microparticles. *Anal. Chem.* **84**, 9370–9378 (2012).

17. Wu, Y. H., Park, H. B., Kai, T., Freeman, B. D. & Kalika, D. S. Water uptake, transport and structure characterization in poly(ethylene glycol) diacrylate hydrogels. *J. Memb. Sci.* **347**, 197–208 (2010).

18. Al-Ameen, M. A., Li, J., Beer, D. G. & Ghosh, G. Sensitive, quantitative, and high-throughput detection of angiogenic markers using shape-coded hydrogel microparticles. *Analyst* **140**, 4530–4539 (2015).

19. Nayak, S., Gan, D., Serpe, M. & Lyon, L. ?Andre. Hollow Thermoresponsive Microgels. *Small* **1**, 416–421 (2005).

20. Tripathi, B. P., Dubey, N. C. & Stamm, M. Hollow Microgel Based Ultrathin Thermoresponsive Membranes for Separation, Synthesis, and Catalytic Applications. *ACS Appl. Mater. Interfaces* **6**, 17702–17712 (2014).

21. Nayak, S. & Lyon, L. A. Ligand-functionalized core/shell microgels with permselective shells. *Angew. Chemie - Int. Ed.* **43**, 6706–6709 (2004).

22. Zhong, Y.-L. & Shing, T. K. M. Efficient and Facile Glycol Cleavage Oxidation Using Improved Silica Gel-Supported Sodium Metaperiodate. *J. Org. Chem.* **62**, 2622–2624 (1997).

23. Petrov, O. V. & Furó, I. NMR cryoporometry: Principles, applications and potential. *Prog. Nucl. Magn. Reson. Spectrosc.* **54**, 97–122 (2009).

24. Leutenegger, M., Ringemann, C., Lasser, T., Hell, S. W. & Eggeling, C. Fluorescence correlation spectroscopy with a total internal reflection fluorescence STED microscope (TIRF-STED-FCS). *Opt. Express* **20**, 5243 (2012).

25. Rottreau, T., Parlett, C., Lee, A., Mesoporous, R. E.-M. and & 2018, undefined. NMR

cryoporometric measurements of porous silica: A method for the determination of melting point depression parameters of probe liquids. *Elsevier*.

26. Mazzarotta, A. *'Engineered Hydrogel-Based Materials For Oligonucleotide Detection'*. PhD Thesis. *fedoa.unina.it* (2014).

27. Zustiak, S. P., Boukari, H. & Leach, J. B. Solute diffusion and interactions in cross-linked poly(ethylene glycol) hydrogels studied by Fluorescence Correlation Spectroscopy. *Soft Matter* **6**, 3609–3618 (2010).

4. Development and Optimization of in-gel Sandwich Assay for Protein Detection

4.1 Introduction

Advances in medical diagnostics and patient-tailored therapy require robust methods for the sensitive and rapid measurement of proteins. Traditionally, protein detection has been carried out with the time- and labour-intensive enzyme linked immunosorbent assay (ELISA), exploiting the variety and specificity of antibodies. Because of the great quantity of validated antibody pairs available, the sandwich ELISAs are the most common implementation of the assay. This detection scheme has been adapted for a number of platforms, including planar and particle arrays. Long incubation times and low throughput of the format make planar arrays unsuitable for the rapid sample processing for diagnostic applications. For this reason, there has been an ever-increasing interest in technologies based on hydrogel microparticles for diagnostics[1–3], but also for a wide variety of biotech applications like drug delivery[4,5], and tissue engineering[6–8]. In particular, hydrogel microparticles have been widely used as a versatile tool to perform immune-enzymatic assays due to their hydrophilic, biocompatible and highly flexible chemical and physical properties[9]. In the diagnostic field, hydrogel coatings and gel dot surface microarrays, were successfully used in sensitive nucleic acid assays and immunoassays[10–12]. More recently, new micro-fabrication techniques for synthesizing encoded hydrogel particles have enabled the development of hydrogel-based suspension arrays[13,14]. As a result of their chemical flexibility, hydrogels can be engineered to capture and detect specific analytes including but not limited to proteins, DNA, microRNA (miRNA) and antibodies[15–18]. As shown in figure 4.1, hydrogel microparticles for diagnostics should present several important characteristics that can be modulated depending on the final application[19]:

- Porosity allowing the diffusion of selected molecules (molecular sieving)
- High diffusion coefficient and accessibility for the analytes inside the network
- Appropriate reactive groups to conjugate the hydrogel microparticle with a specific recognition element (i.e. antibody)
- Simple and sensitive read out (fluorescence or colorimetric)
- Possibility to introduce a unique recognition code (fluorophores, bar codes…) which identifies a single particle to perform multiplexed analysis.

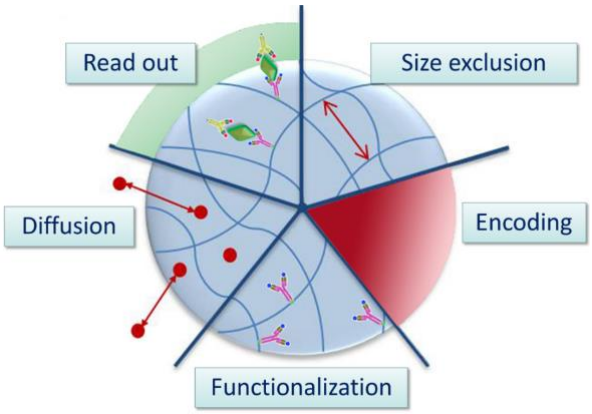

Figure 4.1: Schematic illustration of a hydrogel microparticle for diagnostic and its principal characteristics.

The use of hydrogels microparticles allow the functionalization of the entire bulk.[20–2324]. Compared to flat surfaces or non-porous beads, these 3-dimensional particles offer significantly higher surface areas for immobilization of capture probes[25,26], thereby providing enhanced binding capacity, and consequently sensitivity. Moreover, some hydrogel materials can contribute to enhance the assay specificity. In particular, from the literature, the poly(ethylene)glycol (PEG) emerges as the perfect candidate to synthesise hydrogel microparticles with anti-fouling properties, preventing non-specific interactions between the gel and interfering biomolecules [27,28].

In this chapter, we present the development and optimization of an innovative in-gel sandwich assay for the detection of human immunoglobulin G (IgG) in biological fluids. Our detection system is based on finely engineered the cleavable hydrogel microparticles, synthesized and characterized as shown in chapters 2 and 3. Several studies on the specificity and selectivity of our system have been conducted and the optimized hydrogel microparticles have been used to perform a sandwich assay on IgG in human serum and urine, as shown in figure 4.2.

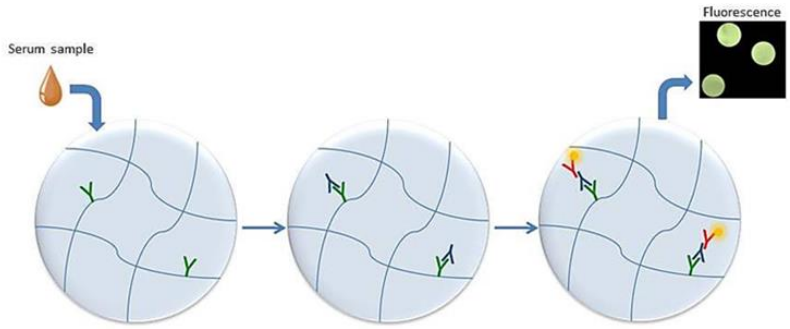

Figure 4.2: Schematic illustration of a fluorescent sandwich immuno-assay on serum performed in hydrogel microparticles

4.2 Materials and Methods

All the hydrogel microparticles used in the experimental part of this chapter were synthesized, optimized and characterized as already described in the chapters 2 and 3. The number of hydrogel microparticles was evaluated by diluting the stock suspension and spotting 10 drops (10µL each) on a thin glass slide. The drops were visualized with an inverted microscope (IX 71 Olympus) equipped with a 10x objective, and the microparticles in each drop were counted and mediated. Then, the mean number of particles in 10µL of diluted suspension was multiplied for the dilution factor to evaluate the number of particles contained in 10µL of the stock suspension.

4.2.1 Labelling of antibodies

The human Immunoglobulin G (hIgG, Sigma Aldrich) and the monoclonal anti-human IgG FAB specific (antih-IgG FAB, Sigma Aldrich) were labelled with a fluorophore exploiting the amino groups. In detail, reaction was carried out with 0.55 mg of hIgG (and antih-IgG FAB) and 30µm of ATTO647N-N-Hydroxysuccinimide for 30 min at room temperature. After the reaction, the conjugates (hIgG-atto647N and antih-IgGFAB647) were dialysed and characterized through a spectrophotometric measurement to calculate their concentration and degree of functionalization.

4.2.2 Primary antibody optimization

In order to optimize the primary antibody concentration for the conjugation to microparticle bulk, two different concentrations of monoclonal antihuman IgG FC specific (anti hIgG-FC, Sigma Aldrich) antibody have been explored. 0.1 pmol/particle and 1pmol/particle, in presence of 5% v/v of 5M sodium cyanoborohydride ($NaCNBH_3$, Sigma Aldrich) in Sodium Bicarbonate 0.1M. After several washes with buffer solutions, 1nM of labelled target (hIgG-atto647N) (Sigma Aldrich) was added and incubated for 90 minutes (37°C, 500rpm). After several washing steps, confocal images at microscope (CLSM Leica SP5, Objective 10x DRY, scan speed of 400 Hz, excitation wavelength 633, emission wavelength 648-710nm) were acquired and analysed using ImageJ software to evaluate the fluorescence intensity.

4.2.3 Reporter antibody optimization

In order to optimize the reporter concentration, hydrogel microparticles were conjugated adding 0.1 pmol/particle of anti hIgG-FC. After several washes with buffer solutions, 1nM of atto647-

human IgG was added and incubated for 90 minutes (37°C, 500rpm). The sample was finally split into separated Eppendorf tubes and then different concentrations (0.1, 0.2, 0.5, 1, 5nM) of atto647-labelled antihuman IgG FAB specific (antihIgG-FAB647) were added and incubated for 90 minutes. After several washes, confocal images at microscope (CLSM Leica SP5, Objective 20x DRY, scan speed of 400 Hz, excitation wavelength 633, emission wavelength 648-710nm) were acquired and analysed using ImageJ software to evaluate the fluorescence intensity.

4.2.4 Particles number modulation experiments for the evaluation of sensitivity variations

Cleaved hydrogel microparticles were conjugated with 0.1 pmol/part anti hIgG-FC. After several washes, three different concentrations of hIgG-atto647 (0.1, 0.5 and 1nM) were added to 10, 50 and 100 microparticles (total reaction volume 100µL) and incubated for 90 minutes (37°C, 500rpm). After subsequent washes, confocal images at microscope (CLSM Leica SP5, Objective 10x DRY, scan speed of 400 Hz, excitation wavelength 633, emission wavelength 648-710nm) were acquired and analysed with ImageJ software.

4.2.5 Sandwich assay and cross-reactivity tests

To perform the sandwich assay, cleaved hydrogel microparticles were firstly conjugated adding 0.1 pmol/particle of anti hIgG-FC (Overnight, RT, 500rpm). Then the conjugated microparticles were washed and incubated for 90 minutes, at 37°C and 500 rpm with different concentrations of h-IgG (0, 0.1, 0.5, 1, 10, 30, 60, 100, 200, 400, 600, 1000pM) in a total reaction volume of 100µL. After several washes, the microparticles were finally incubated for 90 minutes with the antihIgG-FAB647 1nM. The CV% inter-assay that measures consistency of replicate samples between experiments (% CV best if <15%), was calculated as follow:

$$\%CV = \left(\frac{Standard\ deviation_{Replications}}{Mean_{Replications}}\right) * 100 \qquad (1)$$

The means for high and low signals are calculated and then used to calculate the overall mean, standard deviation, and % CV. The average of the high and low % CV is reported as the inter-assay CV.

The limit of detection (LOD) was evaluated on the linear part of the calibration curve as follows:

$$LOD = {}^{3\sigma_0}/_{S}$$

Where σ_0 represents the standard deviation on the signal of the sample with no target (zero) and S is the slope of the linear part of the calibration curve.

In order to study the specificity of the assay two different experiments were performed: the first one using Human Serum Albumin (HSA) as target and the other one using an antibody non-specific for the IgG as primary antibody. In the first experiment, the cleaved hydrogel microparticles were conjugated as described before and then incubated for 90 minutes with different concentration of HSA (37°C, 500 rpm) and finally incubated with antihIgG-FAB647 (90 minutes, 37°C, 500 rpm). Regarding the second experiment, cleaved hydrogel microparticles were conjugated adding 0.1 pmol/particle of a non-specific antibody (overnight, room temperature, 500rpm). The conjugated microparticles were then washed and incubated for 90 minutes, at 37°C and 500 rpm with different concentration of human IgG. After several washes, the microparticles were finally incubated for 90 minutes with the antihIgG-FAB647 1nM.

Moreover, the selectivity of the assay was investigating performing a sandwich assay in buffer with an excess of HSA as interfering molecule. The cleaved conjugated hydrogel microparticles were incubated for 90 minutes with different mixture samples, containing a defined HSA concentration (3nM) and varying concentrations of IgG (37°C, 500 rpm). After several washes, microparticles were finally incubated with antihIgG-FAB647 (90 minutes, 37°C, 500 rpm).

All the experiments were carried out with ten particles per sample and the error is represented as SEM (Standard error of the mean). Confocal images (CLSM Leica SP5, Objective 10x DRY, scan speed of 400 Hz, excitation wavelength 633, emission wavelength 648-710nm) were recorded and analysed with ImageJ software to evaluate the fluorescence intensity. The fluorescence emission of blank functionalized microparticles have been acquired and its value has been subtracted from the signal intensity of each point.

4.2.6 Sandwich assay in complex fluids

To test suitability of the in-particles assay for the direct use in biological samples, several studies in Fetal Bovine Serum (FBS) and in synthetic urine were conducted. In the first experiment, the antibody-conjugated hydrogel microparticles were incubated in FBS diluted 1:5 for 90 minutes with different concentration of IgG (37°C, 500 rpm). Particles were washed, incubated with antihIgG-FAB647 (90 minutes, 37°C, 500 rpm), washed again and finally imaged. Regarding the second experiment, synthetic urine was prepared as an aqueous mixture

solution of salts and human serum albumin (HSA) in the following concentrations: CaCl 0.44 g/l, $MgCL_2*2H_2O$ 0.52 g/l, Urea 25 g/l, NaCl 4.8 g/l, Na_2SO_4 2.34 g/l, KCl 1.5 g/l, NH_4Cl 1 g/l, HSA 10 g/l. Cleaved hydrogel microparticles were conjugated, washed and incubated in synthetic urine with different concentration of human IgG for 90 minutes, at 37°C and 500 rpm. After several washes, the microparticles were finally incubated for 90 minutes with the antihIgG-FAB647 1nM and then imaged.

The assay in extracted human serum samples (Sigma Aldrich) was performed by diluting the serum up to 60million times to obtain four concentrations of human IgG (assuming that the total concentration in serum was 10 mg/ml): 1, 10, 100 and 1000pM.

All the experiments were carried out with ten particles per sample, the error is represented as SEM and the LOD was calculated as mentioned in paragraph 4.2.4. The confocal images were registered using CLSM Leica SP5 (Objective 10x DRY, scan speed of 400 Hz, excitation wavelength 633, emission wavelength 648-710nm) and analysed with ImageJ software to evaluate the fluorescence intensity. The fluorescence emission of blank functionalized microparticles have been acquired and its value has been subtracted from the signal intensity of each point.

4.2.7 Sandwich assay on 5 microparticles

A sandwich assay on 5 microparticles was performed to evaluate an improving of the limit of detection of the assay. The assay was executed as already described in the paragraph 4.2.4, with a hIgG concentration range going from 0 to 100pM. The antihIgG-FAB647 concentration used is 500pM. The error is represented as SEM.

4.3 Results and discussion

4.3.1 Primary and reporter antibody optimization

After demonstrating the generation of aldehydes groups after cleavage reactions and the accessibility of a ternary antibody complex (~ 45 nm) within the porous network of hydrogel microparticles (chapter 3), we have developed a novel, sensitive in-gel immunoassay. First, the primary antibody concentration has been optimized. Basing on the moles of aldehydes calculated in chapter 3, two concentrations of primary antibody (antihIgG-FC) for the

microparticle conjugation step were studied (0.1 and 1 pmol per particle). The response of these differently conjugated particles was assessed after their incubation with two different concentrations of fluorescent target atto647-hIgG (100 and 500 pM). After washing the microparticles to remove the unbounded atto647-hIgG, the fluorescence from the droplets were evaluated. As shown in figure 4.3, hydrogel microparticles functionalized with the lower concentration present a more homogeneously distributed fluorescence within the microparticles than those functionalized with the highest concentration of antihIgG-FC. This inhomogeneity in the fluorescence distribution is very evident at lower target concentration. Since the binding reaction is faster than the complete diffusion of all target molecules, when the microparticles are conjugated with a too high concentration of hIgG-FC and atto647-hIgG results the limiting component, the target forms a fluorescent ring, without reaching the centre of the particle. The best strategy to explore an extremely low range of target concentrations (pM range) results in using 0.1 pmol/part hIgG-FC conjugated microparticles.

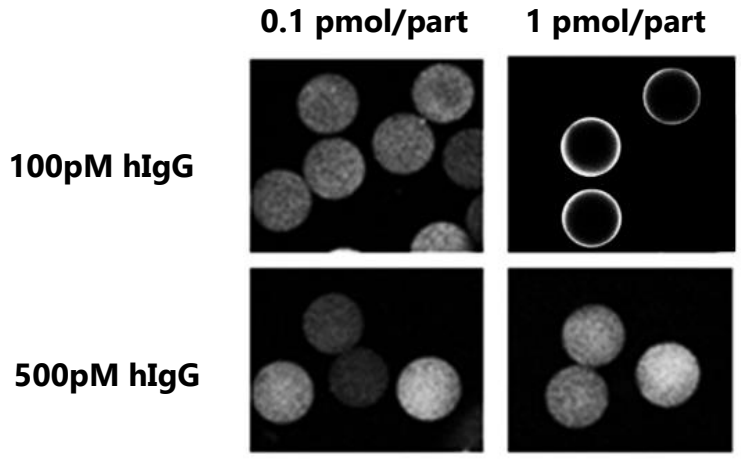

Figure 4.3: CLSM images data of hydrogels microparticles with two concentrations of antihIgG-FC (0.1 and 1 pmol/part), used to detect atto647-hIgG at 100pM and 500pM

After primary antibody optimization, the reporter antibody concentration was optimized to perform the final sandwich assay. The hIgG-FC conjugated-microparticles were incubated with 1 nM hIgG, and subsequently, different concentrations of labelled antihIgG-FAB have been explored. As the figure 4.4 shows, the fluorescence intensity increases until a plateau was reached above the incubation with 1 nM reporter antibody. Then a further increase in the signal can be noticed, corresponding to the 5nM antihIgG-FAB, but this signal is characterized by a high inhomogeneity (high standard deviation), probably due to difficulties in removing the

unbounded reporter antibody with washes. Consequently, the reporter antibody concentration of 1nM is chosen.

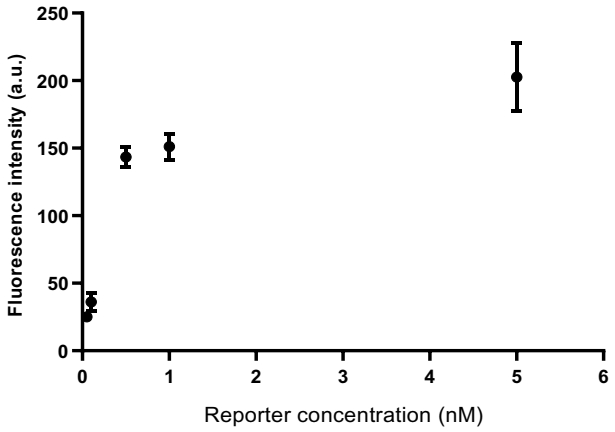

Figure 4.4: Experimental data of sandwich assay performed on hydrogel microparticles with different concentrations of labelled antihIgG-FAB (reporter antibody)

4.3.2 Influence of particles number on fluorescence signal

To study the influence of particle number on responsivity of the assay, the capture of different concentrations of fluorescently labelled hIgG was studied by modulating the number of microparticles. In details, primary antibody conjugated-microparticles in number of 10, 50 and 100 were incubated with three different concentrations of atto647-hIgG. As showed in figure 4.5, comparing each target concentration, the fluorescence signal intensity increases by lowering the particles number. This behaviour can be addressed to the capacity of the hydrogel microparticles to concentrate the analyte in a very small region, amplifying the fluorescence signal. The lower the particles number in which the analyte is confined, the more intense the signal emitted results.

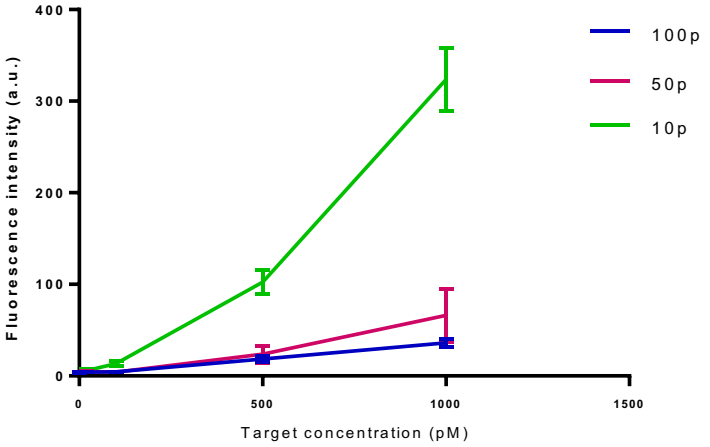

Figure 4.5: Experimental data of different concentrations of atto647 labelled hIgG captured by 100, 50 and 10 hydrogel microparticles

According to this data, all the further experiments were performed with 10 particles in order to have a limit of detection as low as possible.

4.3.3 Sandwich assay and cross-reactivity tests

The optimized hydrogel microparticles were finally used to perform a sandwich assay on hIgG in TRIS buffer 0.1 M pH 8 as calibration. We tested the detectivity of these microparticles in the picomolar range to characterize their detection limits. In details, 10 antihIgG-FC-conjugated microparticles were incubated with different concentrations of hIgG exploring a range from 0.1 to 1000 pM. The reporter antibody concentration is fixed at 1nM for all samples. The fluorescence emission of the labelled antihIgG-FAB versus the target hIgG concentration is plotted (Figure 4.6) showing a specific dose-response binding curve where fluorescent signal increased with increase in hIgG concentration. Since photopolymerized hydrogel microparticles could exhibit a slight autofluorescence, the emission of blank microparticles have been acquired and the value of this background has been subtracted from the signal intensity of each point. The curve is fitted with Langmuir equation, allowing estimation of the dissociation binding constants K_d equal to 280.2 pM. The linear part of the curve was used to calculate the LOD of the assay, which was found to be 4.2pM (corresponding to 0.63 ng/ml).

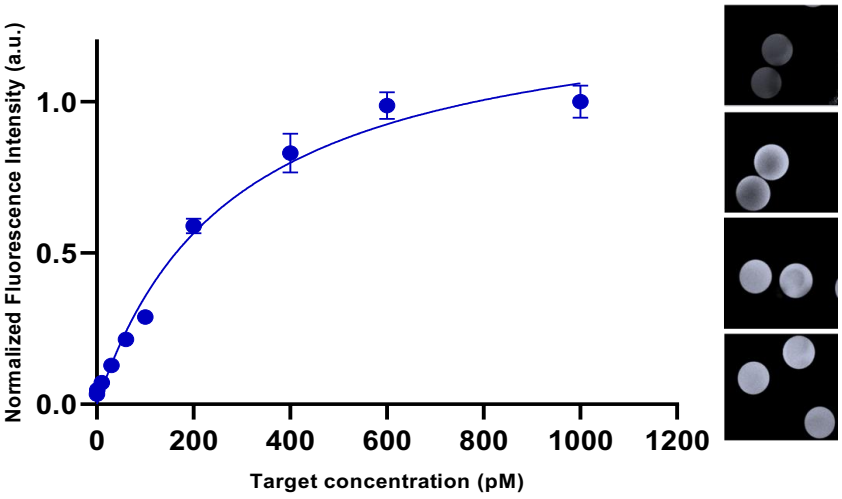

Figure 4.6: Experimental data of sandwich assay on hIgG and HSA performed on hydrogel microparticles and CLSM images of fluorescent particles at different target concentrations.

Moreover, we calculated coefficient of variation (CV) % inter-assay of 9.72%. This result shows that our assay is approaching the confidence level of the well-established ELISA (CV% inter-assay 10-17%). Furthermore, selectivity test was performed to demonstrate that our assay can detect selectively hIgG even in presence of interfering molecule present in complex biological fluids (as Human Serum Albumin). The assay was carried out adding an excess of HSA (fixed to 3 nM) to different concentrations of target hIgG. Figure 4.7 demonstrates how HSA does not interfere with the responsivity of the assay, since the curves are almost overlayable.

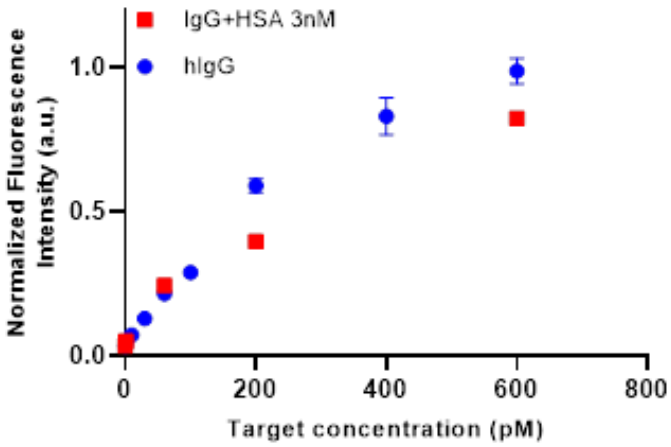

Figure 4.7: Experimental data of sandwich assay on hIgG performed into a mixture of TRIS and HSA, compared with the one performed in TRIS 0.1M

In order to study the specificity of the assay, two experiments were performed. In the first experiment, the primary antibody has been replaced with a non-specific one. The microparticles were conjugated at the same conditions used for the antihIgG-FC. After incubation with the hIgG target and the reporter antihIgG-FAB, the fluorescence intensities from the microparticles were accessed and quantified. As figure 4.8 shows, the fluorescence intensity drastically decreases in the microparticles conjugated with an unrelated antibody. These data demonstrate that in our assay the hIgG target is specifically recognized by the primary antibody antihIgG-FC conjugated within microparticles, without any non-specifically adsorption onto the material or physical entrapment.

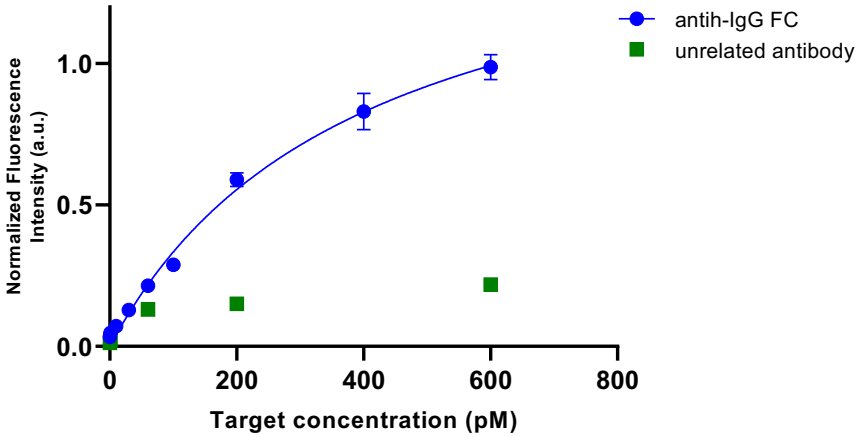

Figure 4.8: Experimental data of sandwich assay on hIgG with particles conjugated with an unrelated antibody, compared with the specific one

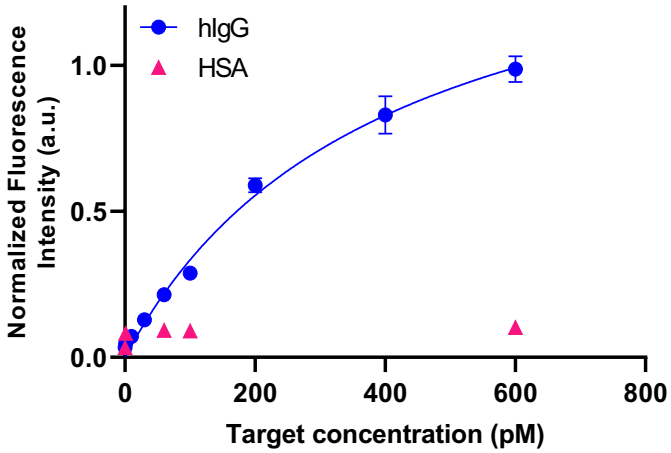

Figure 4.9: Experimental data of sandwich assay on hIgG compared with the sandwich assay performed on a non-specific molecule (HSA)

Another experiment is performed by replacing the target with a non-specific biomolecule, like human albumin. The microparticles were conjugated with the antihIgG-FC and incubated with different concentration of HSA. The labelled antihIgG-FAB concentration is fixed at 1nM for all samples. As seen in figure 4.9, the HSA is not recognized by the particles, so this developed system shows a high specificity.

4.3.4 Sandwich assay in complex fluids

One of the major difficulties in protein assay is the rise of fluorescent signal, either due to non-specific adsorption within microparticles or due to non-specific interaction with immobilized antibody. To further investigate whether other components of serum can affect fluorescent signal, antihIgG-FC immobilized microparticles were incubated with different concentrations of hIgG in FBS and in synthetic urine. The experimental data regarding the assay in FBS, shown in figure 4.10, demonstrate that the system can detect the target even in presence of a lot of interfering molecules with a limit of detection of 13pM (1.95ng/ml) and a dose-response curve very similar to the one in buffer. The same result is obtained in the case of synthetic urine (figure 4.11), but with a higher limit of detection (3.45ng/ml). Nevertheless, compared with the same sandwich assay on IgG in urine performed onto the surface of gold nanoparticles[29], our in-gel assay presents a 2.3-fold lower limit of detection.

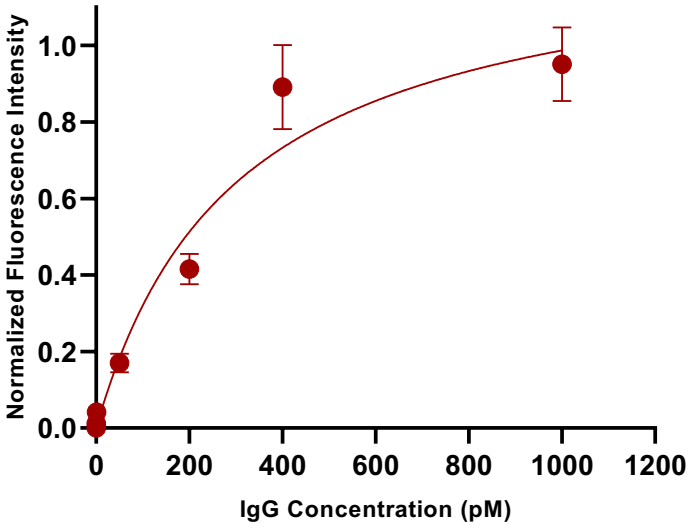

Figure 4.10: Experimental data of sandwich assay on hIgG in FBS 1:5

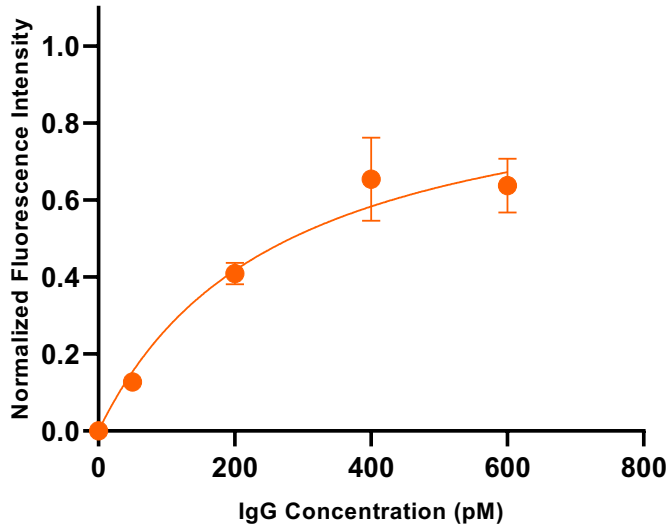

Figure 4.11: Experimental data of sandwich assay on hIgG in synthetic urine

In order to test the conjugated hydrogel microparticles in a complex fluid with an unknown concentration of hIgG, an assay in human serum was performed, testing different dilutions of the serum corresponding to a dilution of the concentration of hIgG. Assuming that the total hIgG concentration in serum was 10 mg/ml, we explored a theoretical concentration range from 1 to 1000pM corresponding to 10^5 to 10^8 dilutions. As figure 4.12 shows, our system can detect the hIgG antibodies in serum, giving a dose-response curve in which the signal decreases while the dilution factor increases.

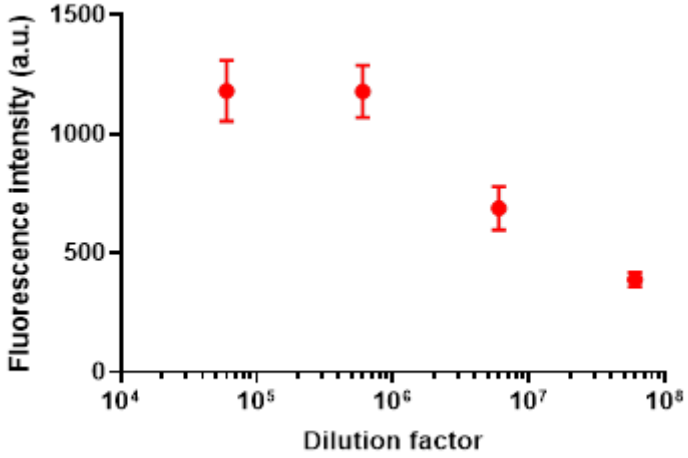

Figure 4.12: Experimental data of sandwich assay on hIgG in diluted synthetic human serum

4.3.5 Sandwich assay on 5 microparticles

As expected from the preliminary data in figure 4.5, lowering the number of particles used in the assay increases the sensitivity of the system (Figure 4.13). In fact, the limit of detection decreases, going from 4.2pM to 3pM, when we use 5 particles instead of 10. Compared with a commercial ELISA kit (Invitrogen) to quantify total IgG and with a magnetic bead-based assay on mouse IgG[30], our in-gel immuno-assay shows a higher sensitivity and a comparable assay time (Table 4.1).

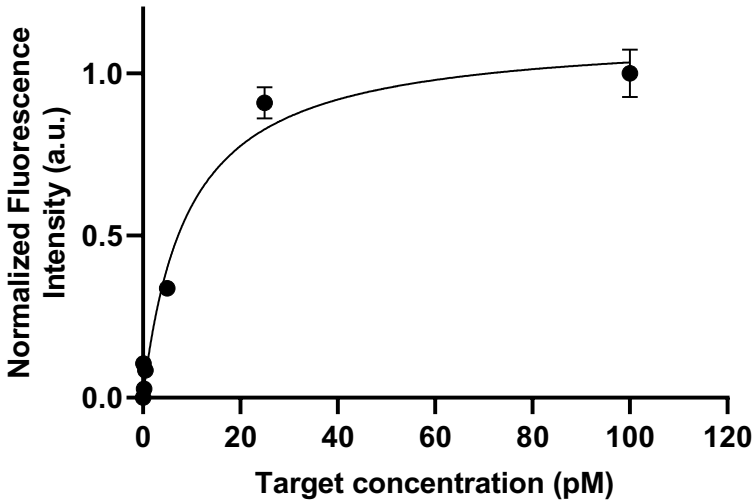

Figure 4.13: Experimental data of sandwich assay on hIgG performed in buffer with 5 hydrogel microparticles

Table 4.1: Performances comparison between commercial ELISA kit and our hydrogel microparticles

	DETECTION TIME	**DETECTION LIMIT**
COMMERCIAL ELISA KIT	+24 hr	1.6 ng/ml
2D BEAD BASED	+2 hr	50 ng/ml
IN-GEL IMMUNO-ASSAY	**3 hr**	**0.45 ng/ml**

Since managing only 5 particles at a time is extremely difficult, especially during washing steps, it would be interesting to implement the assay with 5 particles inside a microfluidic chip. This would allow to block the microparticles, to speed up all the incubation and washing steps and to use a very small sample volume.

4.4 Conclusions

In this chapter, we focused on the development and optimization of an in-gel sandwich assay on human-IgG. The cleavable hydrogel microparticles, synthesized and characterized as explained in chapters 2 and 3, demonstrated a high sensitivity, specificity and selectivity for the hIgG and therefore can be used directly in complex fluids without any purification. The in-gel immuno-assay was optimized in terms of primary antibody (0.1 pmol/part) and reporter (1nM) concentrations and the system was tested in buffer, human serum and synthetic urine, showing a limit of detection in the picomolar range. Moreover, studies about selectivity and specificity of the assay demonstrated that the system detects efficiently hIgG, even in presence of high concentrations of interfering molecules due to the anti-fouling properties of PEG and to the great porosity of the network. Since the chemical properties of the system can be easily tuned and optimized post synthesis, the cleavable hydrogel microparticles could be an ideal platform for the detection of a great variety of molecules such as proteins, antibodies related to pathologies, pollutants or toxic small molecules like dioxin.

4.5 References

1. Langer, R. & Tirrell, D. A. Designing materials for biology and medicine. *Nature* vol. 428 487–492 (2004).
2. Rubina, A. Y., Kolchinsky, A., Makarov, A. A. & Zasedatelev, A. S. Why 3-D? Gel-based microarrays in proteomics. *Proteomics* **8**, 817–831 (2008).
3. Helgeson, M. E., Chapin, S. C. & Doyle, P. S. Hydrogel microparticles from lithographic processes: Novel materials for fundamental and applied colloid science. *Current Opinion in Colloid and Interface Science* vol. 16 106–117 (2011).
4. Peppas, N. A., Keys, K. B., Torres-Lugo, M. & Lowman, A. M. Poly(ethylene glycol)-containing hydrogels in drug delivery. *J. Control. Release* **62**, 81–87 (1999).
5. Peppas, N. A., Hilt, J. Z., Khademhosseini, A. & Langer, R. Hydrogels in Biology and Medicine: From Molecular Principles to Bionanotechnology. *Adv. Mater.* **18**, 1345–1360 (2006).
6. Lee, K. Y. & Mooney, D. J. Hydrogels for Tissue Engineering. *Chem. Rev.* **101**, 1869–1880 (2001).
7. Nguyen, K. T. & West, J. L. Photopolymerizable hydrogels for tissue engineering applications. *Biomaterials* **23**, 4307–4314 (2002).

8. Slaughter, B. V., Khurshid, S. S., Fisher, O. Z., Khademhosseini, A. & Peppas, N. A. Hydrogels in Regenerative Medicine. *Adv. Mater.* **21**, 3307–3329 (2009).

9. Hoffman, A. S. Hydrogels for biomedical applications. *Advanced Drug Delivery Reviews* vol. 64 18–23 (2012).

10. Causa, F., Aliberti, A., Cusano, A. M., Battista, E. & Netti, P. A. Supramolecular spectrally encoded microgels with double strand probes for absolute and direct miRNA fluorescence detection at high sensitivity. *J. Am. Chem. Soc.* **137**, 1758–1761 (2015).

11. Pregibon, D. C. & Doyle, P. S. Optimization of Encoded Hydrogel Particles for Nucleic Acid Quantification. *Anal. Chem.* **81**, 4873–4881 (2009).

12. Chen, L. *et al.* Gel-pad microarrays templated by patterned porous silicon for dual-mode detection of proteins. *Lab Chip* **9**, 756–760 (2009).

13. Appleyard, D. C., Chapin, S. C., Srinivas, R. L. & Doyle, P. S. Bar-coded hydrogel microparticles for protein detection: Synthesis, assay and scanning. *Nat. Protoc.* **6**, 1761–1774 (2011).

14. Shohatee, D., Keifer, J., Schimmel, N., Mohanty, S. & Ghosh, G. Hydrogel-based suspension array for biomarker detection using horseradish peroxidase-mediated silver precipitation. *Anal. Chim. Acta* **999**, 132–138 (2018).

15. Battista, E., Causa, F. & Netti, P. Bioengineering Microgels and Hydrogel Microparticles for Sensing Biomolecular Targets. *Gels* **3**, 20 (2017).

16. Duan, K., Ghosh, G. & Lo, J. F. Optimizing Multiplexed Detections of Diabetes Antibodies via Quantitative Microfluidic Droplet Array. *Small* **13**, 1–8 (2017).

17. Al-Ameen, M. A., Li, J., Beer, D. G. & Ghosh, G. Sensitive, quantitative, and high-throughput detection of angiogenic markers using shape-coded hydrogel microparticles. *Analyst* **140**, 4530–4539 (2015).

18. Yu, X. *et al.* μFBI: A Microfluidic Bead-Based Immunoassay for Multiplexed Detection of Proteins from a μL Sample Volume. *PLoS One* **5**, e13125 (2010).

19. Buenger, D., Topuz, F. & Groll, J. Hydrogels in sensing applications. *Progress in Polymer Science* (2012) doi:10.1016/j.progpolymsci.2012.09.001.

20. Al-Ameen, M. A. & Ghosh, G. Sensitive quantification of vascular endothelial growth factor (VEGF) using porosity induced hydrogel microspheres. *Biosens. Bioelectron.* **49**, 105–110 (2013).

21. Appleyard, D. C., Chapin, S. C. & Doyle, P. S. Multiplexed Protein Quantification with Barcoded Hydrogel Microparticles. *Anal. Chem.* **83**, 193–199 (2011).

22. Moorthy, J., Burgess, R., Yethiraj, A. & Beebe, D. Microfluidic Based Platform for Characterization of Protein Interactions in Hydrogel Nanoenvironments. *Anal. Chem.* **79**, 5322–5327 (2007).

23. Chapin, S. C., Pregibon, D. C. & Doyle, P. S. High-throughput flow alignment of barcoded hydrogel microparticles. *Lab Chip* **9**, 3100–3109 (2009).

24. Kim, J., Heo, J. & Crooks, R. M. Hybridization of DNA to Bead-Immobilized Probes Confined within a Microfluidic Channel. *Langmuir* **22**, 10130–10134 (2006).

25. Kawaguchi, H. Functional polymer microspheres. *Progress in Polymer Science (Oxford)* vol. 25 1171–1210 (2000).

26. Chou, J. *et al.* Porous bead-based diagnostic platforms: Bridging the gaps in healthcare. *Sensors (Switzerland)* **12**, 15467–15499 (2012).

27. Padmavathi, N. C. & Chatterji, P. R. Structural characteristics and swelling behavior of poly(ethylene glycol) diacrylate hydrogels. *Macromolecules* **29**, 1976–1979 (1996).

28. Hutanu, D. Recent Applications of Polyethylene Glycols (PEGs) and PEG Derivatives. *Mod. Chem. Appl.* **02**, 2–7 (2014).

29. Della Ventura, B. *et al.* Biosensor for Point-of-Care Analysis of Immunoglobulins in Urine by Metal Enhanced Fluorescence from Gold Nanoparticles. *ACS Appl. Mater. Interfaces* **11**, 3753–3762 (2019).

30. Lacharme, F., Vandevyver, C. & Gijs, M. A. M. Magnetic beads retention device for sandwich immunoassay: Comparison of off-chip and on-chip antibody incubation. *Microfluid. Nanofluidics* **7**, 479–487 (2009).

5. Development and Application of In-gel Competitive Assay

5.1 Introduction

Dioxin-like compounds (DLCs) have been classified as persistent organic pollutants (POPs) due to their highly dangerous effects on human, including increased cancer risks, reproductive and endocrine defects, accumulation and biomagnification in the food chain and environment[1]. The most toxic and common congener belonging to the DLCs class is 2,3,7,8-tetrachlorodibenzo-para-dioxin (TCDD), commonly referred to as dioxin. The exposure to TCDD (chemical structure in figure 5.1) can cause several pathologies such as liver diseases, cancer, diabetes, hepatocellular carcinoma and metabolic syndrome (MetS)[2,3].

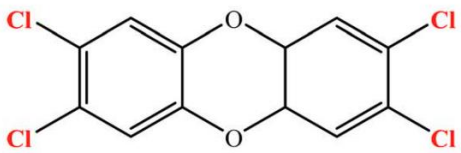

Figure 5.1: Chemical structure of 2,3,7,8-tetrachlorodibenzo-para-dioxin (TCDD). This compound contains two benzene rings linked to two oxygen atoms and includes four chlorine atom substitutions in the 2, 3, 7 and 8 positions.

The maximum values of tolerable intake, quantified as TCDD toxic equivalents (TEQ), are in the range between 1 and 4 pg per kg of body weight, and the maximum amount of dioxins accepted in food lies in the picogram range[4]. In accordance with these levels, the need to detect and quantify dioxins with high sensitivity and specificity, especially in human serum where the concentration is very low, has been the driving force for the development of increasingly sensitive analytical methods[5]. A combination of bioanalytical detection methods provides reliable systems to detect DLCs in environmental samples[7,8]. The chemical analytical methods are mostly based on gas chromatography (GC)[9], while the principal biological techniques are based on *in vivo* bioassays[10,11], biomarkers detection[12], cell-based *in vitro* bioassays[13] and protein binding assays[14]. In particular, high-resolution gas chromatography/mass spectroscopy (HR-GC/MS) and cell-based biochemical

assay CALUX (chemical-activated luciferase expression)[15] represented the gold standard techniques for dioxin detection in serum. The CALUX assay provides an approximation of the total TEQ concentration (dioxin toxic equivalent) but it cannot provide an individual measurement of dioxin congeners in a sample. In fact, CALUX is generally used for a qualitative screening and characterized by low specificity. It cannot discriminate between other similar compounds with arylic groups contained in the sample[16]. Moreover, this test results an expansive and extremely time-consuming technique, which requires the culture and reaction of genetically modified mammalian cells exposed to dioxin-like chemicals in a blood sample. On the contrary, the HR-GC/MS analysis is widely used for measuring individual congeners and total dioxin concentration (TEQ) with high specificity. This chromatographic technique is however very expansive and, in addition, tens of millilitres of blood are needed to perform the dioxin analysisNevertheless, both CALUX and HR-GC/MS require extremely time-consuming extraction and purification of dioxin from human serum via liquid chromatography and organic solvent extractions. Many efforts have been made to reduce the analysis costs[21,22], including developing a radioimmunoassay[23,24] (RIA) and an enzyme-linked immunosorbent test (ELISA) using mouse monoclonal antibodies[25]. These tests require fewer steps for sample purification, though the sensitivity is generally two or three orders of magnitude lower than the HR-GC/MS technique.

In this scientific scenario, the realization of hydrogel-based biosensors, suitable for the specific, selective and direct quantification of the molecule of interest, represents a valid alternative to the current dioxin detection techniques. Moreover hydrogel-based biosensors are characterized by high chemical flexibility, small dimensions and low production costs. The development of a bead-based assay using encoded hydrogel microparticles represent a promising platform because of its high multiplex capacity and its superior sensitivity and dynamic range compared to the enzyme-linked immunosorbent assay (ELISA). Because of the great quantity of validated antibody pairs available, the sandwich ELISAs are the most common implementation of the assay. Considering the small size of the dioxin, this molecule cannot be detected through a sandwich assay and, therefore a competitive scheme has been adopted (Figure 5.2). In this chapter, we present the development of an in-gel competitive assay for the detection of the TCDD. In particular, our detection system is based on finely engineered cleavable hydrogel microparticles, synthesized and characterized as already discussed in chapters 2 and 3. The hydrogel microparticles functionalized with the anti-dioxin antibody are incubated with a pre-mixed solution of target dioxin and a fluorescent competitor. The assay has been optimized to provide a simple, fast fluorescent turn-off sensor, for highly sensitive and specific recognition of few picograms of dioxin.

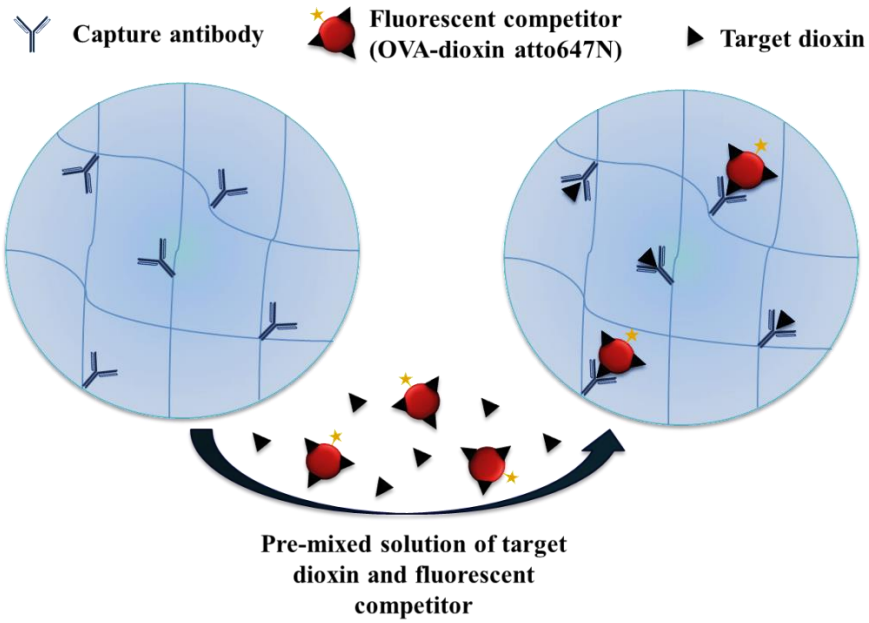

Figure 5.2: Schematic illustration of the in-gel dioxin competitive assay. The hydrogel microparticles functionalized with the anti-dioxin antibody are incubated with a pre-mixed solution of target dioxin and fluorescent competitor. The dioxin, which presents a greater affinity with the capture antibody, compete with a fluorescent antigen for the available sites. The fluorescence signal emitted is quantified and compared with the control signal in absence of dioxin to evaluate the percentual decrement, proportional to the amount of analyte bound.

5.2 Materials and Methods

All the hydrogel microparticles used in the experimental part of this chapter were synthesized, optimized and characterized as already described in the chapters 2 and 3.

5.2.1 Specific capture antibody and fluorescent competitor identification

The anti-dioxin capture antibody used for the detection is specific for recognizing TCDD (2,3,7,8 Tetrachlorodibenzo-p-dioxin), since this compound represents the most common and dangerous dioxin congener. The figure 5.3 shows the cross-reactivity of the anti-dioxin antibody (DBA Italia) against various dioxin congeners.

Dioxins	Compounds	Crossreactivity (%)
PCDDs	2,3,7-TriCDD	100
	2,3,7,8-TeCDD	240
	1,2,3,7,8-PeCDD	25
	1,2,3,4,7,8-HxCDD	0.3
	1,2,3,6,7,8-HxCDD	<0.1
	1,2,3,7,8,9-HxCDD	<0.1
	1,2,3,4,6,7,8-HpCDD	<0.1
	1,2,3,4,6,7,8,9-OCDD	0.1
PCDFs	2,3,7,8-TeCDF	15
	1,2,3,7,8-PeCDF	1
	2,3,4,7,8-PeCDF	39
	1,2,3,4,7,8-HxCDF	0.7
	1,2,3,6,7,8-HxCDF	0.3
	1,2,3,7,8,9-HxCDF	<0.1
	2,3,4,6,7,8-HxCDF	0.1
	1,2,3,4,6,7,8-HpCDF	<0.1
	1,2,3,4,7,8,9-HpCDF	<0.1
	1,2,3,4,6,7,8,9-OCDF	<0.1
Co-PCB	3,4,4',5-TeCB (#81)	2
	3,3',4,4'-TeCB (#77)	3
	3,3',4,4',5-PeCB (#126)	0.3
	3,3',4,4',5,5'-HxCB (#169)	<0.1
	2',3,4,4',5-PeCB (#123)	<0.1
	2,3',4,4',5-PeCB (#118)	0.3
	2,3,3',4,4'-PeCB (#105)	0.5
	2,3,4,4',5-PeCB (#114)	0.1
	2,3',4,4',5,5'-HxCB (#167)	<0.1
	2,3,3',4,4',5-HxCB (#156)	0.1
	2,3,3',4,4',5'-HxCB (#157)	<0.1
	2,3,3',4,4',5,5'-HpCB (#189)	<0.1

Figure 5.3: Cross-reactivity of the anti-dioxin antibody against the most common dioxin congeners. The one in red is the molecule of interest, which presents the higher crossreactivity.

For what concern the dioxin competitor (fluorescent antigen), a large dioxin-conjugated protein carrier (ovalbumin) was used as dioxin competitor (Tecna Srl). This carrier was labelled with a fluorophore exploiting the amino groups of the ovalbumin. In detail, reaction was carried out with 0.55 mg of OVA-dioxin and 30µm of ATTO647N-N-Hydroxysuccinimide for 30 min at room temperature. After the reaction, the conjugate (OVA-dioxin ATTO647N) was dialysed and characterized through a spectrophotometric measurement to calculate its concentration and degree of functionalization.

5.2.2 Capture antibody optimization

The optimal antibody concentration was evaluated by analysing the capacity of the antibody to recognize the fluorescent antigen "OVA-dioxin ATTO647N" at different concentrations, through a fluorescence analysis. In detail, 10 cleaved hydrogel particles per sample were functionalized with 0.1 and 1 pmol per particle and incubated (2h, 37°C) with 6 different concentrations of fluorescent antigen (OVA-dioxin ATTO647N) by exploring a range between

0 and 800nM. After the incubation time and subsequent washing, images of the particles were acquired using a confocal microscope (CLSM Leica SP5, Objective 20x DRY, scan speed of 400 Hz, excitation wavelength 633, emission wavelength 648-710nm) to evaluate the relative fluorescence intensities. The fluorescence signal indicates the binding between the immobilized anti-dioxin antibody in microparticles and fluorescent OVA-dioxin. The images were analysed with ImageJ software and the error is represented by standard deviation.

5.2.3 Fluorescent competitor optimization

The competitor concentration, represented by the fluorescent antigen, was optimized by trying to achieve both a good fluorescence intensity in the absence of dioxin and a good sensitivity, in terms of decrease in fluorescence at low dioxin concentrations (picomolar range). The optimal competitor concentration was evaluated by exploring different dioxin/competitor ratios (1:20; 1:200; 1:400; 1:800 corresponding respectively to 5, 50, 100, 200nM OVA-dioxin atto647N), with a dioxin fixed concentration (250pM). In detail, 10 cleaved hydrogel particles per sample were functionalized with 0.1 pmol per particle and incubated (2h, 37°C) with 4 premixed solutions of dioxin and fluorescent competitor in different ratios, as previously mentioned. For each sample, a control without dioxin was prepared in order to evaluate the zero-fluorescence signal and its decrease in presence of dioxin. After the incubation time and subsequent washing, all the samples were imaged (CLSM Leica SP5, Objective 20x DRY, scan speed of 400 Hz, excitation wavelength 633, emission wavelength 648-710nm) and analysed with ImageJ software. The error is represented by standard deviation.

5.2.4 In-gel displacement assay: Calibration in buffer

The hydrogel microparticles calibration in buffer was performed to obtain a dose-response binding curve with different dioxin concentrations in a range between 0 and 500pM. In particular, 10 cleaved microparticles, functionalized with anti-dioxin antibody (0.1 pmol per particle) were incubated (2h at 37°C) with 5 different pre-mixed solutions composed by i) fluorescent antigen (OVA-dioxin ATTO647N) at a fixed concentration of 5 nM and ii) 4 different dioxin concentrations (0, 25, 100, 250, 500 pM). After the incubation time and subsequent washes, the particles were visualized under a confocal microscope (CLSM Leica SP5, Objective 20x DRY, scan speed of 400 Hz, excitation wavelength 633, emission wavelength 648-710nm) to evaluate the relative fluorescence intensities, indicative of the competitive binding between dioxin and OVA-dioxin with the anti-dioxin antibody. All images were analysed with ImageJ and the error is represented by standard deviation. The fluorescence

emission of blank functionalized microparticles have been acquired and its value has been subtracted from the signal intensity of each point. The statistical analysis on experimental data was performed with t-student tests using GraphPad Prism 8. The limit of detection (LOD) was evaluated on the linear part of the calibration curve as follows:

$$LOD = {}^{3\sigma_0}/_{S}$$

Where σ_0 represents the standard deviation on the signal of the sample with no target (zero) and S is the slope of the linear part of the calibration curve.

5.2.5 In-gel displacement assay in serum

The performance of the hydrogel microparticles-based biosensors was evaluated also in human blood extracts. In particular, the dioxin quantification tests were performed in diluted serum samples, in which 4 different concentrations of a mixture of congeners belonging to the dioxin class were added. A 5-fold dilution of the 4 samples was executed to obtain final concentrations of dioxins in a range between 0.062-62nM. These samples were incubated with 10 particles (functionalized with 0.1 pmol of antibody per particle) and with OVA-dioxin ATTO647N at a fixed concentration of 5nM, 2h at 37°C. After several washes, the particles were visualized (CLSM Leica SP5, Objective 20x DRY, scan speed of 400 Hz, excitation wavelength 633, emission wavelength 648-710nm) to evaluate the relative fluorescence intensities. The fluorescence emission of blank functionalized microparticles have been acquired and its value has been subtracted from the signal intensity of each point. All images were analysed with ImageJ and the error is represented by standard deviation.

5.3 Results and discussion

5.3.1 Capture antibody and competitor optimization

After demonstrating the generation of aldehydes groups after cleavage reactions and the accessibility of a ternary antibody complex (~ 45 nm) within the porous network of hydrogel microparticles (chapter 3), we have developed a novel, sensitive in-gel immunoassay. First, the anti-dioxin antibody concentration has been optimized. The antibody concentration was evaluated by analysing the capacity of the antibody to recognize a fluorescent competitor. In order to limit the interference of a fluorophore conjugated on a small molecule, a direct labelling

of the dioxin was avoided. Thus, a large dioxin-conjugated protein carrier (ovalbumin) was used as dioxin competitor. This carrier was labelled with a fluorophore exploiting the amino groups of the ovalbumin. Basing on the moles of aldehydes calculated in chapter 3, two concentrations of anti-dioxin antibody for the microparticle conjugation step were studied (0.1 and 1 pmol per particle). The response of these differently conjugated particles was assessed after their incubation with the fluorescent competitor "OVA-dioxin ATTO647N" at different concentrations in a range between 0 and 800pM. After washing the microparticles to remove the unbounded OVA-dioxin ATTO647N, the fluorescence from the droplets were evaluated. As shown in figure 5.4, the hydrogel microparticles with both anti-dioxin antibody functionalizations reach comparable intensity levels (with a maximum of about 1500 a.u.), although the particles conjugated with 0.1 pmol of antibody present a higher homogeneity in florescence signal, showing a lower standard deviation, especially at high concentrations of OVA-dioxin ATTO647N. Therefore, the conjugation with 0.1 pmol per particle of anti-dioxin antibody represents the selected strategy for the following tests.

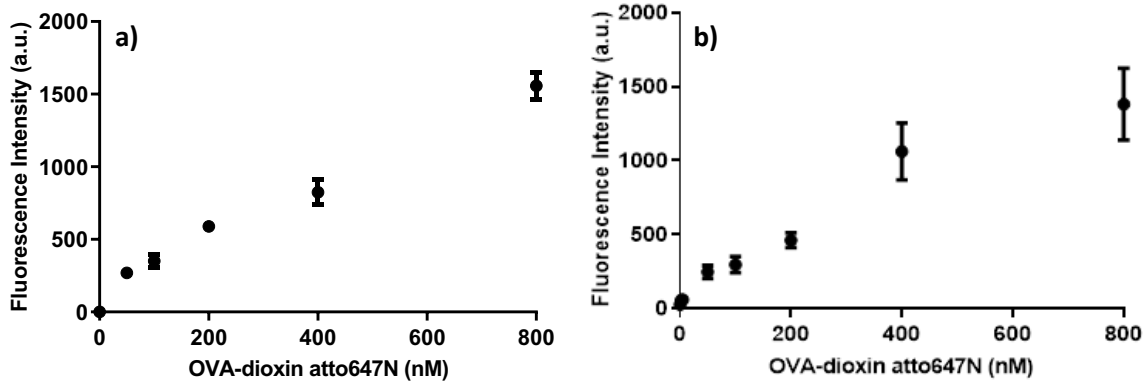

Figure 5.4: Fluorescence signal intensity of OVA-dioxin ATTO647N captured by functionalized hydrogel microparticles with 0.1pmol /part (a) and 1 pmol/part (b) of anti-dioxin antibody.

Subsequently, the functionalized hydrogel microparticles (0.1pmol/part anti-dioxin antibody) were used to set the ideal fluorescent competitor concentration. The optimization was performed trying to achieve both a good fluorescence intensity in absence of dioxin and a good sensitivity in the picomolar range. The optimal competitor concentration was evaluated by exploring different dioxin/competitor ratios (1:20; 1:200; 1:400; 1:800 corresponding respectively to 5, 50, 100, 200 nM OVA-dioxin atto647N), with a dioxin fixed concentration (250pM). For each sample, a control without dioxin was prepared in order to evaluate the zero-

fluorescence signal and its decrease in presence of dioxin. Figure 5.5 shows the decrease in fluorescence intensity due to the presence of a fixed dioxin concentration for every ratio with the fluorescent OVA-dioxin. The maximum difference between the control and the dioxin-containing sample (250pM), and therefore the greater sensitivity of the system to the presence of picomolar concentration of dioxin, was obtained with the lowest competitor-dioxin ratio (1/20), corresponding to a 5nM OVA-dioxinATTO647N concentration. Therefore, this concentration has been selected to perform the final competitive assay.

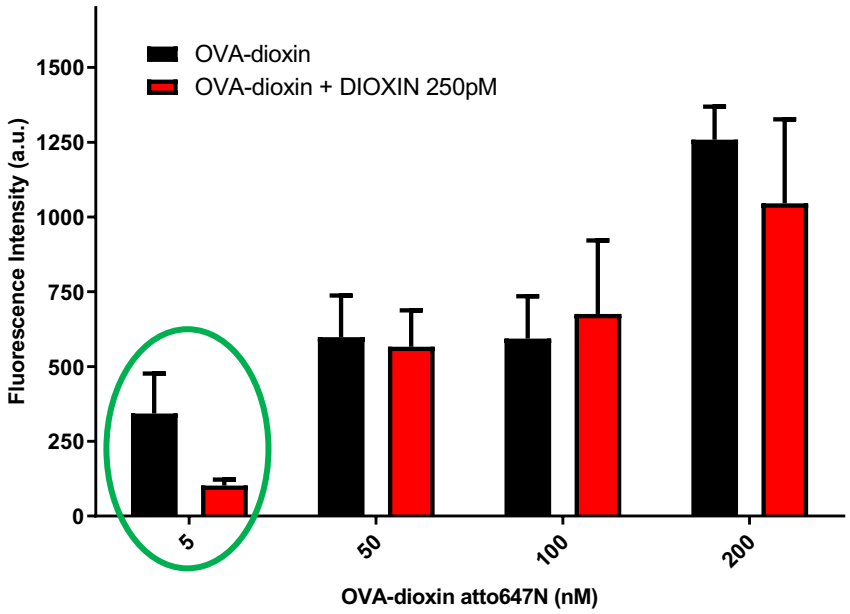

Figure 5.5: Difference of fluorescence signal intensity in absence and in presence of a 250pM dioxin solution, evaluated on 4 different competitor-dioxin ratios (1:20; 1:200; 1:400; 1:800). The green-circled ratio represents the most sensitive solution.

5.3.2 In-gel displacement assay: Calibration in buffer

In order to calibrate the system and to evaluate limit of detection, a competitive in-gel assay on TCDD in buffer was performed. In details, 10 anti-dioxin-conjugated-microparticles were incubated with 5 different pre-mixed solutions composed by free dioxin at variable concentrations (0, 25, 100, 250, 500 pM), while the concentration of the competitor OVA-dioxin ATTO647N is fixed at 5 nM. The fluorescence emission of the labelled competitor versus the target dioxin concentration is plotted (Figure 5.6) showing a specific competition dose-response curve where fluorescent signal decreased with increase in dioxin concentration. The higher the dioxin concentration the less fluorescent competitor is recognized by anti-dioxin

antibodies within the hydrogel microparticles, resulting in a signal decrement. At the highest dioxin concentration explored (500 pM), a decrease of about 50% of the fluorescence signal can be observed. This value can be set as a threshold for a rapid screening of the level of dioxin in a sample.

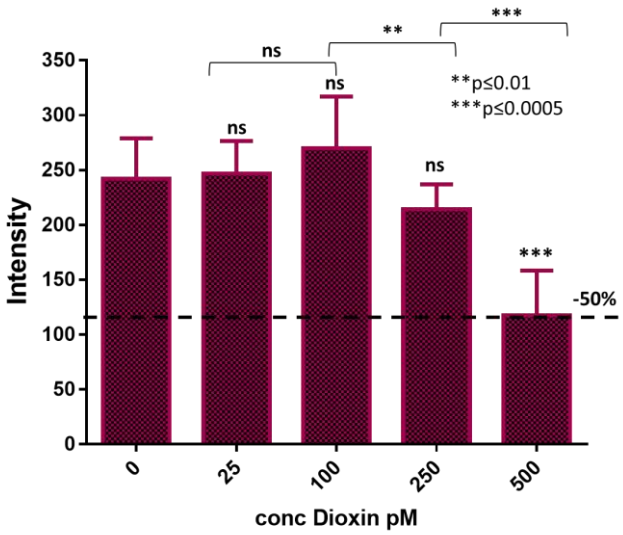

Figure 5.6: Experimental data of competitive assay on TCDD performed on hydrogel microparticles in a range between 0 and 500pM. At the higher concentration tested, the decrement in fluorescence signal is about 50% (on-off threshold).

The CV% inter-assay was calculated by comparing the results between multiple experiments and its value results to be 7%. In comparison with the actual gold standard techniques for the detection of dioxin in extracted and purified samples, our in-gel competitive assay shows a medium sensitivity but a lower cost and a shorter detection time (Table 5.1). This result paves the way for the possible use of in-gel competitive assay as an inexpensive and rapid screening of biological or environmental samples.

Table 5.1: Performances comparison in terms of detection time, limit of detection and cost between the gold standard for TCDD detection (HR-GC/MS[26,27] and CALUX[15]) and our hydrogel microparticles

	TIME	**TCDD LOD**	**COST**
CALUX	+24 hr	0.5 pM	Medium-high
HR-GC/MS	+2 hr	1nM	Very high
IN-GEL IMMUNO-ASSAY	**2h**	**500pM**	**Low**

5.3.3 In-gel displacement assay in serum

In order to avoid long and expansive steps of dioxin extraction and purification from human serum samples, studies about the in-gel recognition of TCDD in whole serum were carried out. Serum samples had been spiked with internal standard solution containing the dioxin at different concentrations. These prepared samples were diluted 5 times and incubated with the antibody-conjugated microparticles and the fluorescent competitor (5nM). As figure 5.7 shows, no dose-dependent signal variation is observed at different dioxin concentration in serum, and the fluorescent intensity results similar for all the dioxin concentration explored. Moreover, the signal is extremely low, indicating a lack of recognition between the anti-dioxin antibody and the fluorescent antigen, even in presence of a very low concentration of dioxin (zero signal).

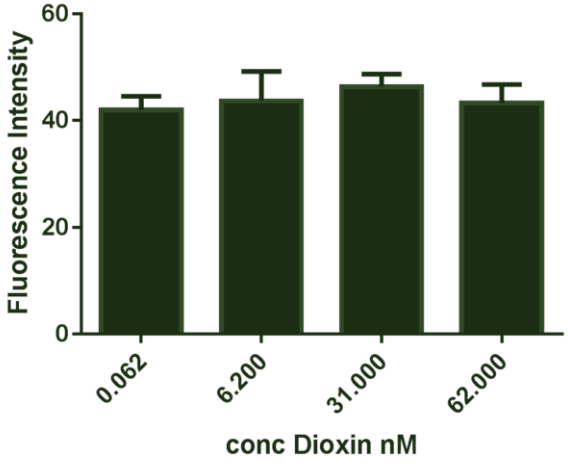

Figure 5.7: Experimental data of in-gel competitive assay on TCDD performed in 1:5 diluted human serum in a target concentration range between 0.062 and 62nM.

These data suggested the potential interference of the lipid part contained in human serum, which act as a complexing agent of dioxin molecules. In fact, it is known that in plasma, dioxins and furans are complexed with proteins and lipoproteins due to their low water solubility, which make the analyte unavailable for recognition. Therefore, we tried to dilute the serum up to 50 folds in order to limit the interactions between dioxin and lipids contained in serum. As shown in figure 5.8, the dilutions of 10, 25 and 50 times did not improve the performance.

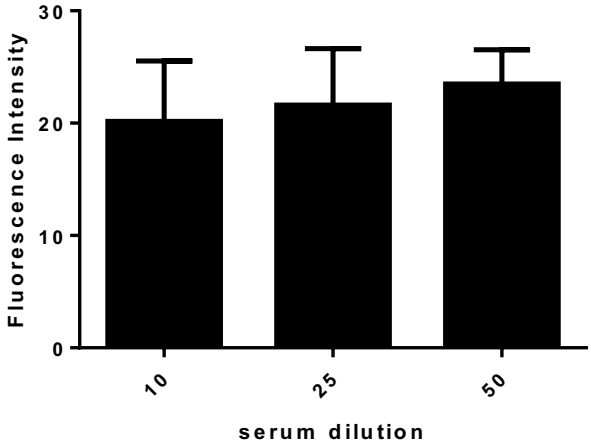

Figure 5.8: Experimental data of in-gel competitive assay on a 62nM TCDD sample performed in human serum at different dilutions (10, 25, 50).

In view of these experimental results, the sample preparation results to be a crucial step to make dioxin available for the detection. In order to eliminate the potential interfering molecules and improve the sensitivity of the assay, it will be necessary to perform steps of dioxins extraction and purification from biological fluids, with a procedure comparable to that used for the CALUX biological test.

5.4 Conclusions

In this work, we focused on the development and optimization of an in-gel competitive assay on TCDD, one of the most common and dangerous congener of the dioxins class. The cleavable hydrogel microparticles, synthesized and characterized as explained in chapters 2 and 3, demonstrated a good sensitivity (around 500pM) for the dioxin detection and therefore can be used as a fast screening with an on-off threshold in extracted and purified dioxin samples from human serum. The in-gel competitive assay was optimized in terms of capture antibody (0.1 pmol/part) and fluorescent competitor (5nM) concentrations and the system was tested in buffer and diluted human serum. Results in buffer showed a fluorescence signal inhibition of about 50% (with a good accuracy CV 7%) for a dioxin concentration of 500pM. While in serum samples diluted up to 50 folds, data show a very low fluorescence signal, even in absence of dioxin. This result suggests the lack of recognition between the capture antibody and the fluorescent competitor that can be addressed to a strong interaction between lipids in serum and dioxins on the ovalbumin surface. Therefore, steps of dioxins extraction and purification from

biological fluids become essential to perform the competitive assay. For this purpose, further studies regarding the compatibility of our detection system with organic solvents typically used for the extraction (DMSO and/or dioxane) will be carried out.

5.5 References

1. Health Risks from Dioxin and Related Compounds: Evaluation of the EPA Reassessment - National Research Council, Division on Earth and Life Studies, Board on Environmental Studies and Toxicology, Committee on EPA's Exposure and Human Health Reassessment of TCDD and Related Compounds (2006).

2. Hahn, M. E. Biomarkers and bioassays for detecting dioxin-like compounds in the marine environment. *Sci. Total Environ.* **289**, 49–69 (2002).

3. Stegeman, J. J., Kloepper-Sams, P. J. & Farrington, J. W. Monooxygenase induction and chlorobiphenyls in the deep-sea fish coryphaenoides armatus. *Science (80-.).* **231**, 1287–1289 (1986).

4. Van Leeuwen, F. X. R. *et al.* Dioxins: WHO's tolerable daily intake (TDI) revisited. *Chemosphere* **40**, 1095–1101 (2000).

5. Tavakoly Sany, S. B. *et al.* An overview of detection techniques for monitoring dioxin-like compounds: Latest technique trends and their applications. *RSC Advances* vol. 6 55415–55429 (2016).

6. Behnisch, P. A., Hosoe, K. & Sakai, S. I. Bioanalytical screening methods for dioxins and dioxin-like compounds- A review of bioassay/biomarker technology. *Environ. Int.* **27**, 413–439 (2001).

7. Muir, D. C. G., Norstrom, R. J. & Simon, M. Organochlorine Contaminants in Arctic Marine Food Chains: Accumulation of Specific Polychlorinated Biphenyls and Chlordane-Related Compounds. *Environ. Sci. Technol.* **22**, 1071–1079 (1988).

8. Wania, F. & Daly, G. L. Estimating the contribution of degradation in air and deposition to the deep sea to the global loss of PCBs. *Atmos. Environ.* **36**, 5581–5593 (2002).

9. Loos, R., Tavazzi, S., Paracchini, B., Canuti, E. & Weissteiner, C. Analysis of polar organic contaminants in surface water of the northern Adriatic Sea by solid-phase extraction followed by ultrahigh-pressure liquid chromatography-QTRAP® MS using a hybrid triple-quadrupole linear ion trap instrument. in *Analytical and Bioanalytical Chemistry* vol. 405 5875–5885 (2013).

10. Tavakoly Sany, S. B. *et al.* Dioxin risk assessment: mechanisms of action and possible toxicity in human health. *Environ. Sci. Pollut. Res.* **22**, 19434–19450 (2015).

11. Ten Tusscher, G. W. *et al.* Neurodevelopmental retardation, as assessed clinically and with magnetoencephalography and electroencephalography, associated with perinatal dioxin exposure. *Sci. Total Environ.* **491**–**492**, 235–239 (2014).

12. Van den Berg, M. *et al.* The 2005 World Health Organization reevaluation of human and mammalian toxic equivalency factors for dioxins and dioxin-like compounds. *Toxicological Sciences* vol. 93 223–241 (2006).

13. Eichbaum, K. *et al.* In vitro bioassays for detecting dioxin-like activity - Application potentials and limits of detection, a review. *Science of the Total Environment* vol. 487 37–48 (2014).

14. Wang, B. J. *et al.* Establishment of a cell-free bioassay for detecting dioxin-like compounds. *Toxicol. Mech. Methods* **23**, 464–470 (2013).

15. Murk, A. J. *et al.* Chemical-activated luciferase gene expression (CALUX): A novel in vitro bioassay for Ah receptor active compounds in sediments and pore water. *Fundam. Appl. Toxicol.* **33**, 149–160 (1996).

16. Otarola, G., Castillo, H. & Marcellini, S. Aryl hydrocarbon receptor-based bioassays for dioxin detection: Thinking outside the box. *J. Appl. Toxicol.* **38**, 437–449 (2018).

17. Carabias-Martínez, R., Rodríguez-Gonzalo, E., Revilla-Ruiz, P. & Hernández-Méndez, J. Pressurized liquid extraction in the analysis of food and biological samples. *Journal of Chromatography A* vol. 1089 1–17 (2005).

18. Focant, J. F., Pirard, C. & De Pauw, E. Automated sample preparation-fractionation for the measurement of dioxins and related compounds in biological matrices: A review. *Talanta* vol. 63 1101–1113 (2004).

19. Dimpe, K. M. & Nomngongo, P. N. Current sample preparation methodologies for analysis of emerging pollutants in different environmental matrices. *TrAC - Trends in Analytical Chemistry* vol. 82 199–207 (2016).

20. Hoff, R. B. & Pizzolato, T. M. Combining extraction and purification steps in sample preparation for environmental matrices: A review of matrix solid phase dispersion (MSPD) and pressurized liquid extraction (PLE) applications. *TrAC - Trends in Analytical Chemistry* vol. 109 83–96 (2018).

21. Kasai, A. *et al.* Fast-track DRESSA: A bioassay for fast, sensitive, and selective detection of halogenated and polycyclic aromatic hydrocarbons. *Anal. Biochem.* **337**, 84–88 (2005).

22. Patrizi, B., De Cumis, M. S., Viciani, S. & D'Amato, F. Dioxin and related compound detection: Perspectives for optical monitoring. *International Journal of Molecular Sciences* vol. 20 (2019).

23. Albro, P. W. *et al.* A radioimmunoassay for chlorinated dibenzo-p-dioxins. *Toxicol. Appl. Pharmacol.* **50**, 137–146 (1979).

24. Luster, M. I. *et al.* Production and characterization of antisera specific for chlorinated biphenyl species: Initiation of a radioimmunoassay for aroclors. *Toxicol. Appl. Pharmacol.* **50**, 147–155 (1979).

25. Stanker, L. H., Watkins, B., Rogers, N. & Vanderlaan, M. Monoclonal antibodies for dioxin: Antibody characterization and assay development. *Toxicology* **45**, 229–243 (1987).

26. Dioxin and Related Compounds: Special Volume in Honor of Otto Hutzinger Editors: Alaee, Mehran (2016).

27. Sánchez-Avila, J., Fernandez-Sanjuan, M., Vicente, J. & Lacorte, S. Development of a multi-residue method for the determination of organic micropollutants in water, sediment and mussels using gas chromatography-tandem mass spectrometry. *J. Chromatogr. A* **1218**, 6799–6811 (2011).

6. Hydrogel Microparticles in a Microfluidic Device for On-Chip Detection

6.1 Introduction

6.1.1 Microfluidic particles trapping techniques

In recent years, microfluidic systems have received great interest in many fields such as life science, tissue engineering, pharmacology and diagnostics[1–3]. By miniaturizing and integrating different functionalities, microfluidic systems provide the ability to perform laboratory operations on small scales (lab-on-a-chip), thus minimizing reagent consumption, processing times and costs. Applications of these microfluidic systems include biomolecules detection and profiling[4,5] bead-based immunoassays[6,7] and cells sorting and trapping[8–10]. Several microfluidic technologies for trapping microparticles or cells are widely studied in literature[11] and several strategies including hydrodynamic trapping[12,13], optical tweezers[14], dielectrophoresis[15], magnetic[16] and acoustic trapping[17] have been explored. Among them, simple hydrodynamic trapping is preferable for handling hydrogel beads, since all forces implied allow to manipulate soft particles whose diameter ranges from 80 µm to 200 µm, without any damage. In diagnostic field, the fine manipulation of hydrogel beads through microfluidic system can be very useful in order to enhance the reagent transport and turnover throughout the whole particle volume, enabling pg mL^{-1} protein detections with shortened assay time. Thus, microfluidic represents the ideal technique to reach this goal, allowing to create an array of hydrogel particles trapped in well-defined positions and enabling high-throughput and fast detections[18–20].

6.1.2 Microfluidic devices materials and fabrication techniques

Photolithography has been used as a major method for the fabrication of microfluidic devices, which involves exposure to light of selected regions of a substrate coated with photoresist[21] .

The most used and easy method, alternative to the time and cost consuming and complex photolithography facilities, to fabricate a microfluidic device are soft lithography techniques and in particular replica molding[22,23].

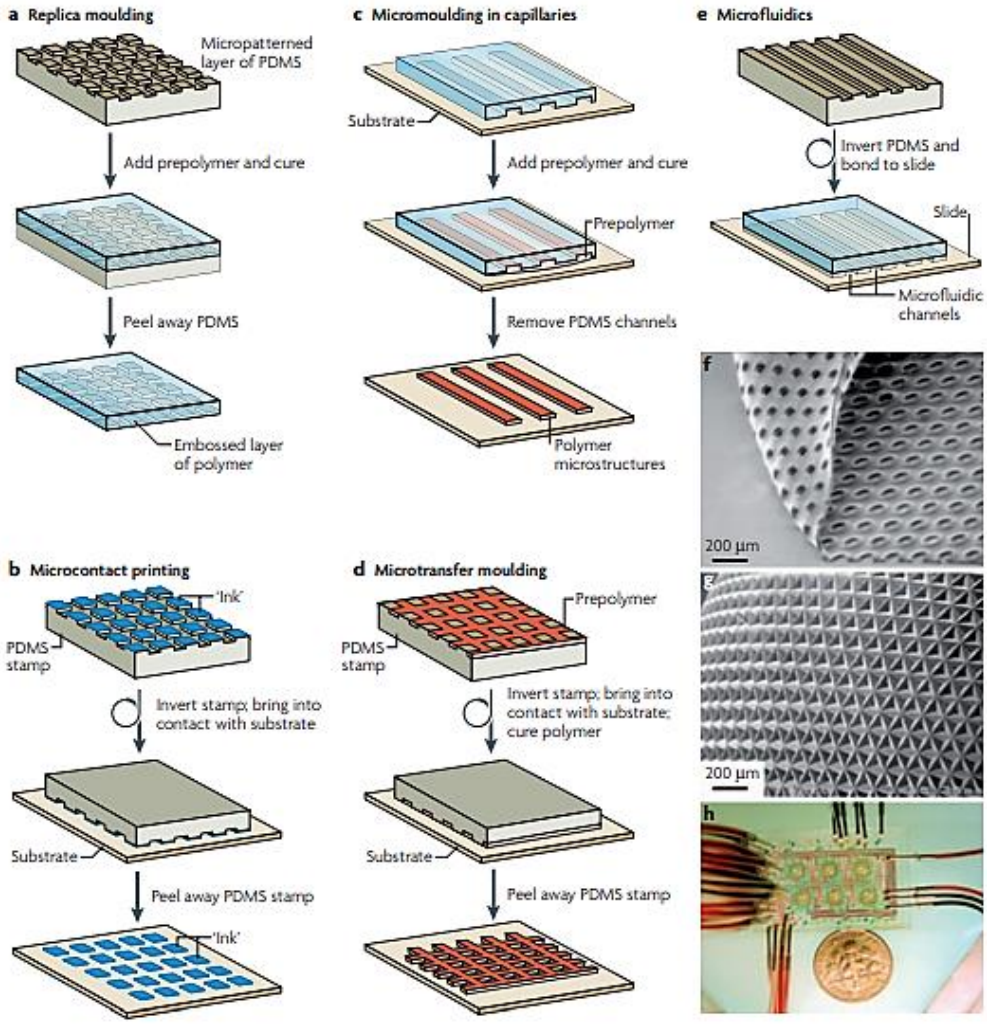

Figure 6.1 Schematic illustration of the principal techniques of soft lithography and their application. The key stages of each of the following techniques are shown a) replica moulding; b) microcontact printing; c) micro-moulding in capillaries; d) micro-transfer moulding; and e) microfluidics. f) A PDMS porous realized by replica moulding[24]. g) A curved layer of micropatterned polyurethane created by replica moulding on a bent micropatterned layer of PDMS[25]. h) A microfluidic chemostat for the growth and culture of microbial cultures[26]. [27]

Soft lithography is a technique to rapidly and easily fabricate and replicate a wide range of elastomeric materials. In particular, tiny patterns are created on the surface of a material using a "pattern-transfer element" or a stamp that has a three-dimensional structure moulded onto its surface. These pattern-transfer elements are always made from an elastomer since they deform under an applied force and get back to their shape when the force is released. In particular, replica micro-molding is a soft lithography method used to replicate micro-structured masters on polymers. The mold is usually fabricated by photolithography on a silicon wafer or with a micro-milling machine onto a rigid polymeric plate, commonly made of PMMA. The polymer

(agar, agarose, collagen, PDMS and other biocompatible polymers) is poured on the mold, cured, detached and bonded to a soft or rigid surface to create a functional microfluidic device.

Polymeric materials are gaining considerable attention as materials for the fabrication of microfluidic devices[28], especially in the biological detection field[17,29,30]. Most of them are easily replicable, biocompatible and have optical, thermal and electrical properties suitable for detection applications[31–33]. In particular PDMS has become the most commonly used elastomer in rapid prototyping of microfluidic devices because of its biocompatibility, inexpensiveness, chemical inertness, low toxicity and ease of manipulation. In fact, its fabrication procedure through casting and curing onto a mold results very simple and it can be strongly sealed to a wide variety of materials. Usually, the pre-polymer is cross-linked with the thermo-initiator in a 10:1 ratio in weight but this ratio can be modified in order to change the mechanical properties of the final product. Despite its qualities, PDMS presents some limitations including gas permeability (depending on the thickness) and hydrophobicity. In fact, the hydrophobic nature of PDMS can cause non-specific protein/hydrophobic analyte absorption on the internal channel surface[34]. Therefore, many surface treatment methods (such as oxygen plasma, or UV-irradiation[35] for PDMS have been reported in order to increase the wettability of the hydrophobic polymer surfaces. Recently, there has been growing interest in developing a very simple and effective method like the addition of wetting agents (like Silwet l-77) to PDMS mixture. Silwet is a non-ionic surfactant which reduces the PDMS hydrophobicity to avoid spontaneous backflow during the use of the device.

In this chapter we present the design, fabrication and testing of an innovative microfluidic device for hydrogel microparticles trapping for on-chip detection. The device is based on hydrodynamic trapping of microparticles and is realized via conventional replica micro-molding. The negative master is produced with the micro-milling machine on a PMMA plate and replicated in hydrophilic PDMS. The replica is bonded to a thin glass slide and connected to the flow with tubing. Several studies regarding the trapping efficiency have been performed, considering three different microfluidic trapping chamber geometries. Finally, the optimal design has been replicated several times to perform the hIgG capture on-chip and to optimize the washing volumes for the final sandwich assay.

6.2 Materials and Methods

6.2.1 Microfluidic device: design and realization

All the microfluidic devices realized and tested in this chapter were designed in 2D using Autocad and then transformed in 3-dimensionals files with Deskam. The microfluidic devices were made of Polydimethylsiloxane (PDSM) via conventional replica molding techniques. In particular, the CAM files were loaded on the micro-milling machine (Mini-mill/GX, Minitech Machinery Corporation; End mills 0.1-0.5mm TS-2-SR6, Performance Micro Tool) software, in order to obtain a negative mold of the device on a 1.2 mm thick Polymethylmethacrylate (PMMA) plate. The molds were cleaned with ethanol, sonicated and finally used to replicate the microfluidic chip. The replicas were realized by pouring a mixture of PDMS, in a 10:1 ratio with a thermo-initiator, and Silwet 0.8% (Silwet l-77, Momentive) onto the mold. Silwet is a non-ionic surfactant which reduces the PDMS hydrophobicity to avoid spontaneous backflow during the use of the device. The PDSM was cured in an oven at 90 ° C for 2 hours, detached from the master, punched, cleaned and bonded on a glass slide via oxygen plasma treatment for 1 min with consequent heat treatment in a stove at 90 ° C for 1 hour. The slides used for bonding present a high level of optical quality, even in fluorescence, an essential feature to ensure a high sensitivity of the assay inside the device. After bonding, the device was connected to the flow through pipes and fittings to carry out loading tests. The entire microfluidic chips production process, starting from the realization of the mold up to the final product, is shown in Figure 6.2.

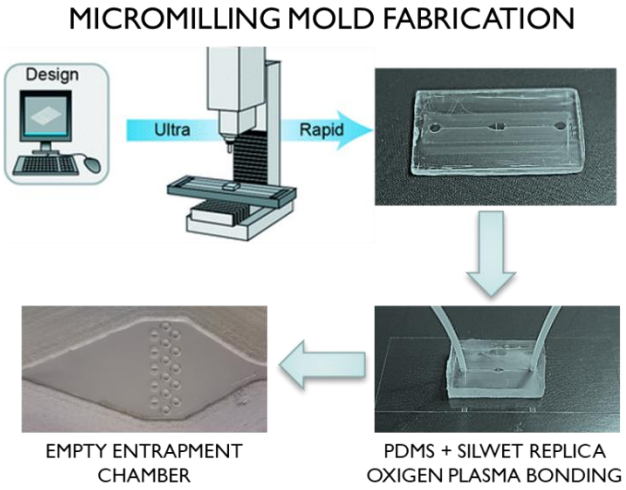

Figure 6.2: Schematic illustration of a microfluidic chip production process, which involves 4 phases: two-dimensional CAD drawing, micro-milling processing for the realization of the negative mold in PMMA, positive replication in hydrophilic PDMS of the device and finally its irreversible bonding on the slide through plasma and heat treatment.

6.2.2 Hydrogel microparticles trapping

In order to test the capability of the microfluidic devices to trap the hydrogel microparticles in well-defined positions, a highly diluted suspension of microparticles in buffer was injected into the chip through a syringe. The experiments were carried out pumping 100µL at a time and acquiring images of the trapped microparticles with an inverted microscope (IX 71 Olympus) equipped with a 10× objective. All the solutions injected into the device were filtered with a 0.45µm syringe filter in order to avoid the entrance of any dust, which can alter the functioning of the chip.

6.2.3 Target binding and washes optimization

The optimized device was loaded, as explained in the previous paragraph, with 5 functionalized microparticles (0.1 pmol/part monoclonal anti human IgG FC specific, Sigma Aldrich). Then, 100µL of a 1µM solution of labelled (atto647) human IgG (Sigma Aldrich) were injected into the loaded device using a 1mL syringe. After the perfusing time, the hydrogel microparticles were washed injecting a filtered 0.1M TRIS buffer solution (45µL at a time). Confocal images of the hydrogel microparticles inside the device were registered after the binding with the target and at every washing step (CLSM Leica SP5, Objective 10x DRY, scan speed of 400 Hz, excitation wavelength 633). The fluorescence signal was then evaluated using ImageJ software and the error was presented as standard deviation on five particles.

6.2.4 Sandwich assay on-chip

Four devices were loaded with 5 functionalized microparticles each (0.1 pmol/part anti hIgG-FC). Then, 100µL of a 1nM solution of hIgG were injected into two of the loaded device using a 1mL syringe. After the perfusing time (~ 1 min), the hydrogel microparticles were washed with 90µL of a filtered 0.1M TRIS buffer solution. Then, 100µL of a 1nM solution of antih-IgGFAB647 were injected into all the loaded devices using a 1mL syringe. After a washing step, confocal images of the hydrogel microparticles inside the device were acquired (CLSM Leica SP5, Objective 10x DRY, scan speed of 400 Hz, excitation wavelength 633, zoom 1.5). All the microfluidic devices were previously treated injecting a BSA solution (1mg/ml) and let it sit for 20 minutes. The fluorescence signal was evaluated using ImageJ software and the error was presented as standard deviation on two independent experiments. The statistical difference between the samples has been evaluated with t-student test using Graphpad Prism 8.0.

6.3 Results and discussion

6.3.1 Microfluidic chip design optimization

In order to find the optimal design for the microfluidic chip three geometries were tested. The characteristics for the final application are:

- Stable trapping of the hydrogel microparticles, avoiding backflow;
- Homogeneous distribution of the sample inside all the microparticles loaded into the chip;
- No need to use a syringe or pressure pump to load or use the device;
- High transparency to the fluorescence signal (atto647N);
- Simple design, without any need to use expansive materials and complex techniques for the production.

The first designed prototype is the simplest one (Figure 6.3). It presents one single line of pillars spaced 30 µm in order to allow the perfusion by fluids, avoiding the hydrogel microparticles passage. The trapping chamber is dimensioned to host from 10 up to 100 microparticles aligned on a single plane (depth 120 µm, width 1.2mm). This device demonstrated a very low entrapment efficiency, since the microparticles were free to move inside the chamber, changing their position during the images acquisition.

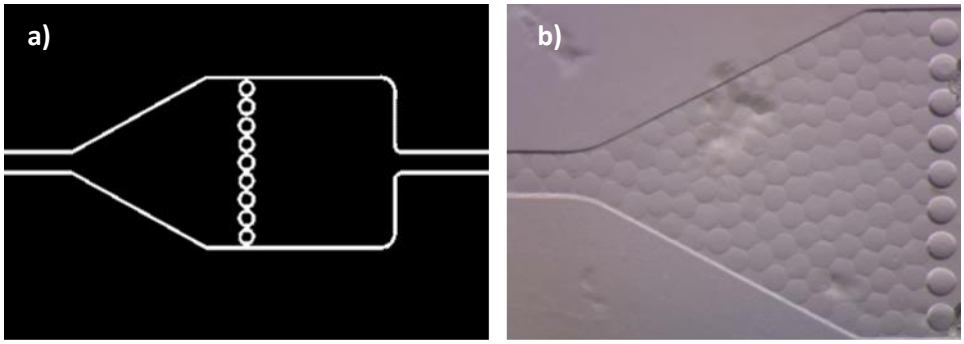

Figure 6.3: First microfluidic chip prototype: single pillars line with a 30µm spacing. a) 2D CAD of the trapping chamber. b) Optical image of trapping chamber loaded with particles.

This led to a second chip prototype in which the microparticles can be trapped individually. As shown in figure 6.4, the second prototype presents ten individual traps on three parallel lines.

Each trap measure 90µm and presents three pillars with a 30µm diagonal spacing. The trapping chamber is slightly smaller than the previous device (depth 120µm, width 1.07mm) and moreover the outlet channel (120µm) is wider than the inlet (60µm) in order to avoid particles backflow. In fact, during the device loading, the microparticles are squeezed into the inlet channel and push to the entrapment chamber. The device is designed to fill the traps line by line, starting from the inlet up to the outlet channel, hosting from one to ten particles. When microparticles flow into the microchannel, some of the particles on the streamline are guided into traps and trapped by hydrodynamic force. When a trap is occupied, the flow resistance is increased, and the other particles are forced to reach the next traps line until the trapping chamber is completely full. This device demonstrated a low entrapment efficiency since it is difficult to guide the microparticles into the middle traps line and, moreover, the microparticles tend to go out from the traps when no flux is applied to the device during the acquisition or when a change in the syringe is needed to flush a different fluid. Furthermore, the parallel lines design does not allow a homogeneous distribution of the sample into the microparticles, as the whole target molecules will distribute and consequently saturate the particles of the first lines. Thus, a third optimized prototype of the device was realized.

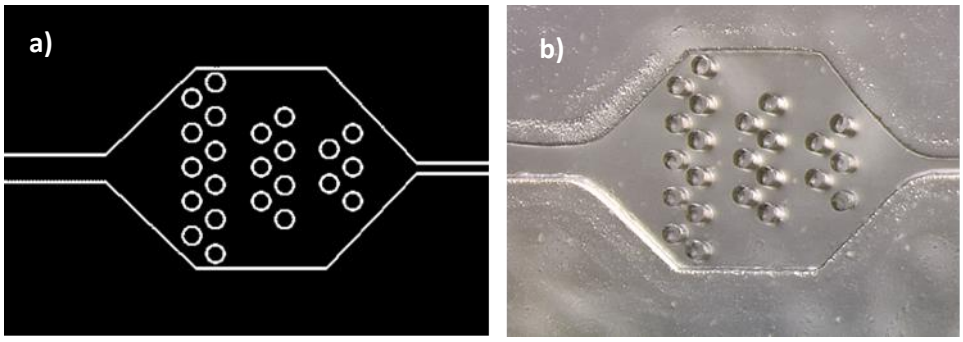

Figure 6.4: Second microfluidic chip prototype: ten individual microparticles traps on three parallel lines. Each trap is composed by three pillars and measures 90µm. a) 2D CAD of the trapping chamber. b) Optical image of the empty trapping chamber.

As shown in figure 6.5, the design provides the presence of five particles traps (each trap consisting of 3 pillars and a step) on a single line, sized to block soft particles with a diameter between 100 and 110 µm. The positioning and functioning of the step is shown in the side view of the chip in figure 6.6. It results fundamental to avoid the particles from leaking out of the traps during acquisitions. Moreover, the space between pillars is reduced to ensure a good

trapping stability even when the pressure applied by hand with the syringe is high, otherwise the soft microparticles could squeeze out of the chip during the fast injections. The trapping chamber (depth 120µm, width 1.07mm) can host from one to five particles. Furthermore, the traps are positioned on a single line to guarantee a homogeneous distribution of the target samples into all trapped hydrogel microparticles.

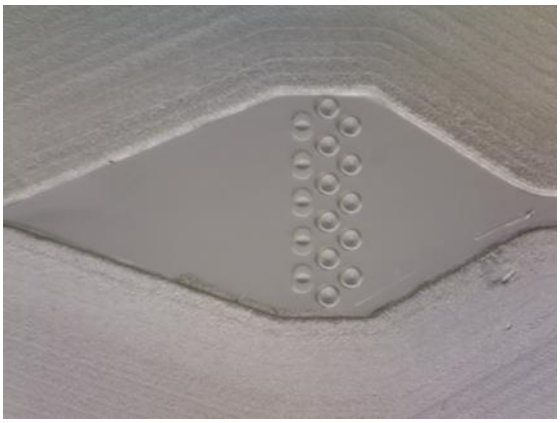

Figure 6.5: Optical image of the empty trapping chamber of the final optimized chip prototype.

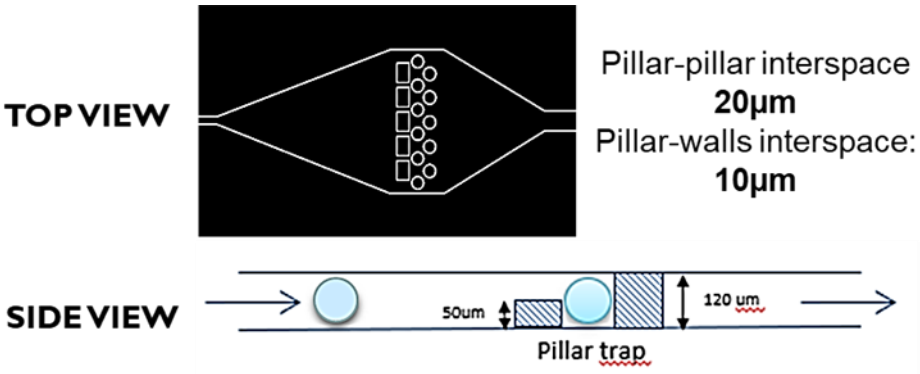

Figure 6.6: Final optimized chip prototype. Top view: 2D CAD of the trapping chamber. Each trap is designed to contain a 100-110µm particle and the 20µm space between the pillars allows fluids perfusion, avoiding the passage of particles. Side view: the arrows indicate the direction in which the device is loaded. The 50µm high steps allow the passage of the particles during the loading and prevents their spontaneous backflow during the acquisition.

6.3.2 Hydrogel microparticles trapping

As shown in figure 6.7, the optimized design of the microfluidic device allows to stably trap the desired number of hydrogel microparticles. It can be noticed how the soft microparticles are slightly deformed by the pillars and this, as well as the step, avoids the particles backflow. These images demonstrate that the design of this device for the hydrodynamic blocking of particles represents a valid alternative to the classical serpentine and wells widely used in literature to block particles and encapsulated cells[8,36,37].

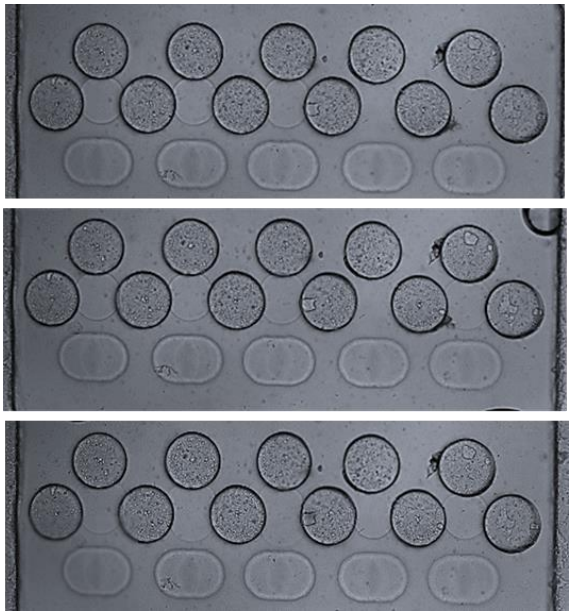

Figure 6.7: CLSM images of entrapped hydrogel microparticles inside the microfluidic device. The chip is designed to host from one up to five particles. The images show respectively three, four and five particles trapped. The particles are slightly deformed by the traps in order to ensure a stable blocking during all the immuno-assay steps.

6.3.3 Target binding and washes optimization

Preliminary tests were carried out to confirm the device ability to speed up the incubation and washing steps. In particular, the device was first loaded with 5 functionalized microparticles (0.1 pmol/part monoclonal anti human IgG FC specific) and then a sample containing a high concentration of fluorescent target (1 μm) was flushed with a syringe inside the chip. After target flushing, the fluorescence emission from the 5 microparticles was registered and measured, corresponding to point “zero” in figure 6.8. Moreover, the fluorescence signal from the channel surface was also considered for evaluating background noise. After the perfusion time of target, the hydrogel microparticles were washed with a buffer solution (45μL at a time)

for three times and the fluorescence signals were measured at each washing step. As shown by the graph in Figure 6.8, with small washing volumes, it is possible to effectively wash particles from unbound target. At each washing step, the signal intensity decreases until it reaches a plateau at an optimal washing volume, identified as 90µL, where the signals between the particles and the channel appear to be statistically different. This difference indicates the target binding which is efficiently recognized and captured by the particles in a single perfusive step Figure 6.9.

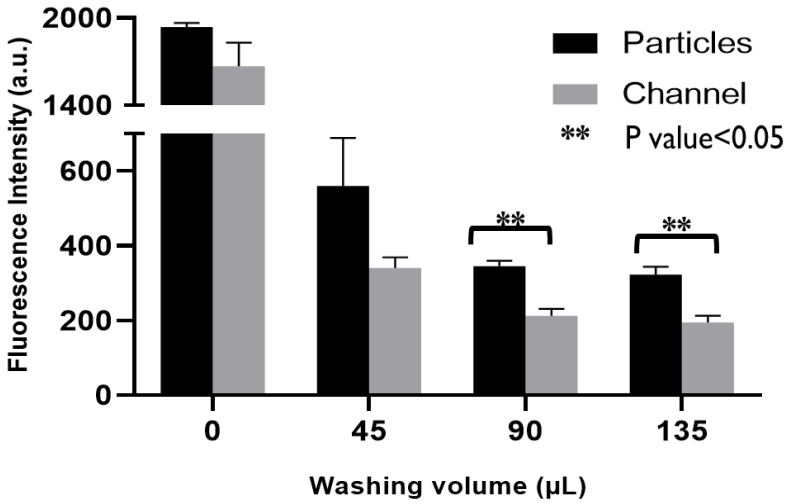

Figure 6.8: Bar-graph showing the average fluorescence intensity inside the trapped microparticles compared with that of the channel. The washing volume 0 indicates the moment in which the labelled hIgG is injected into the device.

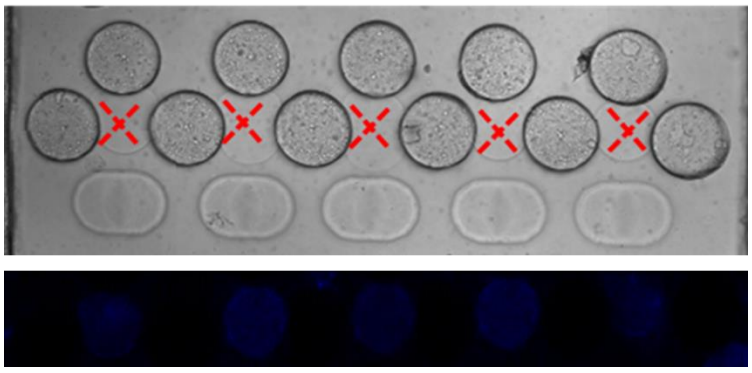

Figure 6.9: CLSM images of the fluorescent hydrogel microparticles (top: brightfield image; bottom: 647nm fluorescence signal) trapped inside the microfluidic chip. The fluorescence signal indicates the target binding, which is efficiently recognized and captured by the particles.

These data demonstrate that the chip succeeded in speed up the first step of the sandwich assay and the washing steps, as resumed in table 6.1. In fact, incubation time drastically decreases, going from 120 minutes, for the classic off-chip test, to less than one minute once the assay is performed inside the microfluidic chip. Furthermore, the washing volumes are also reduced, going from about 3.5ml to 90µL.

Table 6.1: "Incubation time" and "washing volume" comparison between on-chip and off-chip. Data are referred to the binding between the primary antibody and the fluorescent target inside the hydrogel microparticles with consequent washes. The experiments have been performed in Eppendorf (OFF-CHIP) and inside the microfluidic device (ON-CHIP).

Incubation time	
OFF-CHIP	ON-CHIP
120 min	**< 1min**
Washing volume	
OFF-CHIP	ON-CHIP
3.5 mL	**90 µL**

6.3.4 Sandwich assay on-chip: Proof-of-concept

Tests concerning the sandwich assay on chip were carried out for proof-of-concept validation. All the microfluidic devices used for the experiments were previously treated injecting a BSA solution (1mg/ml) and let it sit for 20 minutes, in order to avoid the aspecific adsorption of the antibodies onto the glass slide, which could impair the functioning of assay on-chip. The device was then loaded with 5 functionalized microparticles, then a sample containing a high concentration of target (1 nM) was flushed with a syringe inside the chip and, after one wash (90µL, 1min), 100µL of a 1nM solution of antih-IgGFAB647 were injected. After a second wash (90µL, 1min), the fluorescence emission from the 5 microparticles was registered and measured. As control, a second device was loaded with 5 functionalized microparticle and only 100µL of a 1nM solution of antih-IgGFAB647 were flushed. The results obtained from two independent experiments are shown by the bar graph in Figure 6.10. The hydrogel microparticles trapped inside the microfluidic device succeeded in detecting the target at the

selected concentration. The fluorescence intensity inside the microparticles in presence of 1nM of hIgG results to be doubled respect to the control device. This statistically significant difference indicates that the target is efficiently recognized by the secondary antibody inside the microparticles. These results demonstrate how our microfluidic device allows to perform a sandwich assay in less than 10 minutes, while the time typically needed to perform a classic sandwich ELISA (commercial kits) lies in the range between 90 minutes and 24 hours.

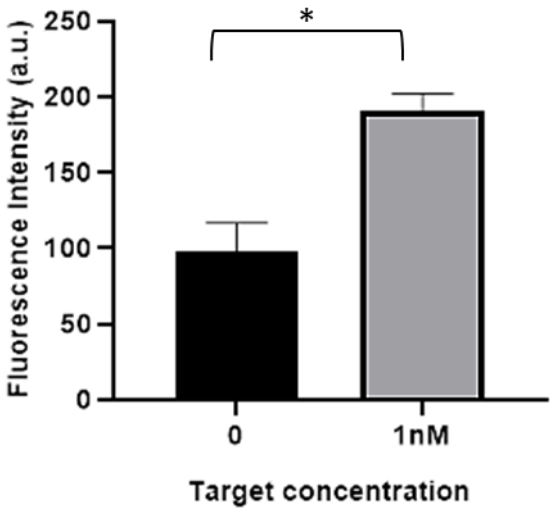

Figure 6.10: Experimental data of sandwich assay on hIgG (0 and 1nM) performed on-chip with five hydrogel microparticles (* p value < 0.05).

6.4 Conclusions

In the diagnostic field, many efforts have been made to develop sensitive, faster and cheaper platforms for immuno-assays which could replace the conventional ELISAs and suspension bead-based assays. However, it is still difficult to combine these three characteristics with the ease of use and portability needed to perform a point-of-care testing. In this work we presented a portable microfluidic device in which sensitive hydrogel microparticles for the hIgG detection are trapped. We optimized the device to achieve a stable trapping of the hydrogel microparticles and a homogeneous distribution of the sample with a simple design and no need to use pumps to perform the assay. Preliminary studies demonstrated the capability of the chip to stably block from one to five particles and to speed up the sample incubation time and the washing steps. In fact, incubation time drastically decreases, going from 120 minutes, for the classical off-chip test, to less than one minute for the assay performed inside the microfluidic chip; while the

washing volumes are also reduced, going from about 3.5ml to 90µL. In addition, the sample and all the fluids needed to perform the assay can be flushed into the chip simply by hand, with the help of a syringe. Further studies will be done to optimize the whole sandwich assay on chip. To sum up, our microfluidic device for microparticles trapping represents an easy, cheap and fast platform to perform immuno-assays. Moreover, due to the versatility of the microparticles trapped (Chapters 3-4), this system could be used for the detection of a great variety of biomolecules (antibodies, proteins, oligonucleotides…) and small molecules (pollutants, dioxin, hormones…) leading the way towards fast, sensitive and portable analytical devices.

6.5 References

1. Whitesides, G. M. The origins and the future of microfluidics. *Nature* vol. 442 368–373 (2006).
2. Janasek, D., Franzke, J. & Manz, A. Scaling and the design of miniaturized chemical-analysis systems. *Nature* vol. 442 374–380 (2006).
3. Yager, P. *et al.* Microfluidic diagnostic technologies for global public health. *Nature* vol. 442 412–418 (2006).
4. Xu, X., Sarder, P., Kotagiri, N., Achilefu, S. & Nehorai, A. Performance analysis and design of position-encoded microsphere arrays using the Ziv-Zakai bound. *IEEE Trans. Nanobioscience* **12**, 29–40 (2013).
5. Evander, M. *et al.* Noninvasive Acoustic Cell Trapping in a Microfluidic Perfusion System for Online Bioassays. *Anal. Chem.* **79**, 2984–2991 (2007).
6. Grumann, M., Geipel, A., Riegger, L., Zengerle, R. & Ducrée, J. Batch-mode mixing on centrifugal microfluidic platforms. *Lab Chip* **5**, 560–565 (2005).
7. Roos, P. & Skinner, C. D. A two bead immunoassay in a micro fluidic device using a flat laser intensity profile for illumination. *Analyst* **128**, 527–531 (2003).
8. Kim, C., Bang, J. H., Kim, Y. E., Lee, J. H. & Kang, J. Y. Stable hydrodynamic trapping of hydrogel beads for on-chip differentiation analysis of encapsulated stem cells. *Sensors Actuators, B Chem.* **166**–**167**, 859–869 (2012).
9. Dittrich, P. S. & Schwille, P. An Integrated Microfluidic System for Reaction, High-Sensitivity Detection, and Sorting of Fluorescent Cells and Particles. *Anal. Chem.* **75**, 5767–5774 (2003).
10. Kulrattanarak, T., Van Der Sman, R. G. M., Schroen, C. G. P. H. & Boom, R. M. Analysis of mixed motion in deterministic ratchets via experiment and particle

simulation. *Microfluid. Nanofluidics* **10**, 843–853 (2011).

11. Nilsson, J., Evander, M., Hammarström, B. & Laurell, T. Review of cell and particle trapping in microfluidic systems. *Anal. Chim. Acta* **649**, 141–157 (2009).

12. Tan, W. H. & Takeuchi, S. A trap-and-release integrated microfluidic system for dynamic microarray applications. *Proc. Natl. Acad. Sci. U. S. A.* **104**, 1146–1151 (2007).

13. Tan, W. H. & Takeuchi, S. Dynamic microarray system with gentle retrieval mechanism for cell-encapsulating hydrogel beads. *Lab Chip* **8**, 259–266 (2008).

14. Ohta, A. T. *et al.* Dynamic cell and microparticle control via optoelectronic tweezers. *J. Microelectromechanical Syst.* **16**, 491–499 (2007).

15. Voldman, J., Braff, R. A., Toner, M., Gray, M. L. & Schmidt, M. A. Holding forces of single-particle dielectrophoretic traps. *Biophys. J.* **80**, 531–542 (2001).

16. Mirowski, E., Moreland, J., Russek, S., Donahue, M. & Hsieh, K. Manipulation of magnetic particles by patterned arrays of magnetic spin-valve traps. *J. Magn. Magn. Mater.* **311**, 401–404 (2007).

17. Kolossa, R., Abolmaaty, A., Meyer, D. & Zhang, Z. An Inexpensive Microfluidic PDMS Chip for Visual Detection of Biofilm-forming Bacteria. *Annu. Res. Rev. Biol.* **22**, 1–13 (2018).

18. Mazutis, L. *et al.* Multi-step microfluidic droplet processing: Kinetic analysis of an in vitro translated enzyme. *Lab Chip* **9**, 2902–2908 (2009).

19. Huebner, A. *et al.* Quantitative detection of protein expression in single cells using droplet microfluidics. *Chem. Commun.* 1218–1220 (2007) doi:10.1039/b618570c.

20. Dishinger, J. F., Reid, K. R. & Kennedy, R. T. Quantitative Monitoring of Insulin Secretion from Single Islets of Langerhans in Parallel on a Microfluidic Chip. *Anal. Chem.* **81**, 3119–3127 (2009).

21. Lim, C. T., Low, H. Y., Ng, J. K. K., Liu, W. T. & Zhang, Y. Fabrication of three-dimensional hemispherical structures using photolithography. *Microfluid. Nanofluidics* **7**, 721–726 (2009).

22. Brittain, S., Paul, K., Zhao, X. M. & Whitesides, G. Soft lithography and microfabrication. *Phys. World* **11**, 31–36 (1998).

23. Heckele, M. & Schomburg, W. K. Review on micro molding of thermoplastic polymers Related content Topical Review Manufacturing microstructured tool inserts for the production of polymeric microfluidic devices A review on the importance of surface coating of micro/nano-mold in micro/nano-molding processes. *J. Micromechanics Microengineering Top. Rev.* **14**, 1 (2004).

24. Ostuni, E., Kane, R., Chen, C. S., Ingber, D. E. & Whitesides, G. M. Patterning Mammalian Cells Using Elastomeric Membranes. *Langmuir* **16**, 7811–7819 (2000).

25. Xia, Y. & Whitesides, G. M. SOFT LITHOGRAPHY. *Annu. Rev. Mater. Sci.* **28**, 153–184 (1998).

26. Groisman, A. *et al.* A microfluidic chemostat for experiments with bacterial and yeast cells. *Nat. Methods* **2**, 685–689 (2005).

27. Weibel, D. B., Diluzio, W. R. & Whitesides, G. M. Microtechnology Microfabrication meets microbiology. *Nat. Rev. | Microbiol.* **5**, (2007).

28. Eteshola, E. & Leckband, D. Development and characterization of an ELISA assay in PDMS microfluidic channels. *Sensors Actuators, B Chem.* **72**, 129–133 (2001).

29. Jeon, S., Kwon, Y. W., Park, J. Y. & Hong, S. W. Fluorescent Detection of Bovine Serum Albumin Using Surface Imprinted Films Formed on PDMS Microfluidic Channels. *J. Nanosci. Nanotechnol.* **19**, 4736–4739 (2019).

30. Tian, T. *et al.* Distance-based microfluidic quantitative detection methods for point-of-care testing. *Lab on a Chip* vol. 16 1139–1151 (2016).

31. Silverio, V. & de Freitas, S. C. Microfabrication techniques for microfluidic devices. in *Complex Fluid-Flows in Microfluidics* 25–51 (Springer International Publishing, 2017). doi:10.1007/978-3-319-59593-1_2.

32. Pandey, C. M. *et al.* Microfluidics Based Point-of-Care Diagnostics. *Biotechnol. J.* **13**, 1700047 (2018).

33. Motalebizadeh, A., Bagheri, H., Asiaei, S., Fekrat, N. & Afkhami, A. New portable smartphone-based PDMS microfluidic kit for the simultaneous colorimetric detection of arsenic and mercury. *RSC Adv.* **8**, 27091–27100 (2018).

34. Zhang, H. & Chiao, M. Anti-fouling coatings of poly(dimethylsiloxane) devices for biological and biomedical applications. *Journal of Medical and Biological Engineering* vol. 35 143–155 (2015).

35. Kim, H. T., Kim, J. K. & Jeong, O. C. Hydrophilicity of surfactant-added poly(dimethylsiloxane) and its applications. *Jpn. J. Appl. Phys.* **50**, (2011).

36. Zhao, Z., Al-Ameen, M. A., Duan, K., Ghosh, G. & Fujiou Lo, J. On-chip porous microgel generation for microfluidic enhanced VEGF detection. *Biosens. Bioelectron.* **74**, 305–312 (2015).

37. Duan, K., Ghosh, G. & Lo, J. F. Optimizing Multiplexed Detections of Diabetes Antibodies via Quantitative Microfluidic Droplet Array. *Small* **13**, 1–8 (2017).

7. Conclusions and future perspectives

Throughout this PhD thesis, we have developed, optimized and tested a hydrogel microparticles platform for biomolecule detection, successfully combining material engineering and biosensing. PEG-based hydrogels resulted to be ideal materials for this purpose due to their chemical flexibility, anti-fouling properties, optical transparency and high hydrophilicity. Firstly, microfluidic droplets generation in a T-junction device has been investigated and used in order to synthesize cleavable hydrogel microparticles with fine controlled physical and chemical properties, such as size, shape and composition to perform in-gel assays. Using optimized microfluidic parameters, we successfully synthesized monodisperse PEG-based microparticles with a cleavable cross-linker (DHEBA). The DHEBA cleavage allows to simultaneously create pores and reactive groups into the hydrogel network, producing highly versatile particles with the possibility to be functionalized post-synthesis with any biomolecule. Volumetric swelling, kinetics analysis, NMR cryoporometry and aldehydes titration allowed to optimize the cleavage reaction conditions and provide important information about the relative porosity of all the hydrogel composition tested. Moreover, the equilibrium partitioning and Fluorescence Correlation Spectroscopy analysis demonstrated that the cleaved hydrogel microparticles are accessible to single antibodies and complexes, and so they are perfect candidates for biological immuno-assay applications. The cleavable microparticles were tested, performing an in-gel sandwich assay on h-IgG as proof of concept. Our detection system demonstrated a high sensitivity (LOD ~3pM), specificity and selectivity for the hIgG, even in biological fluids, such as serum and urine, where a great amount of interfering molecules is present. Since the chemical properties of the system can be easily tuned, our microparticles represent an ideal platform for the detection of a great variety of molecules. In fact, we also used our detection system as platform to develop an in-gel competitive assay on TCDD, one of the most common and dangerous dioxin-like compound. The system showed a good sensitivity (50% signal inhibition at 500pM) on extracted and purified samples, although further studies regarding the compatibility with organic solvents typically used for the extraction (DMSO and/or dioxane) are still in progress.

In addition to the creation of new materials for diagnostics, the final goal of this project is the fabrication of a microfluidic chip which could work as point-of-care testing platform for direct detection in biological fluids. In this work we successfully realized a portable microfluidic device for the hIgG detection, in which five hydrogel microparticles are trapped. Preliminary

studies demonstrated the capability of the chip to speed up sample incubation time (less than a minute) and washing steps (less than one hundred microliters). In addition, the sample and all the fluids needed to perform the assay can be introduced into the device simply by hand, avoiding the use of expansive and bulky pumps. Further studies are in progress to optimize the whole sandwich and competitive assays on chip. In light of this earliest studies, our microfluidic device could be an easy, cheap and fast platform to perform assays on a wide variety of molecules, representing a great improvement in the field of portable analytical devices.